3D Tunnel Seismic Imaging

vorgelegt von

Jannis Tzavaras

Berlin, 25.3.2010

Dissertation
zur Erlangung des Doktorgrades
am Institut für Geologische Wissenschaften,
Fachrichtung Geophysik,
der Freien Universität Berlin

Tag der mündlichen Prüfung:	25.5.2010
1. Gutachter:	Prof. Dr. Serge A. Shapiro
2. Gutachter:	Prof. Dr. Georg Kaufmann

Erklärung

Hiermit erkläre ich, daß ich die vorgelegte Dissertation selbst verfaßt und mich dabei keiner anderen als der von mir ausdrücklich bezeichneten Quellen bedient habe. Weiterhin erkläre ich hiermit, daß ich an keiner anderen Stelle ein Prüfungsverfahren beantragt bzw. die Dissertation in dieser oder anderer Form bereits anderweitig als Prüfungsarbeit verwendet oder einer anderen Fakultät als Dissertation vorgelegt habe.

Summary

The project OnSITE (On-line Seismic Imaging System for Tunnel Excavation in Hard Rock) aims at developing an integrated approach for seismic imaging around the tunnel and prediction ahead of the tunnel face during construction work. We present the results of our subproject which is concerned with the determination of the spatial locations of faults, fractures and heterogeneities by advanced seismic imaging techniques.

We have extended existing 2D imaging techniques to 3D. We have implemented 3D versions of "Kirchhoff prestack depth migration" (KPSDM), "Fresnel Volume Migration" (FVM) and "Reflection-Image-Spectroscopy" (RIS). The 3D P- and S-velocity models required for the calculation of the Green's functions have been generated by using the 2D first-break tomography velocity models and rotating them around the tunnel axis. The 3D images were obtained by stacking the migrated data taking into account either the true phase or the absolute value.

The application of the mentioned imaging techniques to data from the Gotthard Base Tunnel (Piora adit) show significant improvements compared to standard (KPSDM) processing. The 3D RIS approach suppresses scattering effects in the low frequency band and increases resolution in the high frequency band so that some of the geological structures are much better visible. The 3D FVM technique uses slowness and polarization based estimates of the emergence angles at the receivers and restricts the imaging to the region around the actual reflection or diffraction point. We observe less spatial ambiguity and a higher resolution of most structures.

The integration of both approaches (RIS and FVM) exploits their advantages and delivers an even more pronounced and clear image of the tunnel environment.

Zusammenfassung

Das Vorhaben OnSITE (Ein seismisches Abbildungssystem zur geologischen Vorauserkundung beim Tunnelvortrieb in Festgestein) zielt darauf ab, ein ganzheitliches Konzept zur seismischen Bildgebung um einen Tunnel und eine Prognose im Voraus der Tunnelortsbrust während der Bauarbeiten zu entwickeln. Wir präsentieren die Ergebnisse unseres Teilprojekts, das sich mit der Bestimmung der räumlichen Lage von Störzonen, Brüchen und Heterogenitäten mittels fortgeschrittener seismischer Bildgebungstechniken befaßt.

Wir haben existierende 2D Abbildungsverfahren auf 3D erweitert. 3D Versionen der "Kirchhoff Pre-Stack Tiefen-Migration" (KPSDM), "Fresnel Volumen Migration" (FVM) und "Reflexionsseismischen Spektroskopie" (RIS) wurden implementiert. Die 3D P- und S-Wellenmodelle, die zur Berechnung der Greens-Funktionen benötigt wurden, sind anhand eines um die Tunnelachse rotierten 2D Erst-Einsatz-Tomographie Geschwindigkeitsmodells erzeugt worden. Die 3D Bilder wurden über eine Stapelung der migrierten Daten unter Berücksichtigung entweder der Phase oder des Absolutbetrags erhalten.

Die Anwendung der erwähnten Abbildungsverfahren auf Daten aus dem Gotthard Basis Tunnel (Piora Sondierstollen) weisen bedeutende Verbesserungen gegenüber der Standardprozessierung auf. Die 3D RIS Methode unterdrückt Streueffekte in dem tieffrequenten Band und erhöht die Auflösung in dem hochfrequenten Band, so daß ein paar von den geologischen Strukturen besser sichtbar werden. Die 3D FVM Technik gebraucht Richtungseinschätzungen der Einfallswinkel, die aus der Slowness bzw. Polarisation abgeleitet wurden, und bildet nur die Region um den wirklichen Reflexions- bzw. Diffraktionspunkt ab. Wir beobachten eine geringere räumliche Mehrdeutigkeit und eine erhöhte Auflösung der meisten Strukturen.

Die Kombination beider Herangehensweisen (RIS und FVM) nutzt ihre Vorteile aus und liefert ein markanteres und klareres Bild der Tunnelumgebung.

Contents

Chapter 1

Introduction

The high-resolution analysis of the underground space requires the development of a specialized seismic processing, imaging and interpretation scheme. Processing and imaging of recorded data must take into account arbitrary distribution and orientation of reflectors and diffractors including fault systems and fractured zones. Faults and fractures may be filled with air, gas, fluids or different rocks or minerals. The challenge of making underground construction safer and more efficient leads to the aim of improving the localization and petrophysical characterization of faults, fractures and heterogeneities around and ahead of the tunnel face during drilling. Conventional approaches use body waves (P- and S-waves) that are reflected or backscattered at geologic heterogeneities. The spatial distribution of heterogeneities is then examined by different migration techniques. Kneib et al. (2000) developed a so-called Sonic Softground Probing (SSP) for tunnel construction in loose rock. This system employs a high-frequency acoustic vibroseis source and accelerometers on the cutting wheel and acquires the data in a measurement-while-drilling fashion, while tunneling is taking place. SSP delivers a refelection seismic image of P-wave reflectors up to 100 m ahead of the tunnel face. Otto et al. (2002) apply True Reflection Tomography (TRT) seismic imaging at the Unterwald tunnel for imaging changes in the rock mass conditions ahead of the tunnel excavation. TRT is a seismic processing technique developed to create a 3D velocity tomogram of the ground conditions ahead of the tunnel excavation.

We are evaluating different methods of 3D seismic imaging around a tunnel. Tunnel seismic measurements are characterized by strongly limited spatial coverage so that special imaging techniques have to be applied. It is desirable to restrict the migration operator to the region around the point of specular reflection to resolve the spatial ambiguity stemming from the limited aperture as well as to avoid migration artifacts.

As long as sufficient spatial coverage is given, slowness analysis of single-component data can be used to derive the direction of wave-propagation at the receiver and thus construct the reflecting surface to which imaging is to be restricted (Tillmanns and Gebrande 1999, Sun and Schuster 2003). Takahashi (1995) proposes using the polarization angle from multicomponent data to resolve the spatial ambiguity. Lüth et al. (2005) extended this strategy by applying the concept of the Fresnel volumes in homogeneous and smoothly heterogeneous velocity models as an extension of 3D Kirchhoff prestack depth migration (KPSDM). Buske et al. (2009) formulated this so-called Fresnel Volume Migration (FVM) approach for single-component seismic data based on slowness analysis and applied it to standard seismic exploration data sets. In this study we apply FVM based on 3D slowness information derived by polarization analysis on tunnel seismic data. It is shown how this procedure increases the visibility of reflectors and eliminates artifacts in the seismic images.

Another challenge in complicated environments is that it is not possible to deliver a uniquely valid seismic image. Previous studies carried out at the FU Berlin have shown that heterogeneities in the underground exist over a wide range of scale lengths so that an extension of the seismic imaging method to account for the spectral behavior of reflectivity is necessary. The image will differ significantly when focusing over different frequency bands. To address this issue we apply another imaging technique based on KPSDM, the so-called Reflection Image Spectroscopy (RIS) (Yoon 2005 and 2009), to the tunnel data sets. We processed two reflection seismic data sets recorded in different adits of the Gotthard Base Tunnel.

Chapter 2

Theory

2.1 Body waves

Waves traveling in the interior of a medium are called body waves. P-waves are also known as dilatational, longitudinal, irrotational or compressional waves. They are called P-waves due to the fact that this type is the first (primary) event on an earthquake recording. The second type of body waves, the S-wave, is also referred to as shear, transverse or rotational wave (second event observed on earthquake records). The velocities of P-waves α and S-waves β can be related to the elastic constants and the density as follows:

$$\alpha = \left(\frac{\lambda + 2\mu}{\rho}\right)^{1/2} \tag{2.1}$$

$$\beta = \left(\frac{\mu}{\rho}\right)^{1/2} \tag{2.2}$$

The quantities λ and μ are known as *Lamé's constants*. Writing γ for the ratio β/α we obtain:

$$\gamma^2 = \frac{\beta^2}{\alpha^2} = \frac{\mu}{\lambda + 2\mu} = \frac{\frac{1}{2} - \sigma}{1 - \sigma} \tag{2.3}$$

Here σ denotes the Poisson's ratio. As σ decreases from 0.5 to zero, γ increases from zero to its maximum value $1/\sqrt{2}$ hence the velocity of the S-wave ranges from zero up to 70% of the velocity of the P-wave.

For fluids, μ is zero and therefore β and γ are also zero. Thus S-waves do not propagate through fluids.

S-wave motion is usually resolved into components parallel and perpendicular to the surface of the ground, which are known, as SH and SV waves respectively.

2.2 Surface waves

When the medium does not extend to infinity in all directions, other types of waves can be generated. These waves are called surface waves because they are confined to the vicinity of one of the surfaces that bound the medium. Surface waves (called ground roll as well) are usually present on reflection records. For the most part, these are Rayleigh waves with velocities ranging from 100 to about 1000 m/s. Ground roll frequencies usually are lower than those of reflections and refractions, often with the energy concentrated below 10 Hz. Ground roll alignments are straight, just as refractions are, but they represent lower velocities. The envelope of ground roll builds up and decays very slowly and often includes many cycles. Ground roll energy generally is high enough even in the reflection band to override all but the strongest reflections. However, because of the low velocity, different geophone groups are affected at different times so that only a few groups are affected at any one time. Sometimes there is more than one ground roll wavetrain, each with different velocities. Occasionally where ground roll is exceptionally strong, in-line offsets are used so that desired reflections can be recorded before the surface waves reach the spread.

2.2.1 Rayleigh waves

Rayleigh waves also called ground roll travel along the surface of the earth and involve a combination of longitudinal and transverse motion with a definite phase relation to each other. The amplitude of this wave motion decreases exponentially with depth and depends on the wavelength of the waves. During the passage of the wave, a particle traverses an elliptical path and the major axis of the ellipse is vertical. The velocity of Rayleigh waves depends upon the elastic constants near the surface and is always less than the S-wave velocity β.

2.2.2 Love waves

A Love wave involves transverse motion parallel to the surface of the ground and sometimes it is called an SH wave. The velocity of Love waves varies between the

S-wave velocity at the surface and that in deeper layers and it exhibits dispersion. Energy sources used in seismic work do not generate Love waves to a significant degree and geophones designed to respond only to vertical motion of the surface would not detect any Love waves that might exist. Therefore they are unimportant for ordinary seismic exploration.

2.3 Slowness

The 2D slowness vector $\vec{p} = (p_x, p_z)$ is defined as follows:

$$p_x = -\frac{\sin\phi}{v} \quad p_z = -\frac{\cos\phi}{v} \tag{2.4}$$

Here v denotes the velocity at the receiver. It is easy to see that the absolute value of $\vec{p}$ is equal to the reciprocal velocity:

$$|\vec{p}| = \left(p_x^2 + p_z^2\right)^{1/2} = \frac{1}{v} \tag{2.5}$$

Figure 2.1 illustrates the angles α in the x-t diagram and ϕ in the x-z diagram.

The "apparent velocity angle" in the seismogram section is (see Figure 2.2):

$$\tan\alpha = \frac{dt}{dx} \tag{2.6}$$

Thus we can derive the relation between ϕ and α. The horizontal slowness p_x is equal to:

$$p_x = \frac{dt}{dx} \tag{2.7}$$

Therefore we have:

$$\tan\alpha = \frac{dt}{dx} = p_x = -\frac{\sin\phi}{v} \tag{2.8}$$

Finally we achieve after rearranging:

$$v\tan\alpha = -\sin\phi \tag{2.9}$$

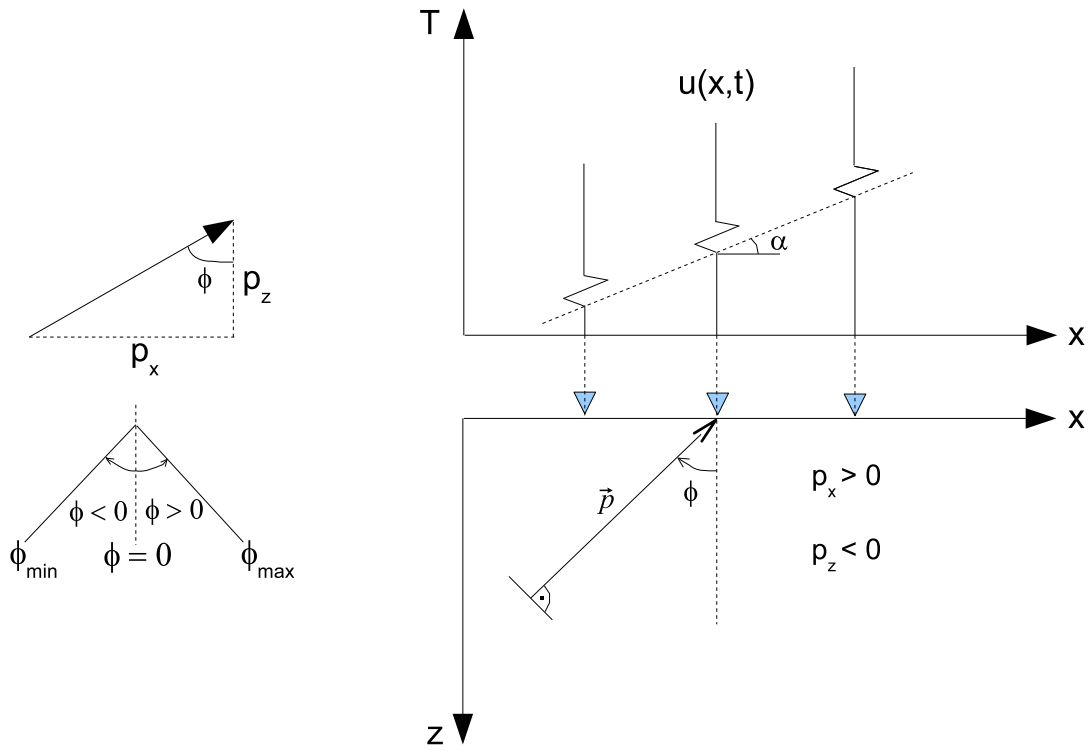

Figure 2.1: *2D slowness, definition of the angle α and ϕ.*

Figure 2.2: *"Apparent velocity angle" α.*

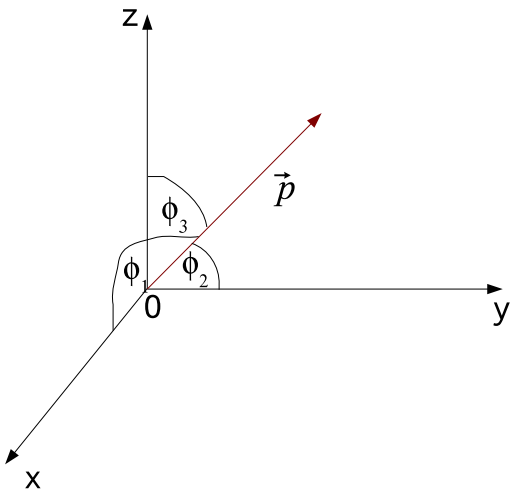

Figure 2.3: *Angles of the direction cosines.*

In the 3D case we can describe the 3D slowness vector via the direction cosines:

$$\begin{aligned} p_x &= \frac{\cos\phi_1}{v} \\ p_y &= \frac{\cos\phi_2}{v} \\ p_z &= \frac{\cos\phi_3}{v} \end{aligned} \tag{2.10}$$

Figure 2.3 shows the orientation of the angles ϕ_1, ϕ_2 and ϕ_3.

2.4 Ray Theory

In complex environments seismic signals are difficult to describe and it takes a lot of computational power to simulate realistic wave propagation. The amount of computational power is strongly reduced by approximating the propagation of body waves with ray tracing. The books of Červený (2001) and Chapman (2004) offer a complete description and derivation of ray theory. The approach is based on an asymptotic high frequency approximation to the wave equation and commonly used for several applications such as reflection seismics, refraction seismics or seismology. In this case the wavelength is small compared to the propagation distances and the spatial variations of the medium. These circumstances may require smoothing of input models but also allow us to consider the propagating wave locally as a plane wave.

There are two types of ray tracing: kinematic ray tracing and dynamic ray tracing. Here only kinematic ray tracing will be discussed since for the location method mainly the geometry and times of rays are needed. The description of the acoustic kinematic ray theory starts with the equation of motion

$$\frac{\partial v}{\partial t} = -\frac{1}{\rho}\nabla P \; + \; \frac{1}{\rho} f \tag{2.11}$$

and the relation for the time derivative of the pressure P

$$\frac{\partial P}{\partial t} = -\kappa \, \nabla \cdot \vec{v} \tag{2.12}$$

Here $\vec{v}$ denotes the velocity of the medium (particle velocity), ρ the density, κ the bulk modulus and t is the time. The symmetry of the equations above implies that velocity and pressure have similar solutions. The following ansatz is used by Chapman (2004) to solve the equation:

$$\mathbf{v}(\omega, x_R) = f(\omega) \sum_n e^{i\omega T(x_R, \ell_n)} \sum_{m=0}^{\infty} \frac{\mathbf{v}^{(m)}(x_R, \ell_n)}{(-i\omega)^m} \tag{2.13}$$

and

$$-P(\omega, x_R) = f(\omega) \sum_n e^{i\omega T(x_R, \ell_n)} \sum_{m=0}^{\infty} \frac{-P^{(m)}(x_R, \ell_n)}{(-i\omega)^m} \tag{2.14}$$

The ansatz is written in the frequency domain and $f(\omega)$ is an arbitrary spectrum depending on the source. The notation ℓ_n and the corresponding summation over n is used by Chapman (2004) to indicate that more than one path from a source point to the point x_R may exist. T indicates the travel-time function, and $^{(m)}$ denotes the index, whereas $(...)^m$ refers to the power of m. In homogeneous media acoustic and elastic waves propagate approximately without dispersion with a frequency-independent velocity and satisfy Snell's law at interfaces. In inhomogeneous media similar behavior can be observed as long as the wavelength is small compared to the spatial variation. Thus Chapman (2004) writes his ansatz as a series in amplitude coefficients $\mathbf{v}^{(m)}$ and $P^{(m)}$.

Substituting equations (2.13) and (2.14) into equation (2.11) without the body force term yields:

$$
\begin{aligned}
&f(\omega)\sum_n i\omega\cdot e^{i\omega T(x_R,\ell_n)}\sum_{m=0}^{\infty}\frac{\mathbf{v}^{(m)}(x_R,\ell_n)}{(-i\omega)^m} = \\
&-\frac{1}{\rho}\cdot\left(f(\omega)\sum_n i\omega\cdot e^{i\omega T(x_R,\ell_n)}\cdot\nabla T(x_R,\ell_n)\sum_{m=0}^{\infty}\frac{-P^{(m)}(x_R,\ell_n)}{(-i\omega)^m}\right) \\
&-\frac{1}{\rho}\cdot\left(f(\omega)\sum_n e^{i\omega T(x_R,\ell_n)}\sum_{m=0}^{\infty}\frac{-\nabla P^{(m)}(x_R,\ell_n)}{(-i\omega)^m}\right)
\end{aligned}
\tag{2.15}
$$

and into equation (2.12):

$$
\begin{aligned}
&f(\omega)\sum_n i\omega\cdot e^{i\omega T(x_R,\ell_n)}\sum_{m=0}^{\infty}\frac{-P^{(m)}(x_R,\ell_n)}{(-i\omega)^m} = \\
&-\kappa\cdot\left(f(\omega)\sum_n i\omega\cdot e^{i\omega T(x_R,\ell_n)}\cdot\nabla T(x_R,\ell_n)\sum_{m=0}^{\infty}\frac{\mathbf{v}^{(m)}(x_R,\ell_n)}{(-i\omega)^m}\right) \\
&-\kappa\cdot\left(f(\omega)\sum_n e^{i\omega T(x_R,\ell_n)}\sum_{m=0}^{\infty}\frac{-\nabla\mathbf{v}^{(m)}(x_R,\ell_n)}{(-i\omega)^m}\right)
\end{aligned}
\tag{2.16}
$$

Omitting the argument (x_R,ℓ_n) and defining boundary conditions, $v^{(-1)}=0$ and $P^{(-1)}=0$, equations (2.15) and (2.16) can be written as

$$
\rho\sum_{m=0}^{\infty}\frac{\mathbf{v}^{(m)}}{(-i\omega)^m} = -\nabla T\sum_{m=0}^{\infty}\frac{-P^{(m)}}{(-i\omega)^m}+\sum_{m=0}^{\infty}\frac{-\nabla P^{(m-1)}}{(-i\omega)^m} \tag{2.17}
$$

$$
\sum_{m=0}^{\infty}\frac{P^{(m)}}{(-i\omega)^m} = \kappa\cdot\left(\nabla T\sum_{m=0}^{\infty}\frac{\mathbf{v}^{(m)}}{(-i\omega)^m}-\sum_{m=0}^{\infty}\frac{\nabla\mathbf{v}^{(m-1)}}{(-i\omega)^m}\right) \tag{2.18}
$$

The coefficients of each power of ω are set to zero and it follows:

$$
-\nabla P^{(m-1)} = \rho\mathbf{v}^{(m)}-\mathbf{p}P^{(m)} \tag{2.19}
$$

$$
\kappa\nabla\cdot\mathbf{v}^{(m-1)} = \kappa\mathbf{p}\cdot\mathbf{v}^{(m)}-P^{(m)} \tag{2.20}
$$

for $m\geq 0$, with the slowness vector

$$
\mathbf{p} = \nabla T \tag{2.21}
$$

Multiplying equation (2.19) by $\mathbf{p}$ and rearranging equation (2.20) yields:

$$-\mathbf{p}\cdot\nabla P^{(m-1)} = \rho\,\mathbf{p}\cdot\mathbf{v}^{(m)} - \mathbf{p}^2 P^{(m)} \tag{2.22}$$

$$\mathbf{p}\cdot\mathbf{v}^{(m)} = \frac{1}{\kappa}P^{(m)} + \nabla\cdot\mathbf{v}^{(m-1)} \tag{2.23}$$

By substituting equation (2.23) in (2.22) and rearranging once again we obtain:

$$-\mathbf{p}\cdot\nabla P^{(m-1)} = \rho\left(\frac{1}{\kappa}P^{(m)} + \nabla\cdot\mathbf{v}^{(m-1)}\right) - \mathbf{p}^2 P^{(m)} \tag{2.24}$$

$$(\kappa\mathbf{p}^2 - \rho)P^{(m)} = \kappa\,\left(\rho\,\nabla\cdot\mathbf{v}^{(m-1)} + \mathbf{p}\cdot\nabla P^{(m-1)}\right) \tag{2.25}$$

For $m = 0$ and applying again the boundary conditions ($\mathbf{v}^{(-1)} = 0$ and $P^{(-1)} = 0$) this equation reduces to:

$$\left(\frac{\kappa}{\rho}\mathbf{p}^2 - 1\right)P^{(0)} = (\alpha^2\mathbf{p}^2 - 1)P^{(0)} = 0 \tag{2.26}$$

with $\alpha = \sqrt{\frac{\kappa}{\rho}}$

The series of amplitude coefficients in the ansatz (2.14) can always be defined in a way that $m = 0$ holds the first non-zero term and thus the coefficient $P^{(0)}$ can be assumed to be non-zero. Therefore it is possible to rewrite equation (2.26):

$$(\nabla T)^2 = \frac{1}{\alpha^2} \tag{2.27}$$

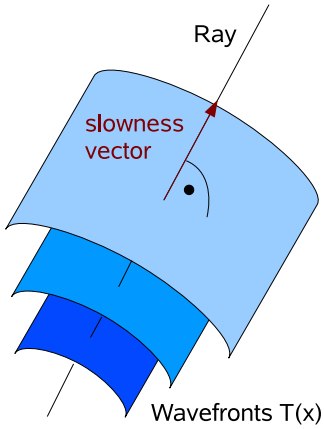

Figure 2.4: *The ray path must be in the direction of the slowness vector and perpendicular to the wavefronts.*

The equation (2.27) is also known as the eikonal equation. The surfaces where the travel-time function is $T(x) = t$ are wavefronts. The slowness vector is orthogonal to the wavefronts (see Figure 2.4). The ray is defined as the trajectory orthogonal to the wavefronts which can be parameterized in arc length s. Assuming s increases with increasing T the eikonal equation becomes:

$$\frac{dT}{ds} = \frac{1}{\alpha} \tag{2.28}$$

Thus the ray path dx/dT must be parallel to the slowness vector and from equation (2.28) it follows considering that $|dx| = ds$

$$\frac{dx}{dT} = \alpha^2 \mathbf{p} \tag{2.29}$$

Using equation (2.28) and (2.21) the change of the slowness vector is

$$\frac{d\mathbf{p}}{dT} = -\frac{\nabla\alpha}{\alpha} \tag{2.30}$$

Equation (2.29) and (2.30) represent the kinematic ray equations. Since the location method (ray tracer) applied in this work will use initial conditions for the position x_0 and the direction p_0 the ray path can be obtained solving these differential equations. A widely used method to numerically integrate ordinary differential equations is the fourth-order-Runge-Kutta (RK4) method (Press et al. 1992). This technique evaluates the derivatives once at the beginning of the interval (initial point) k_1, twice at midpoints k_2 and k_3, and once at the end of the interval k_4.

$$\begin{aligned}
k_1 &= \Delta t f(x_n, y_n) \\
k_2 &= \Delta t f(x_n + \frac{1}{2}\Delta t, y_n + \frac{1}{2}k_1) \\
k_3 &= \Delta t f(x_n + \frac{1}{2}\Delta t, y_n + \frac{1}{2}k_2) \\
k_4 &= \Delta t f(x_n + \Delta t, y_n + k_3)
\end{aligned} \tag{2.31}$$

The new value $y_{(n+1)}$ is calculated as a weighted average of these estimated increments:

$$y_{(n+1)} = y_n + \frac{1}{6}k_1 + \frac{2}{6}k_2 + \frac{2}{6}k_3 + \frac{1}{6}k_4 + 0(\Delta t^5) \tag{2.32}$$

This method is reasonably simple and robust and provides a stable and accurate numerical solution of differential equations as long as the propagation increment - here a ray

tracing time step Δt - is sufficiently small compared to the variations in the integration interval. The RK4 method has an error that is proportional to Δt^5 for an integration step, while the total accumulated error is proportional to Δt^4.

Therefore the time step for the ray propagation needs to be chosen carefully. On the other hand, the use of small propagation time steps increases the number of time steps necessary to trace a ray for a fixed length, which has the consequence of an unreasonable long computation time. Press et al. (1992) proposes the use of adaptive step size control to achieve some predetermined accuracy in the solution with minimum computational effort. In this work the number of rays as well as the considered length of rays was reasonable small and the adaptive step size was not needed in the ray tracing method.

2.5 Variable velocity and ray path direction

Changes in the direction of rays at interfaces are determined by Snell's law:

$$\frac{\sin\theta_1}{\alpha_1} = \frac{\sin\delta_1}{\beta_1} = \frac{\sin\theta_2}{\alpha_2} = \frac{\sin\delta_2}{\beta_2} = p \tag{2.33}$$

where p is the component of the slowness of each ray in Figure 2.5 parallel to the interface. A_0 denotes the incident wave, A_1 and A_2 is the reflected and refracted P-wave while B_1 and B_2 indicates the reflected and refracted S-wave respectively.

For planar parallel layering, the angle of emergence from a layer equals the angle of entry into the next layer and the ray path parameter $p = (\sin i)/v = (\sin i_0)/v_0 = \Delta t/\Delta x$ specifies ray direction, that is, p is constant along any ray and is fixed by the direction in which the ray left the source. Note that $1/v$ is the slowness and p is the component of slowness parallel to the interface, hence the component of slowness parallel to the interface is constant for each ray.

At times, the assumption is made that the velocity varies in a systematic continuous manner and therefore can be represented by a velocity function. The actual velocity usually varies extremely rapidly over short intervals; however, if we integrate these changes over distances of a wavelength, we obtain a function that is generally smooth except for discontinuities at marked lithological changes. If the velocity discontinuities are small, we are often able to represent the velocity distribution with sufficient accuracy

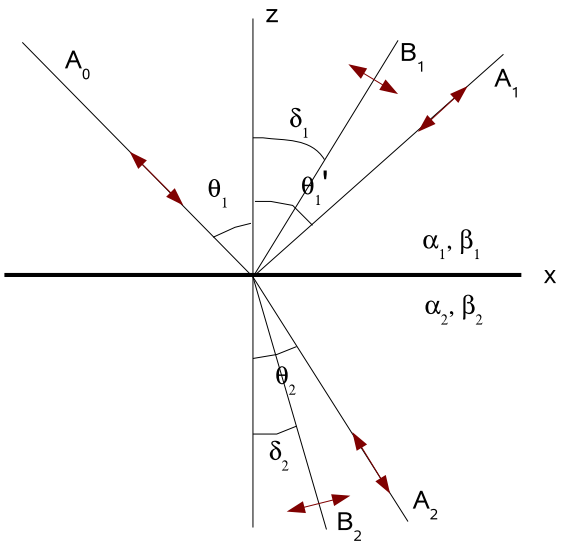

Figure 2.5: *Generation of waves at a solid-solid interface by an incident P-wave.*

by a smooth velocity function. The path of a wave traveling in such a medium is then determined by two integral equations.

To derive the equations, we assume that the medium is divided into a large number of thin beds in each of which the velocity is constant; on letting the number of beds go to infinity, the thickness of each bed becomes infinitesimal and the velocity distribution becomes a continuous function of depth. As illustrated in Figure 2.6 we have for the n^{th} bed:

$$\begin{aligned} \frac{\sin i_n}{v_n} &= \frac{\sin i_0}{v_0} = p \\ v_n &= v_n(z) \\ \Delta x_n &= \Delta z_n \tan i_n \\ \Delta t_n &= \frac{\Delta z_n}{v_n \cos i_n} \end{aligned} \tag{2.34}$$

As n goes to infinity we obtain:

$$\begin{aligned} &\frac{\sin i}{v} = \frac{\sin i_0}{v_0} = p, \quad v = v(z), \quad \frac{dx}{dz} = \tan i \\ &\frac{dt}{dz} = \frac{1}{v \cos i}, \quad x = \int_0^z \tan i \, dz, \quad t = \int_0^z \frac{dz}{v \cos i} \end{aligned} \tag{2.35}$$

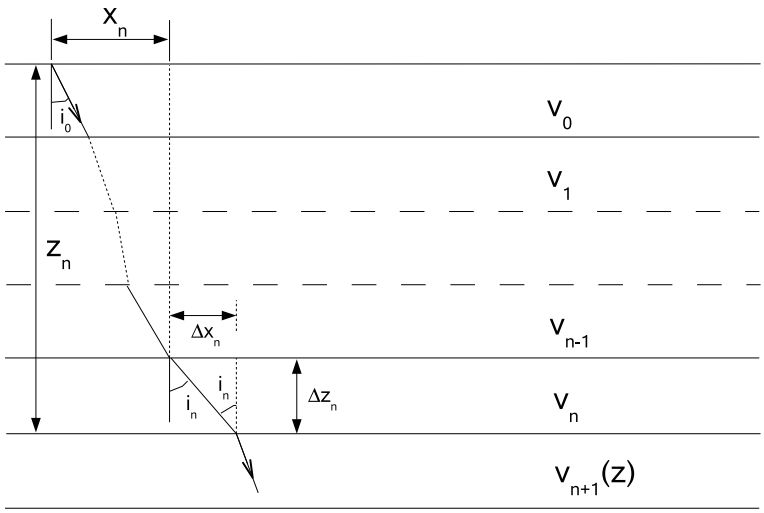

Figure 2.6: *Ray path in a medium where velocity varies with depth.*

hence,

$$x = \int_0^z \frac{pv\, dz}{[1-(pv)^2]^{1/2}} \tag{2.36}$$

$$t = \int_0^z \frac{dz}{v[1-(pv)^2]^{1/2}} \tag{2.37}$$

Because v is a function of z, equations (2.36) and (2.37) yield two integral equations relating x and t to the depth z. These equations can be solved by numerical methods when we have a table of values of v at various depth.

2.6 Attenuation, Absorption and Noise

The amplitude of events on a seismic record depends on a multitude of factors (see Figure 2.7). Some of these factors (for example recording, processing) are within our control. The effects of others can be estimated and then compensated for. Still other factors affect data with about the same traveltimes in about the same way and thus do not introduce significant trace-to-trace differences, the main factor on which interpretational decisions are based.

Divergence is usually the major factor causing time-dependent amplitude changes. The energy spreads out so that the wave decreases in strength but the total energy in the

wavefield does not change. If the medium were homogeneous, the amplitude weakening would be inversely proportional to distance, or vt; however, because velocity generally increases with depth, ray path curvature makes the wave spread out more and thus makes the decrease in amplitude larger. Newman (1973) showed that, for parallel layering, the amplitude decrease depends approximately on $1/v_{rms}^2 t$, and Hardage (1985) showed that this factor is appropriate for observed data. This phenomenon was compensated by applying an AGC (Automatic Gain Control) on all the data sets we examined.

Absorption causes wave energy to disappear by converting it to heat. However, like dispersion, most of the factors affecting the amplitude of waves as they travel through the earth redistribute the wave energy rather than cause it to disappear. Sometimes compensation for these various factors is approximated by multiplying by an empirical exponential factor.

In general, seismic amplitude decreases exponentially with time. Higher frequencies are attenuated more than lower frequencies so that the spectrum of a seismic wavelet changes with time. Spencer (1985) concludes that attenuation measurements are not promising as a diagnostic of lithology because of the intrinsic scatter produced by peg-leg multiple interference. Peg-leg multiples also called short-path multiples are successive reflections from the top and base of thin reflectors on their way to or from the principal reflecting interface with which they are associated. They delay part of the energy and therefore lengthen the wavelet.

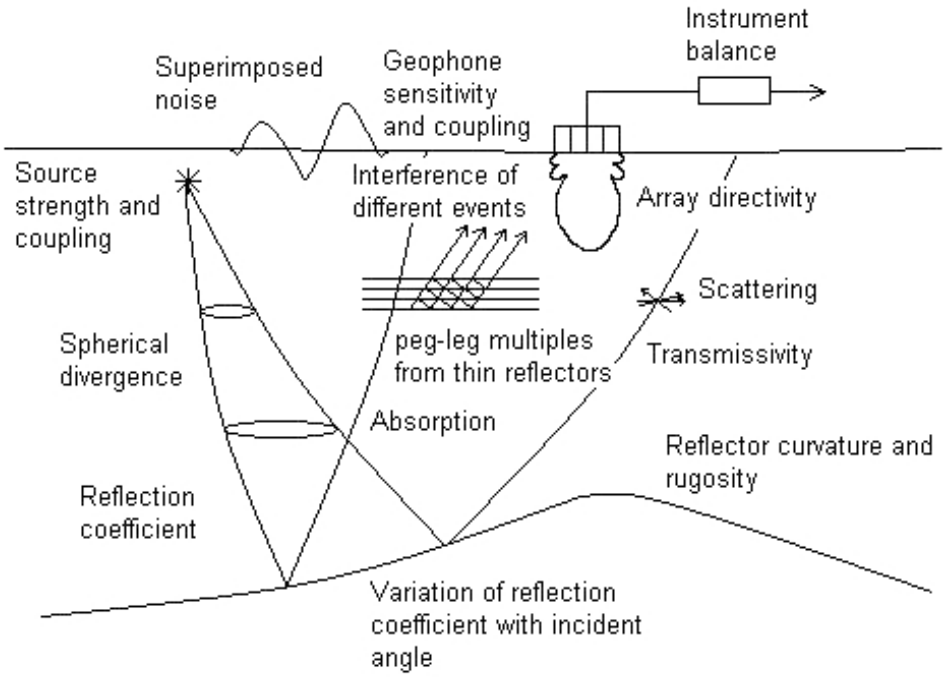

Figure 2.7: *Factors influencing amplitude. Modified after Sheriff and Geldart (1995).*

The basic mechanisms by which elastic-wave energy is transformed into heat are not clearly understood. Toksoz and Johnston (1981) summarized the state of our knowledge about attenuation and absorption. Various absorption mechanisms have been proposed (White 1965, 1966) but none appears adequate. Internal friction in the form of sliding friction (or sticking and sliding) and viscous losses in the interstitial fluids are probably the most important mechanisms, the latter being more important in high-permeability rocks. Other effects, probably of minor significance in general, are the loss when part of the heat generated during the compressive part of the wave is conducted away, piezoelectric and thermoelectric effects, and the energy used to create new surfaces which is only important near the source. Many of the postulated mechanisms predict that, in solids, Q should depend upon frequency; however, Q appears to be independent of frequency. In liquids, Q is inversely proportional to frequency. The loss mechanism in rocks must be regarded as an unsolved problem (Aki and Richards 1980).

Often no distinction is made between "attenuation" and "absorption". Because of difficulties in measuring absorption and also because the quantity of interest is usually the net decrease in wave amplitude, measurements are often made of total attenuation

without regard to its cause and the results used to determine a value of the absorption coefficient η in equation (2.38):

$$A = A_0 e^{-\eta x} \tag{2.38}$$

Here A and A_0 are values of the amplitude of a plane wavefront at two points a distance x apart. Although this may be a useful method of treating attenuation, it has no proper mathematical basis because the attenuation due to partitioning, peg-leg multiples, etc. is not a continuous function of distance, as required by equation (2.38).

In field measurements of absorption, the effects of partitioning and other significant factors must be allowed for to obtain meaningful absorption values. Difficulties in achieving this have resulted in wide divergence in absorption measurements.

Experimental evidence suggests that the absorption coefficient η is approximately proportional to frequency, that is $\eta\lambda$ is roughly constant for a particular rock. Such an increase of absorption with frequency provides one mechanism for the observed loss of high frequencies and the change of waveshape with distance. Peg-leg multiples and possibly other phenomena also produce waveshape changes. In interbedded sections, the loss in amplitude because of peg-leg multiple effects appears to be comparable to that due to absorption.

The term signal will be used in the following to denote any event on the seismic record from which we wish to obtain information. Everything else is noise, including coherent events that interfere with the observation and measurement of signals. The signal-to-noise ratio, abbreviated S/N, is the ratio of the signal in a specified portion of the record to the total noise in the same portion. Poor records result whenever the signal-to-noise ratio is small. When S/N is less than unity, the record quality is usually marginal and deteriorates rapidly as the ratio decreases further.

Seismic noise may be either coherent or incoherent. Coherent noise can be followed across at least a few traces; incoherent noise is dissimilar on all traces, and we cannot predict what a trace will be like from a knowledge of nearby traces. The difference between coherent and incoherent noise is often a matter of scale and if we had geophones more closely spaced incoherent noise would be seen as coherent. Nevertheless, incoherent noise is defined with respect to the records being used without regard for what closer spacing might reveal.

Incoherent noise is often referred to as random noise, which implies not only nonpredictability but also certain statistical properties; more often than not the noise is not

truly random. Spatial randomness and time randomness may be independent; the usual seismic trace tends to be random in time because we do not know when a reflection will occur on the basis of what the trace has shown previously, with the exception of multiples. Coherent noise is sometimes subdivided into energy that travels essentially horizontally, and energy that reaches the spread more or less vertically. It is also important to distinguish between repeatable noise and non repeatable noise; in other words, whether the same noise is observed at the same time on the same trace when the source is repeated. The three properties - coherence, travel direction and repeatability - form the basis of most methods of improving record quality.

Coherent noise includes surface waves, multiples and so on. Incoherent noise, which is spatially random and also repeatable, is due to scattering from near-surface irregularities such as boulders and small-scale faulting; such noise sources are so small and so near the spread that the outputs of two geophones will only be the same when the geophones are placed almost side by side. Nonrepeatable noise may be due to stones ejected by a shot and falling back to the earth, a person walking near a geophone etc..

In order to avoid noise frequency filtering as done by the method of Reflection-Image-Spectroscopy described in the following and Fresnel Volume Migration, which actually picks the relevant events by tracing them, can be essential.

2.7 Migration

The process of moving data elements from the time domain to subsurface locations is called migration. It is called imaging as well because its objective is to produce a clear image of the subsurface.

Migration implies that the seismic data being migrated are either primary reflections or diffractions. Migration of other types of events as if they were reflections or diffractions smears them out and creates noise.

Migration to the correct location requires knowledge of the velocity distribution but, in structurally complex areas where migration is most required, velocity information tends to have large uncertainty. However, migration is fairly tolerant of errors in vertical variations in velocity so that migration with the wrong velocity usually helps to clarify structure even though events are not located correctly. Changes in velocity in the horizontal direction produce distortions unless they are allowed for correctly. Migration

that attempts to allow for horizontal velocity changes is called depth migration. If common shot gathers are first migrated and afterwards stacked, we are talking about "prestack migration", on the contrary to the migration of already stacked sections as for example the common midpoint section which is called "poststack migration".

2.7.1 Kirchhoff Migration

The solution of the Kirchhoff integral of the wave equation is the basis of Kirchhoff Migration and shell be derived in the following chapter (after Müller 1989).

Generalized 2D Kirchhoff formula

Starting from the scalar 2D wave equation for homogeneous media:

$$\triangle U = \frac{\partial^2 U}{\partial x^2} + \frac{\partial^2 U}{\partial z^2} = \frac{1}{v^2}\frac{\partial^2 U}{\partial t^2} \tag{2.39}$$

with the Laplace-Operator: $\triangle = \frac{\partial^2}{\partial x^2} + \frac{\partial^2}{\partial z^2}$

The wave-field-quantity $U = U(x, z, t)$ is a function of position (x,z) and time t. The Fourier transform $\overline{U}$ of the wave field U in aspect to the time t is:

$$\overline{U}(x, z, \omega) = \int_{-\infty}^{\infty} U(x, z, t) e^{-i\omega t} dt \tag{2.40}$$

The velocity v of the medium shall be constant. With the relations

$$\frac{\partial^2 U}{\partial x^2} \xrightarrow{FT} \frac{\partial^2 \overline{U}}{\partial x^2} \tag{2.41}$$

$$\frac{\partial^2 U}{\partial z^2} \xrightarrow{FT} \frac{\partial^2 \overline{U}}{\partial z^2} \tag{2.42}$$

$$\frac{\partial^2 U}{\partial t^2} \xrightarrow{FT} (i\omega)(i\omega)\overline{U} = -\omega^2 \overline{U} \tag{2.43}$$

we obtain from the wave equation (2.39) the Helmholtz equation:

$$\frac{\partial^2 \overline{U}}{\partial x^2} + \frac{\partial^2 \overline{U}}{\partial z^2} = -\frac{\omega^2}{v^2}\overline{U} = -k^2 \overline{U} \tag{2.44}$$

with $\frac{\omega}{v} \equiv k =$ wavenumber

$$\triangle \overline{U} + k^2 \overline{U} = 0 \tag{2.45}$$

We are searching for a solution $\overline{U}$ of the Helmholz-equation (2.45). The solution of the wave equation U is obtained by applying the inverse Fourier transformation to $\overline{U}$. We restrict our interest in the x-z-plane on a region of the area F, which is confined by the borderline S (see Figure 2.8).

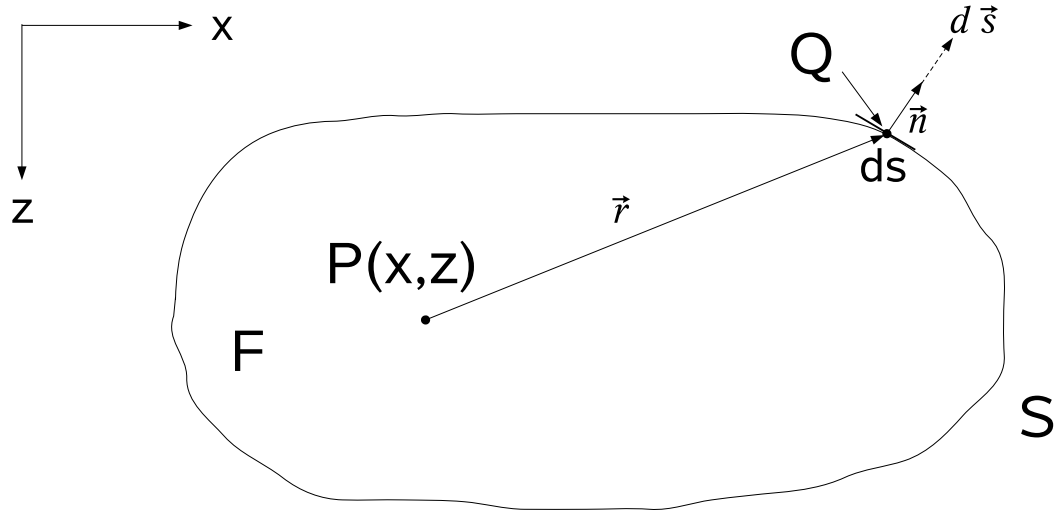

Figure 2.8: *Geometry; P point in area F, Q integrational point on the borderline S*

In this region the Green's Theorem in two dimensions is valid:

$$\int_F [A\Delta B - B\Delta A] dF = \int_S (A\nabla B - B\nabla A) d\vec{s} \tag{2.46}$$

Here A and B are two arbitrary, two times continuously differentiable functions. The vector $d\vec{s}$ is perpendicular to the boundary element of the length ds and has the same orientation as the outer normal $\vec{n}$ of S: $d\vec{s} = |d\vec{s}|\vec{n} = ds\ \vec{n}$

A shall be a solution of the Helmholtz-equation and indeed the demanded solution $\overline{U}$:

$$A \equiv \overline{U} \tag{2.47}$$

B shall be a solution of the Helmholtz-equation too and indeed a known simple solution, that we will denote in the following with G (Green's function):

$$B \equiv G \tag{2.48}$$

Which function is chosen in particular for G is depending on the problem. The most used form is the Hankel-function of the second form of the order 0. Its asymptotic form ($kr \gg 1$)

$$H_0^{(2)}(kr) \approx \sqrt{\frac{2}{\pi kr}} e^{-i\left(kr-\frac{\pi}{4}\right)} \tag{2.49}$$

is describing together with the factor $e^{i\omega t}$ a from the point P(x,z) at r=0 with the velocity v expanding cylindrical wave and is suitable for the derivation of equations that describe the propagation of seismic waves.

For the migration we are only interested in the wave field "on the reflector", that means the continuation of the wave field must occur backwards in time. Therefore we choose in the following instead of the Hankel function of the second form the one of the first form: $H_0^{(1)}(kr)$. Its asymptotic form reads ($kr \gg 1$):

$$H_0^{(1)}(kr) \approx \sqrt{\frac{2}{\pi kr}} e^{i\left(kr-\frac{\pi}{4}\right)} \tag{2.50}$$

It describes in combination with the factor $e^{i\omega t}$ a contracting cylindrical wave, which arrives with the velocity v in the point P(x,z) at r=0.

The Green's Sentence assumes, that A and B (in this case $\overline{U}$ and G) do not have a singularity in F. Because $G = H_0^{(1)}(kr)$ is however singular the area F must be reduced about a small circle around the point P(x,z) with the radius r_0. Therefore the boundary S' of the circle must be added to the boundary S which limits the area F (see Figure 2.9).

The Green's Sentence reads now:

$$\int_F [\overline{U}\Delta G - G\Delta\overline{U}]dF = \int_S [\overline{U}\nabla G - G\nabla\overline{U}]d\vec{s} + \int_{S'} [\overline{U}\nabla G - G\nabla\overline{U}]d\vec{s'} \tag{2.51}$$

Because G and $\overline{U}$ are solutions of the Helmholtz equation, for both applies:

$$\Delta\overline{U} + k^2\overline{U} = 0 \Rightarrow \Delta\overline{U} = -k^2\overline{U} \tag{2.52}$$

$$\Delta G + k^2 G = 0 \Rightarrow \Delta G = -k^2 G \tag{2.53}$$

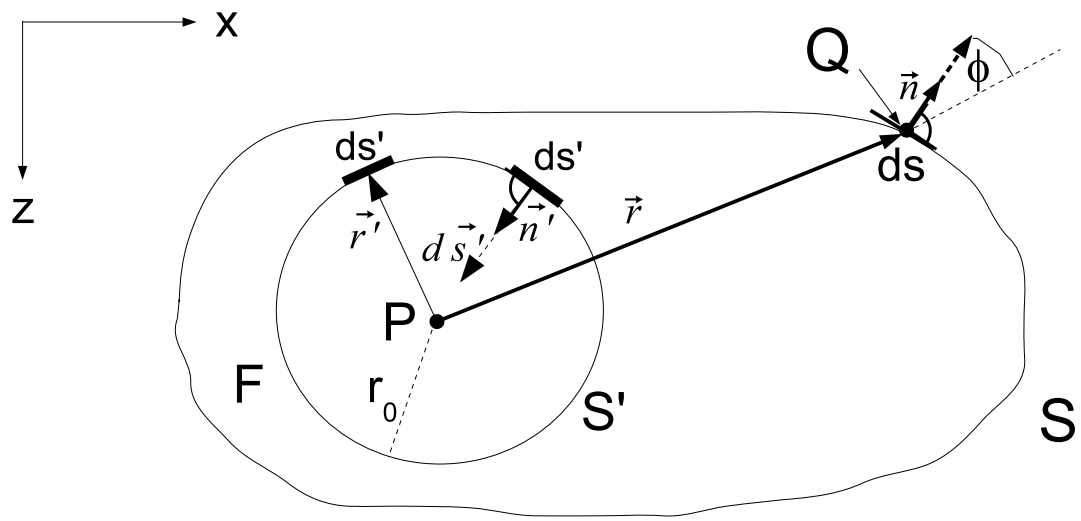

Figure 2.9: *Extended geometry*

From equation (2.51) it follows:

$$\int_F [\overline{U}(-k^2 G) - G(-k^2 \overline{U})] dF = \int_S [\overline{U} \nabla G - G \nabla \overline{U}] d\vec{s} + \int_{S'} [\overline{U} \nabla G - G \nabla \overline{U}] d\vec{s'} \quad (2.54)$$

$$0 = \int_S [\overline{U} \nabla G - G \nabla \overline{U}] d\vec{s} + \int_{S'} [\overline{U} \nabla G - G \nabla \overline{U}] d\vec{s'} \quad (2.55)$$

In the following the two integrals in (2.55) will be calculated separately.

It applies:

$$a = \int_S [\overline{U} \nabla G - G \nabla \overline{U}] d\vec{s} = \int_S [\overline{U} \nabla H_0^{(1)}(kr) - H_0^{(1)}(kr) \nabla \overline{U}] d\vec{s} \quad (2.56)$$

By multiplying the vector $d\vec{s}$ with the gradient of the Hankel function and the gradient of $\overline{U}$ on S, we obtain:

$$[\nabla ...] d\vec{s} = [\nabla ...] \vec{n} |d\vec{s}| = \frac{\partial ...}{\partial n} ds \quad (2.57)$$

$$a = \int_S \left[\overline{U} \frac{\partial}{\partial n} H_0^{(1)}(kr) - H_0^{(1)}(kr) \frac{\partial}{\partial n} \overline{U} \right] ds \quad (2.58)$$

For the derivative of the Hankel function in the point Q on S in the direction of the external normal $\vec{n}$ it applies:

$$\frac{\partial}{\partial n} H_0^{(1)}(kr) = -kH_1^{(1)}(kr)\cos\phi \tag{2.59}$$

thus the first integral reads:

$$a = -\int_S \left[\overline{U} k H_1^{(1)}(kr)\cos\phi + \frac{\partial \overline{U}}{\partial n} H_0^{(1)}(kr)\right] ds \tag{2.60}$$

Taking into account, that for infinitesimal r_0 the Fourier transform $\overline{U}$ and its gradient $\nabla\overline{U}$ on S' can be regarded as constant, they can be written in front of the integral. It follows:

$$b = \int_{S'} \overline{U}\nabla G d\vec{s'} - \int_{S'} G\nabla\overline{U} d\vec{s'} = \overline{U}_P \int_{S'} \nabla G d\vec{s'} - (\nabla\overline{U})_P \int_{S'} G d\vec{s'} \tag{2.61}$$

The vector $d\vec{s'}$ and the normal unity vector $\vec{n'}$ are perpendicular to the borderline S' and they are pointing towards the inner circle (see Figure 2.9):

$$d\vec{s'} = |d\vec{s'}|\vec{n'} = ds'\vec{n'} \qquad\qquad -\vec{n'} = \frac{\vec{r'}}{|\vec{r'}|} \tag{2.62}$$

The gradient of G points to S' in the direction of $\vec{r'}$, therefore it applies:

$$\nabla G = \frac{dG}{dr}\frac{\vec{r'}}{|\vec{r'}|} = -\frac{dG}{dr}\vec{n'} \tag{2.63}$$

Thus we have:

$$b = \overline{U}_P \int_{S'} \frac{dG}{dr}(-\vec{n'})\cdot\vec{n'} ds' - (\nabla\overline{U})_P \int_{S'} G d\vec{s'} \tag{2.64}$$

The integral over G is performed on a circle with a radius r_0 and G is cylindrically symmetric with respect to r. Thus the value of G on S' and the derivative of G with respect to r can be written in front of the integral.

$$b = \overline{U}_P \left.\frac{dG}{dr}\right|_{r=r_0} \int_{S'} ds' - (\nabla\overline{U})_P \, G|_{r=r_0} \int_{S'} d\vec{s'} \tag{2.65}$$

The integral $\int_{S'} d\vec{s'}$ vanishes, because the sum of all $d\vec{s'}$ vectors annihilates due to symmetry reasons to the zero vector. The integral over S' is nothing else than the perimeter of the circle with radius r_0. It follows:

$$b = -2\,\pi\,r_0\,\overline{U}_P\,\left.\frac{dG}{dr}\right|_{r=r_0} \tag{2.66}$$

For the derivative of the Hankel function $H_0^{(1)}(kr)$ at the point Q on S' with respect to r it applies:

$$\frac{d}{dr}H_0^{(1)}(kr) = -kH_1^{(1)}(kr) \tag{2.67}$$

Therefore following value is obtained for the second integral:

$$b = 2\,\pi\,\overline{U}_P\,k\,r_0\,H_1^{(1)}(kr_0) \tag{2.68}$$

By letting the radius of the circle r_0 tend to zero, we obtain:

$$\lim_{kr_0\to 0} k\,r_0\,H_1^{(1)}(kr_0) = -\frac{2\,i}{\pi} \tag{2.69}$$

Thus the second integral reads:

$$\lim_{r_0\to 0} b = -4\,i\,\overline{U}_P \tag{2.70}$$

All in all equation (2.55) can be written now as:

$$0 = -\int_S \left[\overline{U}\,k\,H_1^{(1)}(kr)\,\cos\phi + \frac{\partial\overline{U}}{\partial n}H_0^{(1)}(kr)\right] ds - 4\,i\,\overline{U}_P \tag{2.71}$$

respectively

$$\overline{U}_P = \frac{i}{4}\int_S \left[\overline{U}\,k\,H_1^{(1)}(kr)\,\cos\phi + \frac{\partial\overline{U}}{\partial n}H_0^{(1)}(kr)\right] ds \tag{2.72}$$

This is the Fourier transform of our requested solution U_P, the value of the wavefield at the point P. In order to perform the backtransformation in the time domain we rewrite equation (2.72) (wavenumber $k = \omega/v$):

$$\overline{U}_P = \int_S \left[[i\,\omega\,\overline{U}]\left[-\frac{1}{4v}\,H_1^{(1)}\left(\frac{r}{v}\,\omega\right)\right]\,\cos\phi + \left[\frac{\partial\overline{U}}{\partial n}\right]\left[-\frac{i}{4}\,H_0^{(1)}\left(\frac{r}{v}\,\omega\right)\right]\right] ds \tag{2.73}$$

A inverse Fourier transform with the relations

$$i\,\omega\,\overline{U} \xrightarrow{FT^{-1}} \frac{\partial U}{\partial t} \qquad \frac{\partial \overline{U}}{\partial n} \xrightarrow{FT^{-1}} \frac{\partial U}{\partial n} \tag{2.74}$$

$$-\frac{1}{4\,v}\,H_1^{(1)}\left(\frac{r}{v}\,\omega\right) \xrightarrow{FT^{-1}} \frac{-t\,H\left(-t-\frac{r}{v}\right)}{2\,\pi\,r\,\sqrt{t^2-\frac{r^2}{v^2}}} \tag{2.75}$$

$$-\frac{i}{4}\,H_0^{(1)}\left(\frac{r}{v}\,\omega\right) \xrightarrow{FT^{-1}} \frac{-H\left(-t-\frac{r}{v}\right)}{2\,\pi\,\sqrt{t^2-\frac{r^2}{v^2}}} \tag{2.76}$$

yields:

$$U_P = U(x,z,t) = \frac{1}{2\,\pi}\int_S \left[\frac{\partial U}{\partial t} * \frac{t\,H\left(-t-\frac{r}{v}\right)}{r\,\sqrt{t^2-\frac{r^2}{v^2}}}\,\cos\phi + \frac{\partial U}{\partial n} * \frac{H\left(-t-\frac{r}{v}\right)}{\sqrt{t^2-\frac{r^2}{v^2}}}\right] ds \tag{2.77}$$

Here * is the convolution and H is the step function. This formula is the solution of the wave equation in the time domain. In order to calculate the wavefield at the point P(x,z) one has to know the time derivative $\frac{\partial U}{\partial t}$ and the derivative of the outer normal $\frac{\partial U}{\partial n}$ on the borderline S. The time proceeds here backwards. The filtering with

$$\frac{t\,H\left(-t-\frac{r}{v}\right)}{r\,\sqrt{t^2-\frac{r^2}{v^2}}} \qquad \frac{H\left(-t-\frac{r}{v}\right)}{\sqrt{t^2-\frac{r^2}{v^2}}} \tag{2.78}$$

consists of a time shift of r/v that means the travel time of the wave from the integrational point Q to the Point P and additionally of a low pass filtering because the operators are no delta functions.

3D Kirchhoff formula

In the 3D case the Kirchhoff formula corresponding to (2.77) reads:

$$U_P = \frac{1}{4\,\pi}\int_{S'} \left[\frac{\partial U}{\partial t} * \frac{\delta\left(t-\frac{r}{v}\right)}{r\,v}\,\cos\phi + \frac{\partial U}{\partial n} * \frac{\delta\left(t-\frac{r}{v}\right)}{r} + U * \frac{\delta\left(t-\frac{r}{v}\right)}{r^2}\,\cos\phi\right] ds' \tag{2.79}$$

Here S' denotes a surface, on which the marginals of $\frac{\partial U}{\partial t}$, $\frac{\partial U}{\partial n}$ and U are given. The filtering of these marginals is a pure retardation.

In the special case of a half space, that means that S' denotes the x-y plane combined with a hemisphere with infinite radius, the 3D Kirchhoff formula is:

$$U_P = \frac{1}{2\,\pi} \int_{-\infty}^{+\infty} \int_{-\infty}^{+\infty} \left[\frac{\partial U}{\partial t} * \frac{\delta\left(t - \frac{r}{v}\right)}{r\,v} + U * \frac{\delta\left(t - \frac{r}{v}\right)}{r^2} \right] \cos\phi \, dxdy \tag{2.80}$$

For the migration we want to know the wave field in the depth before reaching the surface at z=0. This means a continuation of the wave field in the past. The Kirchhoff formula for the past is given by:

$$U_P = \frac{1}{2\,\pi} \int_{-\infty}^{+\infty} \int_{-\infty}^{+\infty} \left[-\frac{\partial U}{\partial t} * \frac{\delta\left(t + \frac{r}{v}\right)}{r\,v} + U * \frac{\delta\left(t + \frac{r}{v}\right)}{r^2} \right] \cos\phi \, dxdy \tag{2.81}$$

By neglecting the $\frac{1}{r^2}$ term and using $\cos\phi = \frac{z}{r}$ we obtain:

$$U_P \approx \frac{1}{2\,\pi} \int_{-\infty}^{+\infty} \int_{-\infty}^{+\infty} -\frac{\partial U}{\partial t} * \frac{\delta\left(t + \frac{r}{v}\right)}{r^2\,v}\, z \, dxdy \tag{2.82}$$

Calculating the convolution

$$\frac{\partial U}{\partial t} * \delta\left(t + \frac{r}{v}\right) = \int_{-\infty}^{+\infty} \frac{\partial U(t')}{\partial t'} \delta\left(t + \frac{r}{v} - t'\right) dt' = \frac{\partial U\left(t + \frac{r}{v}\right)}{\partial t} \tag{2.83}$$

yields:

$$U_P = U(x, y, z, t) \approx \int_{-\infty}^{+\infty} \int_{-\infty}^{+\infty} \frac{\partial U\left(x', y', 0, t + \frac{r}{v}\right)}{\partial t} \left(-\frac{z}{2\,\pi\,r^2\,v}\right) dx'dy' \tag{2.84}$$

Thus we achieve a weighting factor of the value:

$$W(x', y') = -\frac{z}{2\,\pi\,r^2\,v} \tag{2.85}$$

The formula (2.84) is used in all calculations containing Kirchhoff Prestack Depth Mirgation (KPSDM).

2.7.2 Fresnel Volume Migration

Homogeneous model

An extension of three component Kirchhoff prestack depth migration will be explained, where the migration operator is restricted to the Fresnel volume of the specular reflected

ray path (after Lüth et al. 2004). In homogeneous media, the angle between the observed and the expected polarization is used to decide whether a certain image point belongs to the Fresnel volume. In heterogeneous media, the orthogonal distance between the image point and the paraxial Fresnel-ray traced from the receiver location is used.

For scalar wavefields, a Kirchhoff migration is usually described by means of the diffraction stack integral (DSI) (see Schleicher et al. 1993):

$$V(\vec{m}) = \frac{-1}{2\pi} \int \int_A \int w(\vec{x}, \vec{m}) \dot{u}_f(\vec{x}, t_S + t_R) dx \tag{2.86}$$

The migrated image $V(\vec{m})$ at a point in the subsurface $\vec{m} = (x, y, z)$ is constructed as a weighted summation along diffraction surfaces. The diffraction traveltime $t_S + t_R = t_S(\vec{x}_S, \vec{m}) + t_R(\vec{x}_R, \vec{m})$ is the traveltime from the source and the receiver to the image point, respectively. The aperture A is the region over which the sources and receivers are distributed. This can be a line (borehole or tunnel), a surface, or a volume. To account for the most general case, we write the diffraction stack as a volume integral. The term $\dot{u}_f$ denotes the time derivative of the input wavefield which is needed in order to correctly recover the source pulse (Newman 1975). The weight function w accounts for the correct treatment of amplitudes during the backpropagation of the wavefield.

For the treatment of elastic wavefields recorded on two or three components, the wavefield must be projected onto the expected direction of polarization for any given subsurface point (Jackson et al. 1991; Takahashi 1995). The diffraction stack can then be written as:

$$V(\vec{m}) = \frac{-1}{2\pi} \int \int_A \int w \dot{\vec{u}}_f(\vec{x}, t_S + t_R) \vec{e}_r dx \tag{2.87}$$

The vectorial character of the wavefield is taken into account, whereas the property to be summed over is still a scalar. The image $V(\vec{m})$ consists of the backpropagated multicomponent wavefield projected onto the expected polarization direction $\vec{e}_r$ for the ray code under consideration. In order to restrict the image of a recorded reflection to that part of the volume which physically contributes to the signal another weight is introduced. This weight is unrelated to the true-amplitude weight w of equation (2.87) but it can be applied in addition to it.

For an arbitrary ray representing a seismic wave between two points, the volume of physical contribution can be described by the Fresnel volume of first order (Kravtsov and Orlov 1990). The Fresnel volume can be described as follows: Consider a seismic ray which travels from the source point S to the scattering point M and then to the

receiver location R. The total length of the ray is l. A point P is located in the vicinity of M and its distance from the source point S and the receiver R is s and r, respectively (see Fig. 2.10).

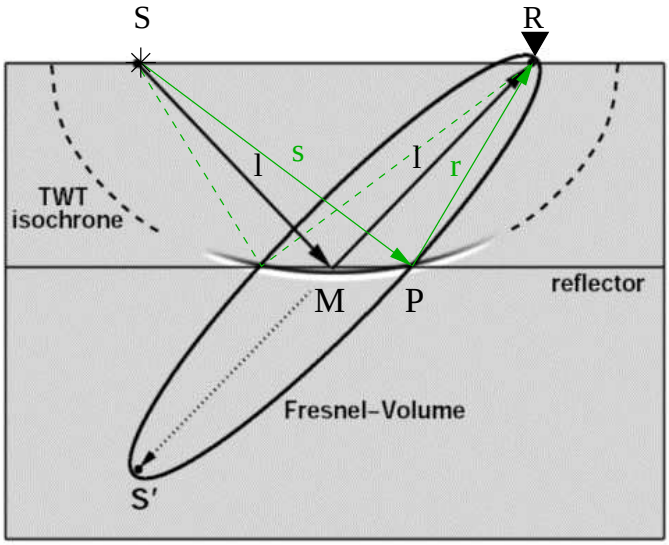

Figure 2.10: *FVM sketch showing the intersection of the Fresnel Volume and the isochrone (Buske 2009).*

Then, the Fresnel condition states that P is within the Fresnel-volume of n^{th} order if

$$|s + r - l| \leq n\frac{\lambda}{2} \tag{2.88}$$

with n=1,2,... and λ is the wavelength of a monofrequency wave. For the transient signals used in practice, one has to replace λ by a reasonable estimate of the dominant wavelength. In the case of a constant velocity medium, simple geometrical considerations are sufficient to decide which part of the isochrone belongs to the n^{th} Fresnel-volume of the ray $\overline{SMR}$. Goertz et al. (2003) derive that, if

$$cos(\gamma) \geq \frac{2r^2 + 2rs - n(r+s)\lambda + n^2\frac{\lambda^2}{4}}{2r^2 + 2rs - nr\lambda} = H_n \tag{2.89}$$

the considered point P is located within the n^{th} Fresnel-volume of $\overline{SMR}$. The angle γ describes the opening angle between $\overline{RM}$, the measured polarization on the trace at R, and $\overline{RP}$, the expected polarization for the depth point P under consideration. In order

to incorporate such a Fresnel zone criterion into the integral formulation of equation (2.87) an additional weighting factor is defined:

$$F_c = \begin{cases} 1 & : cos\gamma \geq H_1 \\ \frac{cos\gamma - H_2}{|H_1 - H_2|} & : H_1 > cos\gamma \geq H_2 \\ 0 & : cos\gamma < H_2 \end{cases} \tag{2.90}$$

where H_1 is the expression on the right hand side of equation (2.89) for n=1. The image formula for the Fresnel-volume migration then becomes:

$$V(\vec{m}) = \frac{-1}{2\pi} \int \int_A \int F_c w \dot{\vec{u}}_f(\vec{x}, t_S + t_R) \vec{e}_r dx \tag{2.91}$$

with the Fresnel criterion F_c. As the Fresnel-criterion is zero for all points which are not located within the first and second Fresnel volumes of the specular ray path, the image is thus efficiently restricted to the physically relevant part of the volume around the point of specular reflection. Compared with standard vector Kirchhoff migration the Fresnel volume migration does not require wide apertures in order to achieve a sufficient superposition of migration operators. Therefore this method is expected to be particularly useful for data with limited aperture.

Heterogeneous model

The relatively simple geometrical considerations with respect to the Fresnel volume are not valid in heterogeneous velocity fields. In such fields the rays are curved and the Fresnel volume has a more complex shape. The Fresnel volume of a ray describing a primary reflection from a defined reflector can be constructed using the traveltime fields of shotpoint S, receiver R and of the reflector (Kvasnicka and Červený 1994). In our case, the traveltime fields of shot and receiver are available, but the traveltimes from the reflector are not. Alternatively, the Fresnel volume of a known ray $\overline{SMR}$ can be constructed in paraxial approximation (Červený and Soares 1992). For that, we would not only need to know the ray path between the virtual reflection point and the receiver, which is easily constructed using the direction of wave propagation at the receiver (see Sun and Schuster 2003), but also the ray path between the shot point location and the image point, which would require relatively costly two-point ray tracing. We therefore propose to replace the Fresnel volume of the ray path $\overline{SMR}$ by the Fresnel volume of

the direct ray $\overline{S'R}$, where S' denotes the virtual mirror source as seen from R (see Fig. 2.11).

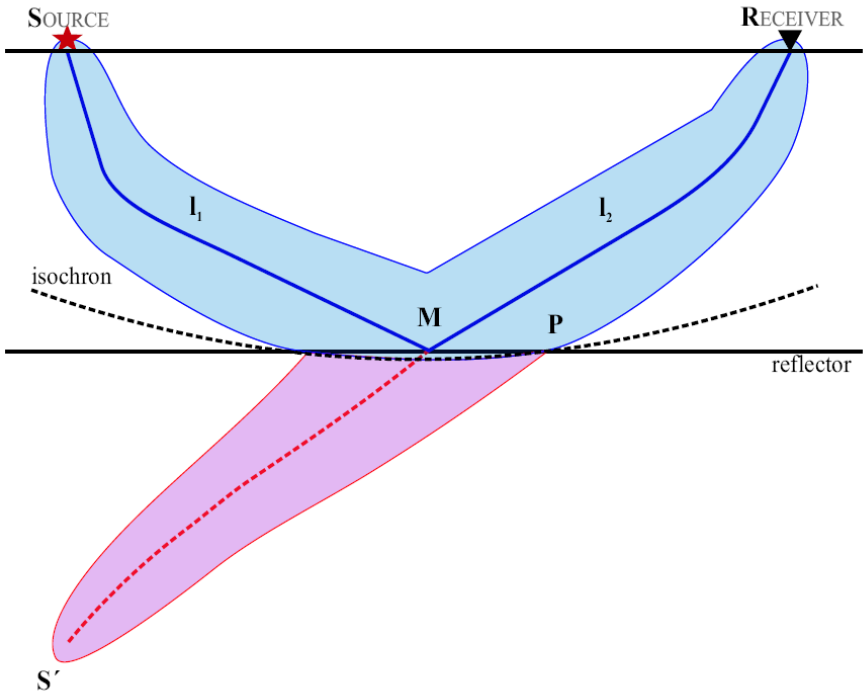

Figure 2.11: *Fresnel volume in a heterogeneous model.*

The traveltime of the ray equals the traveltime of the ray $\overline{SMR}(t = t_{SMR})$. In the vicinity of the reflection point M the Fresnel volume of the reflected ray $\overline{SMR}$ is nearly identical to the Fresnel volume of the direct ray $\overline{S'R}$. The construction of the Fresnel volume of the ray $\overline{S'R}$ follows the procedure of Fresnel volume ray tracing presented by Cerveny and Soares (1992). It is based on the paraxial ray method and merely consists of simple algebraic manipulations of the elements of the ray-propagator matrix. Consider a ray between two points (A and B) in a heterogeneous velocity field $v = v(x, y, z)$. At any point P along the ray, in paraxial approximation the Fresnel volume can be described by an ellipse with the half axes oriented along two eigenvectors of 2×2 matrices containing the minors of the propagator matrices of the ray computed at the points P and B. The half axes are given by (Červený and Soares 1992):

$$r_1(P) = \left[\frac{T}{M_1(P)}\right]^{1/2}, r_2(P) = \left[\frac{T}{M_2(P)}\right]^{1/2} \tag{2.92}$$

Here, T is the dominant period of the signal, and M_1 and M_2 are the two eigenvalues of

matrix M, which is expressed in terms of the ray propagator matrices of the considered point P and of the end point B of the ray (Červený and Soares 1992). The ray propagator matrix is a 4×4 matrix which is part of the dynamic ray tracing system (Červený 2001). The differential equation for the ray propagator Π reads:

$$\frac{d\Pi}{dt} = \begin{pmatrix} 0 & 0 & v^2 & 0 \\ 0 & 0 & 0 & v^2 \\ \frac{\partial^2 v}{\partial q_1^2} & \frac{\partial^2 v}{\partial q_1 \partial q_2} & 0 & 0 \\ \frac{\partial^2 v}{\partial q_2 \partial q_1} & \frac{\partial^2 v}{\partial q_1^2} & 0 & 0 \end{pmatrix} \Pi \tag{2.93}$$

At the starting point A of the ray, $\Pi = I$, where I is the 4×4 unity matrix. The ray centered coordinates perpendicular to the ray are q_1 and q_2. From equation (2.93) it can be observed that the second spatial derivatives of the velocity field are needed, which may cause numerical problems in practice. However, usually relatively smooth velocity models are used for prestack migration, so that we can assume that these velocity models have a locally constant velocity gradient. We therefore neglect the terms of the second derivatives for the purpose of approximating the Fresnel volume. In general, 16 different equations have to be solved for each point along the ray for the construction of the complete ray propagator matrix. In our simplified approximation, only one additional equation beside the kinematic ray tracing system must be solved:

$$\frac{d\Pi_{13}}{dt} = v^2 \tag{2.94}$$

The initial condition for Π_{13} at the first point of the ray is $\Pi = 0$. The simplified ray propagator implies that the two eigenvalues of M are identical, and the approximate Fresnel volume has a circular shape perpendicular to the ray. Its radius is:

$$r(P) \approx \sqrt{\frac{T}{\frac{1}{\Pi_{13}(P)} - \frac{1}{\Pi_{13}(P) - \Pi_{13}(B)}}}, \tag{2.95}$$

where $\Pi_{13}(B)$ and $\Pi_{13}(P)$ are the elements of the ray propagator at the end of the ray and at the considered point P on the ray, respectively.

Using the relation described above we now can apply the following procedure to implement 3C Fresnel volume migration in a heterogeneous background velocity model. Note that the procedure is described for P-waves recorded at the receiver R, and it has to be carried out within a loop over all traces and for all image points within the trace loop:

1. Compute the two-way traveltime of the image point by adding the traveltimes t_S and t_R from the source and receiver.

2. Determine the data polarization of the 3C-trace at the computed traveltime.

3. Use the data polarization as the initial condition for a ray from the receiver R to point S', where S' is defined by the point of intersection of the ray with the isochrone $t = t_S + t_R$ in the traveltime field of receiver R.

4. Construct the ray $\overline{RS'}$ and the Fresnel radii along it using equation (2.95).

5. Determine the orthogonal distance of the image point from the ray, compare it to the respective Fresnel radius and select according to the Fresnel criterion F_c (equation (2.90)).

6. The summation is carried out according to equation (2.91).

2.7.3 Reflection-Image-Spectroscopy

This approach was invented to extract structural details from seismic reflection images of strongly heterogeneous media. It accounts for the frequency dependence of scattering. The redistribution of seismic energy into reflected (backscattered) and transmitted (forward scattered) waves is referred to as scattering. The scattered energy and the wave field fluctuations vary in dependence on the magnitude of the velocity fluctuation as well as on the ratio between the wavelength and the spatial size of the heterogeneities. Thus seismic images will significantly differ when migration is performed over different frequency ranges. Strong scattering in a certain frequency band of the data will lead to severe amplitude loss and phase fluctuations. The loss of coherency and reflection strength will affect the image of a deep reflector. The reflector shape will be biased or the reflector is screened at all. In another frequency band scattering might be less severe such that reflectors are imaged properly. In the broadband image the fluctuations are superposed, covering the coherent reflections. Besides the extraction of the undistorted reflectors the method is furthermore applied to gain additional information on the spatial parameters of the heterogeneities in the medium (Yoon 2005).

Mathematically the method RIS is based on a Fast Fourier Transformation (FFT) from the time to the frequency domain. In the frequency domain a trapezoidal filter is applied to the data. Then a reverse FFT is performed with the frequency filtered data. KPSDM is implemented to the data according to formula (2.84). The obtained images

are supposed to offer suppressed scattering effects in the low-frequency band, which improves the visibility, and an increased resolution in the high-frequency band.

Chapter 3

The Piora data set

3.1 Geological setting and survey layout

We have processed a reflection seismic data set acquired in the Gotthard Base Tunnel (Piora adit). The Gotthard Base Tunnel is located between the cities Lucerne and Lugano in Switzerland. It will be the largest traffic tunnel on earth with 57 km length when completed presumably in 2015. The geographical site of the measurement setup is shown in Figure 3.1 and a geological cross section is shown in Figure 3.2. The seismic survey in the Piora adit is situated above the Gotthard Base Tunnel in the Penninic Gneiss Zone near the Piora Basin.

Figure 3.3 shows the geology at the measurement site. The major geological feature of the transition between two Gneiss variations (Leventina Gneiss - Lucomagno Gneiss) slices the tunnel within the extent of the seismic line.

The geology along the tunnel wall at the measurement site is shown in Figure 3.4. The main geological features are the transition between the Leventina and the Lucomagno Gneiss at $x = 2900\,m$ as mentioned before as well as the fault gouge at $x = 3105\,m$.

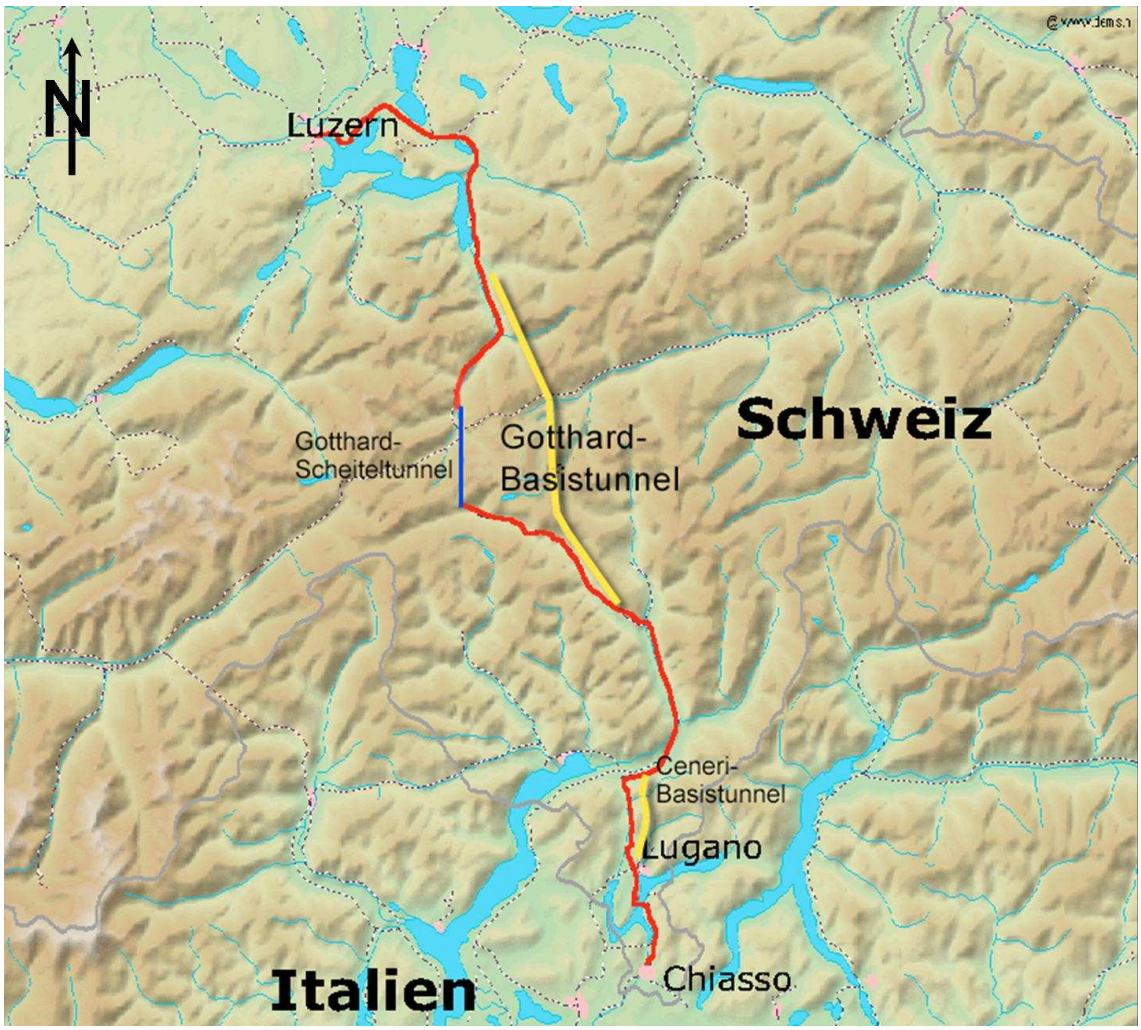

Figure 3.1: *Location of the Gotthard Base Tunnel (picture copied from http://de.wikipedia.org/wiki/Gotthard_Basistunnel)*

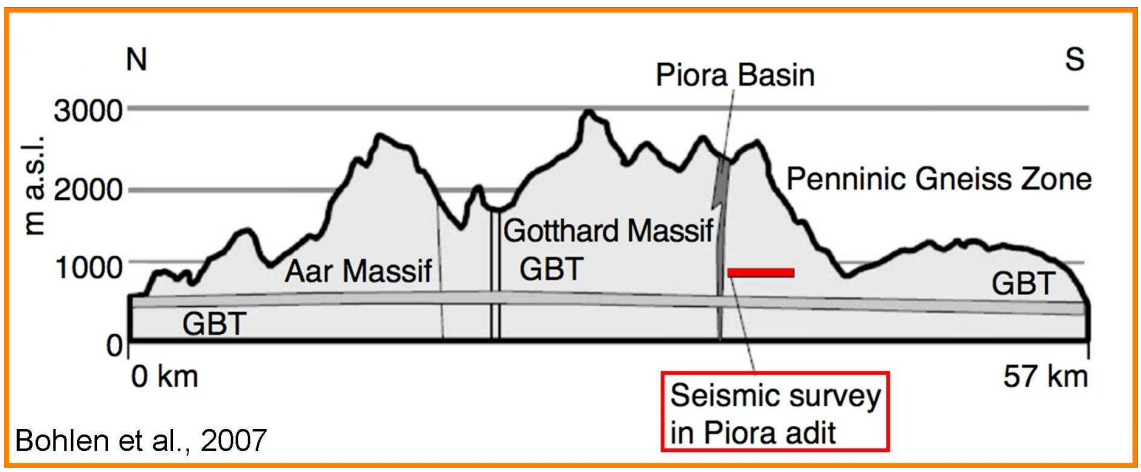

Figure 3.2: *Geological setting and location of the Piora adit (Bohlen 2007)*

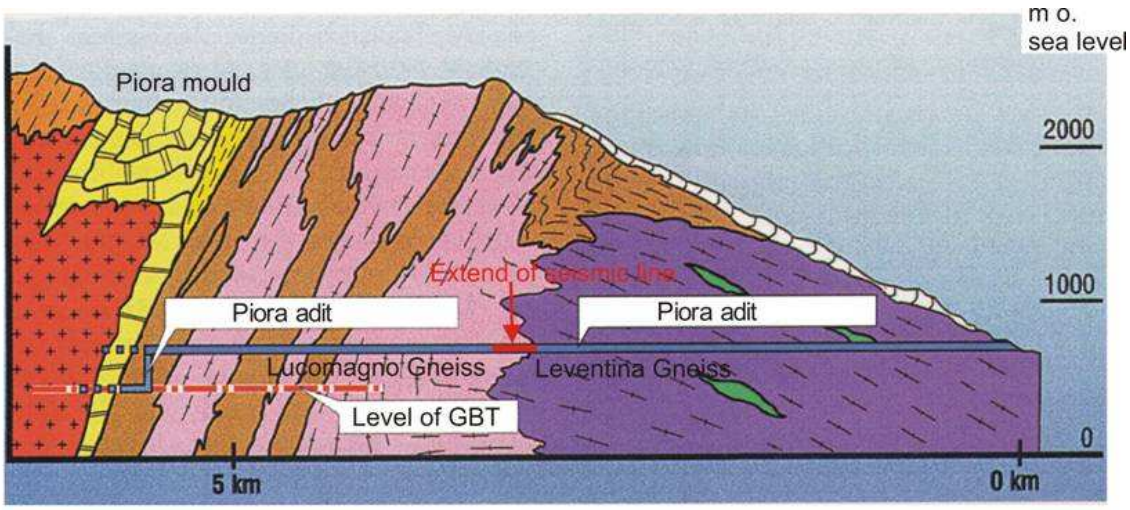

Figure 3.3: *Geological cross section showing the transition between the different Gneiss variations (Leventina Gneiss - Lucomagno Gneiss) (Schneider 1997).*

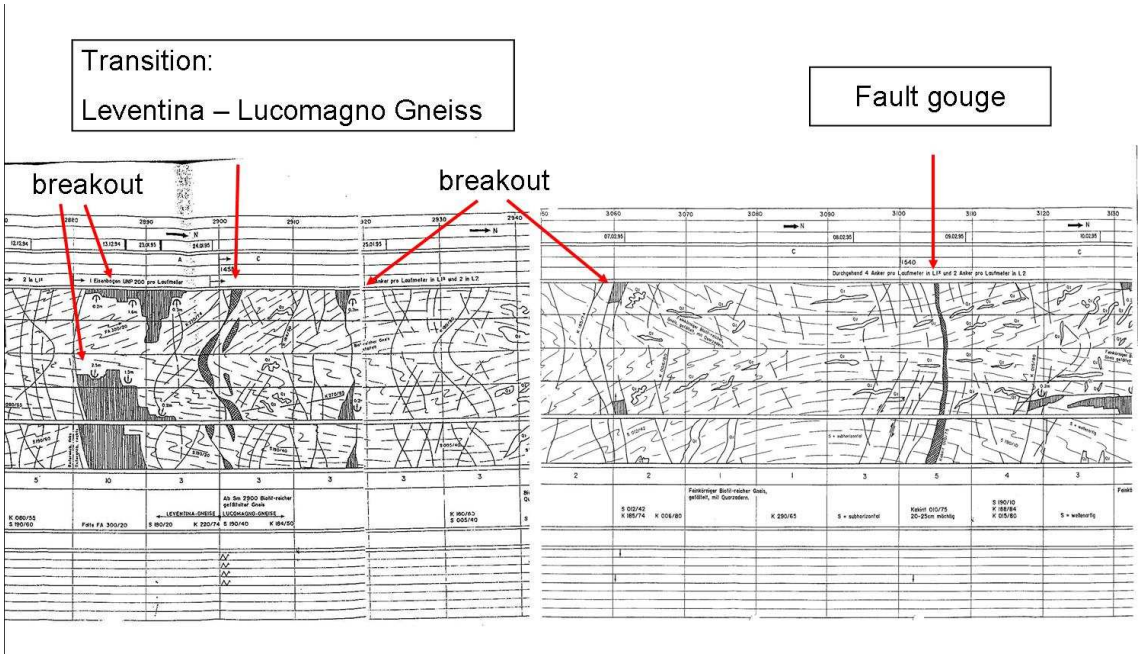

Figure 3.4: *Geological features along the tunnel wall.*

We used 147 different source points. The source was a pneumatic hammer moved along the wall with a motor vehicle. It was triggered every 1 m advancing towards the tunnel face starting at $x = 2882,5\,m$ and ending at $x = 3028,5\,m$. 15 three-component receivers are located at two meters depth in the tunnel wall (see Figure 3.5). Every shot

was recorded at each receiver. The total amount of 147 shots recorded at one receiver is called a common receiver gather. The sampling interval was $dt = 31\,\mu s$ and the total number of time samples per trace was $nt = 5120$.

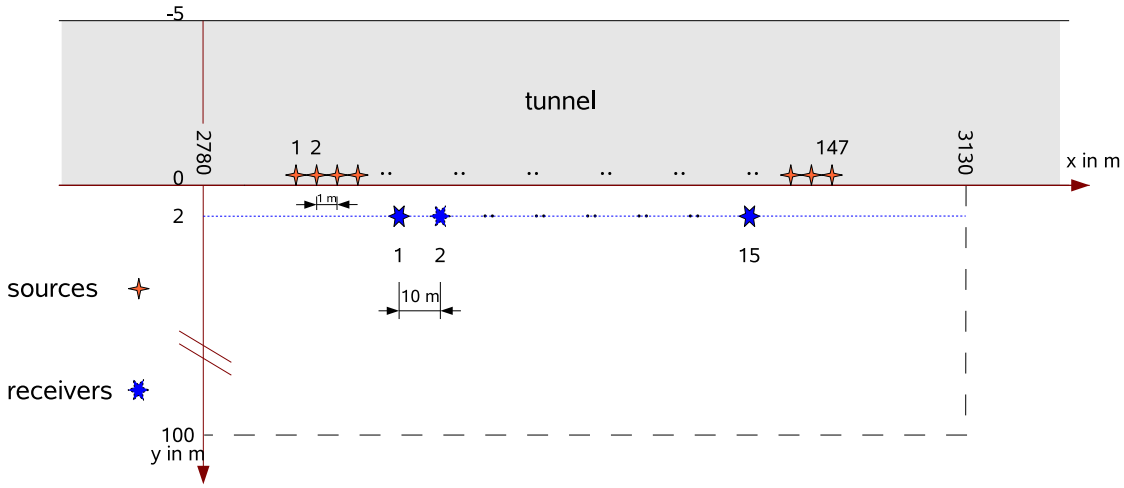

Figure 3.5: *Acquisition geometry in the Piora adit.*

3.2 Velocity model

A 3D Kirchhoff prestack depth migration was applied to the data. In order to do this a 2D first-break tomography P- and S-velocity model (Giese et al. 2005) was used and extrapolated to a grid containing 701×201 grid points (see Figure 3.6). Slow velocities are indicated in black and blue while high velocities are designated in red. We observe a slow velocity zone in close vicinity to the tunnel due to the excavation damage zone. Changes of the velocity occur at the major geological features as the gneiss transition and the cataclastic zone (see Figure 3.7). We implemented a 3D P- and S-velocity model by rotating the extrapolated 2D first-break tomography models for the Piora adit around the tunnel axis (see Figure 3.8 and 3.9). The 3D model contains $351 \times 206 \times 206$ grid points. The grid increment is $1\,m$. The velocity in the tunnel was assumed to be constant at $v = 330\,m/s$ (propagation velocity of sound in air). In the P-velocity model the velocities range from $3000\,m/s$ up to about $6000\,m/s$, and for the S-velocity model the velocities vary between $1500\,m/s$ and $3900\,m/s$.

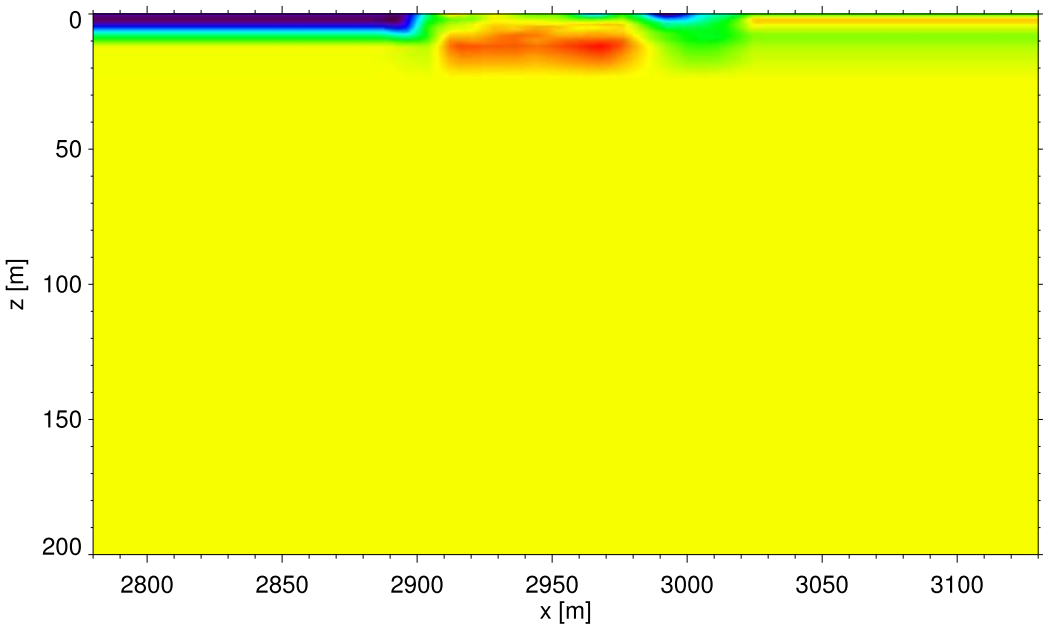

Figure 3.6: *Extrapolated 2D P-velocity model.*

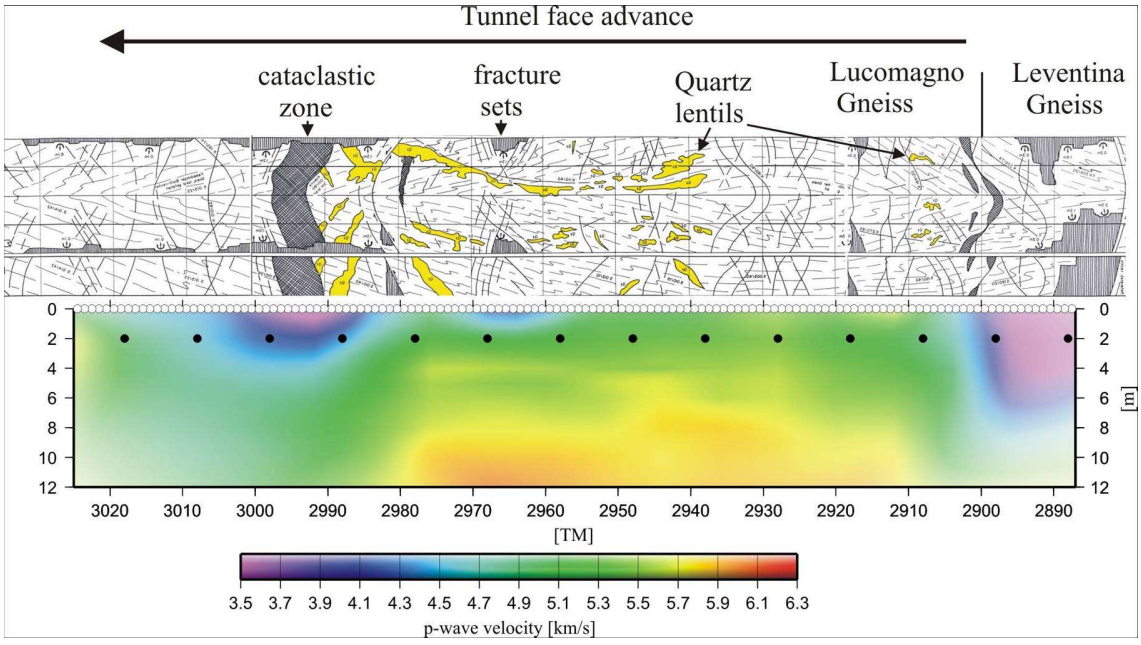

Figure 3.7: *Comparison of the velocity model to the geology. The white dots are the 147 shotpoints and the black dots correspond to the 15 receivers.*

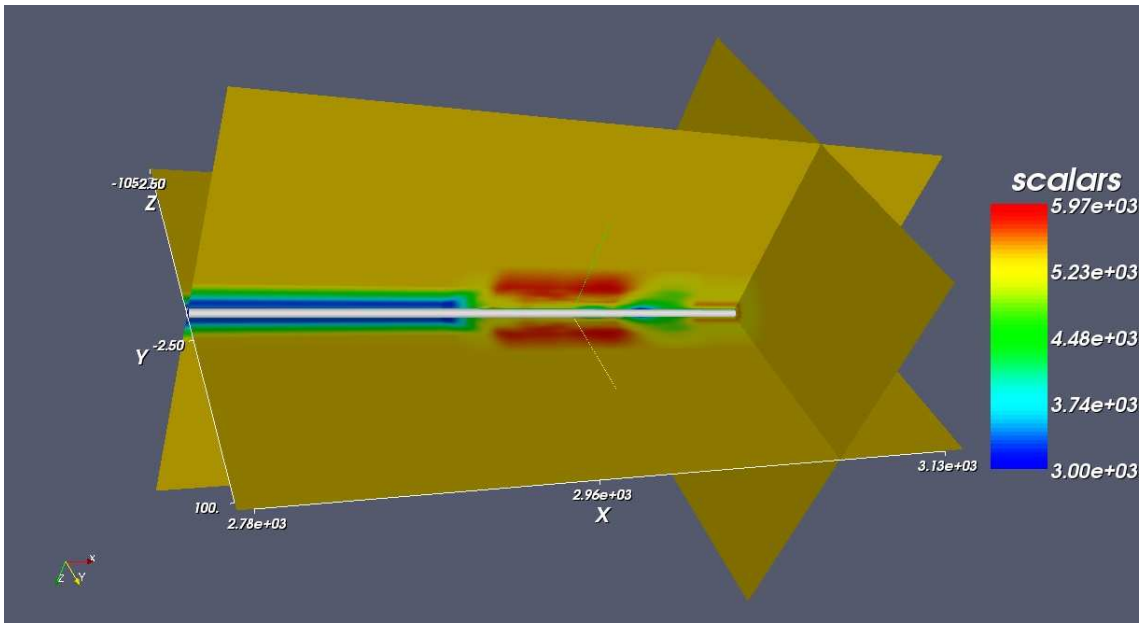

Figure 3.8: *3D first-break tomography P-velocity model for the Piora adit. Scalars denote the P-velocities in m/s.*

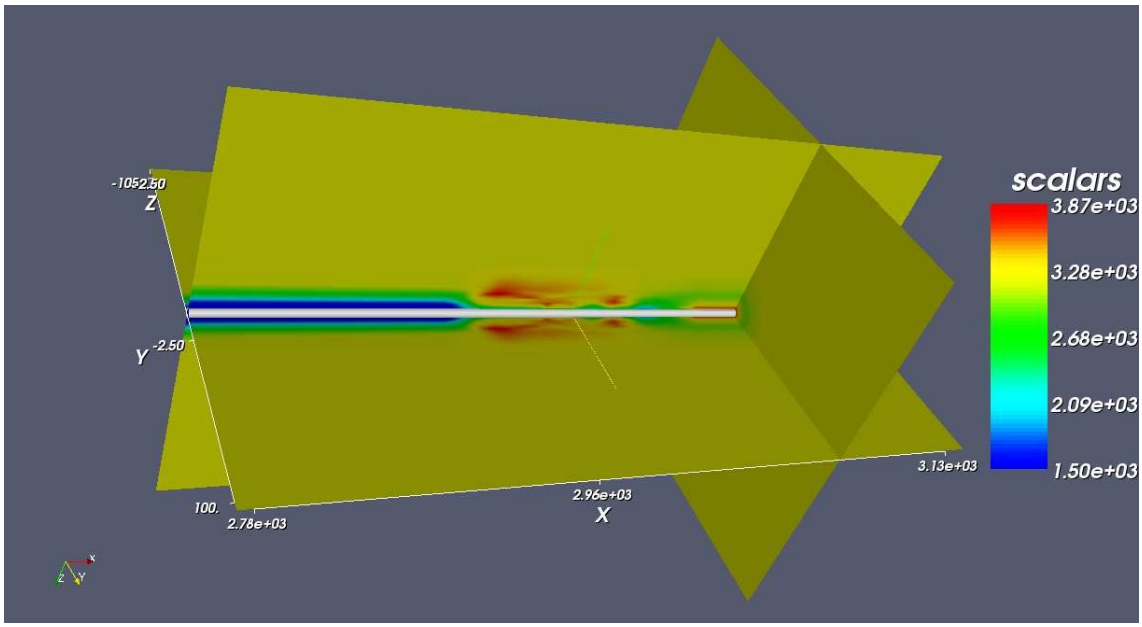

Figure 3.9: *3D first-break tomography S-velocity model for the Piora adit. Scalars denote the S-velocities in m/s.*

3.3 Kirchhoff prestack depth migration

The data set was preprocessed by muting the first arrivals, then applying an AGC to the data and afterwards normalizing each trace to its maximum. In Figures 3.10 and 3.11 the receiver gather before and after applying the preprocessing steps is shown. In the raw data in figure 3.10 we can notice the first break of the P- (red arrow) and S-wave (green arrow) and a dominant reflection indicated by two black arrows. This reflection has its minimum travel time at trace #20 at (source position $x = 2901,5\,m$) and therefore it can be related to the transition between the two gneiss variations. We observe that spherical divergence is compensated and that surface waves are suppressed in the preprocessed data as well.

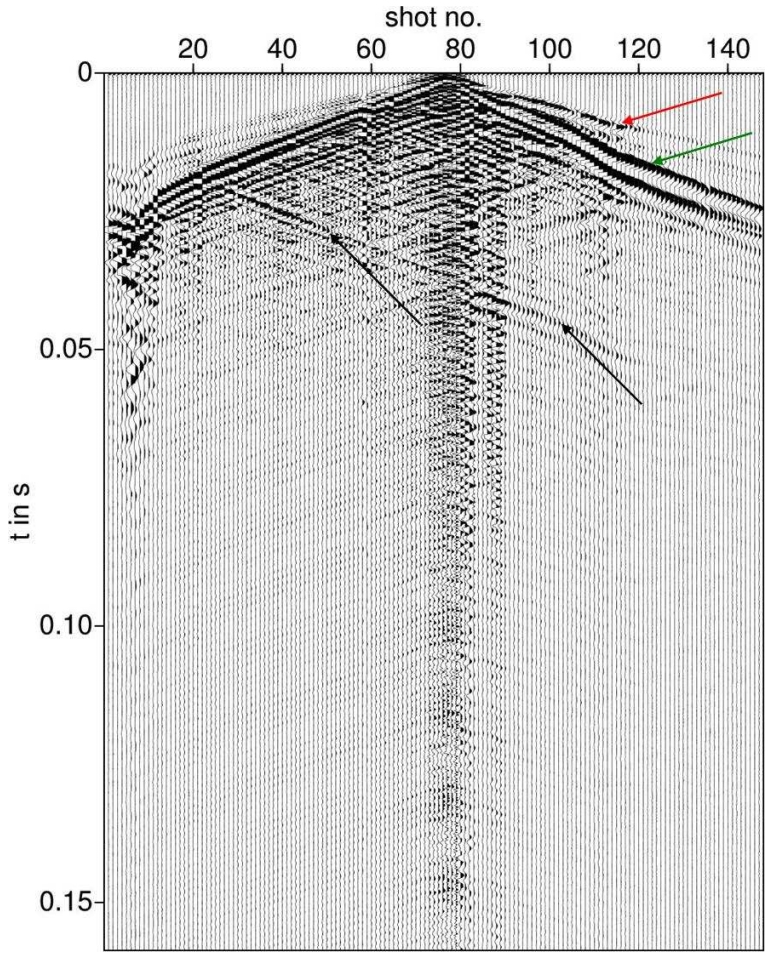

Figure 3.10: *Raw data of field file 8.*

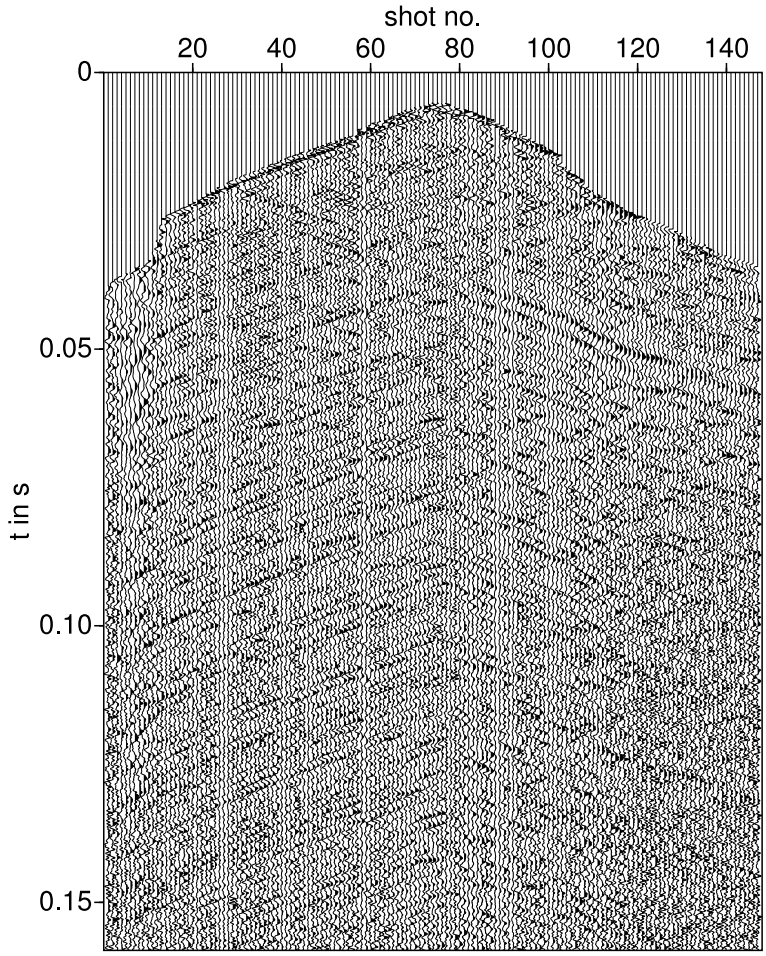

Figure 3.11: *Preprocessed data for field file 8.*

A 3D KPSDM was performed with the data. In order to do this we calculated the two-way travel time for each point of the 3D grid using the finite difference method of Podvin and Lecomte (1991). This was done for the P-velocity model as well as for the S-velocity model.

Each receiver gather was migrated separately and the final 3D image was obtained by stacking the migrated data taking into account either the true phase or the absolute value (see Figure 3.12 and 3.13). The tunnel is indicated along the x-axis, the y-axis is horizontal and perpendicular to the tunnel and the z-axis is vertical. Three perpendicular slices through the 3D volume are presented in both images. High amplitudes have the color red in Figure 3.13 while small amplitudes have the color blue. In Figure 3.12 the absolute value of the amplitudes is high when the color is red or blue and negligible amplitudes have the color green. The two black arrows in the image 3.13 point at reflections correlated with the gneiss transition. The inclination of these reflections

towards the x-axis is 37° while the slice through the tunnel wall occurs at 2900 m.

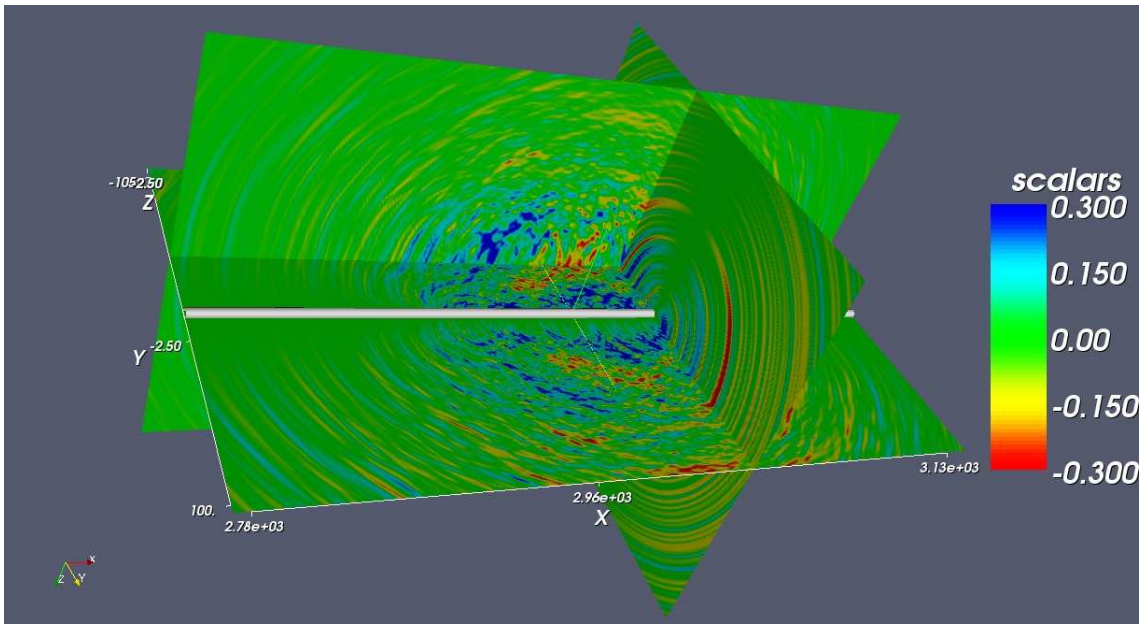

Figure 3.12: *KPSDM: Phase-stack. Scalars denote the amplitudes.*

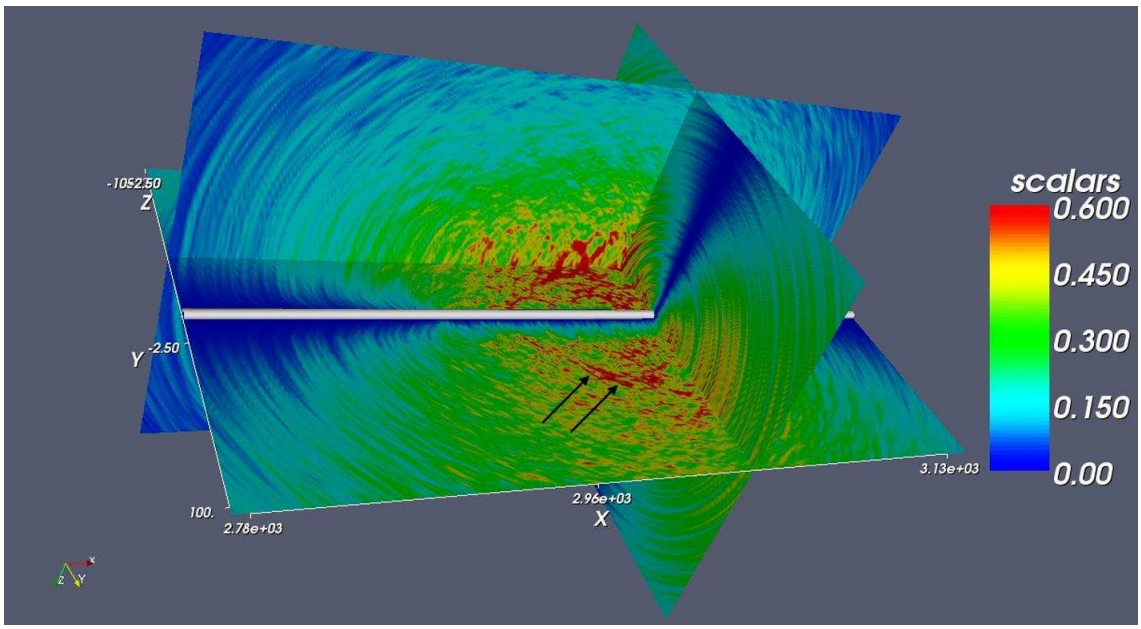

Figure 3.13: *KPSDM: Absolute-value-stack. Scalars denote the amplitudes.*

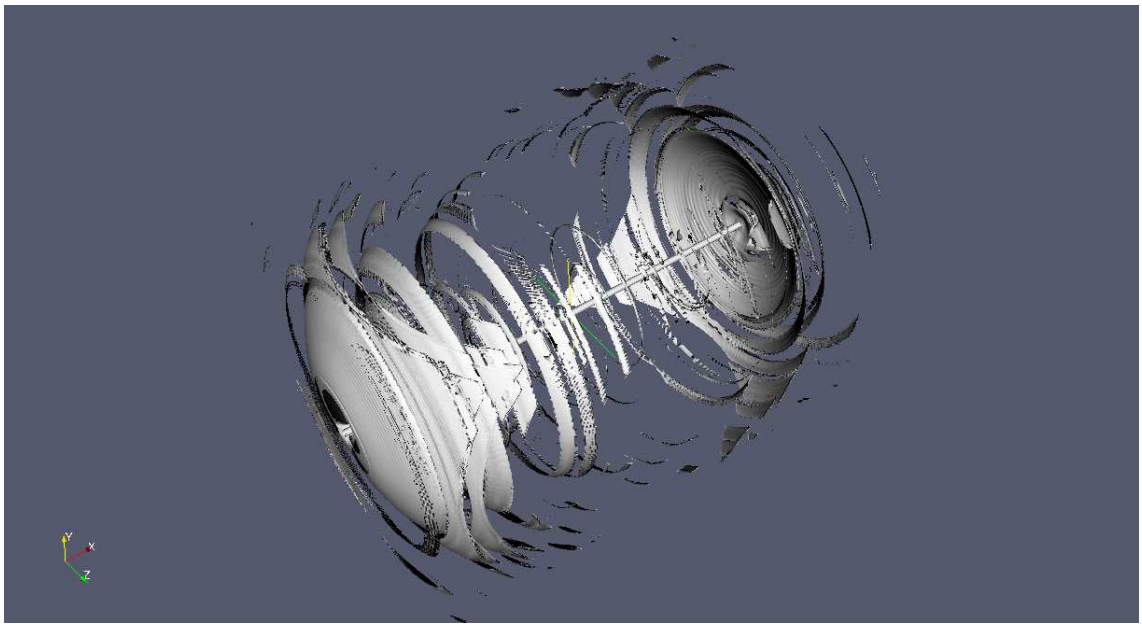

Figure 3.14: *Isosurface of reflections with high amplitudes in the 3D KPSDM volume (compressional wave velocity, phase-stack)*

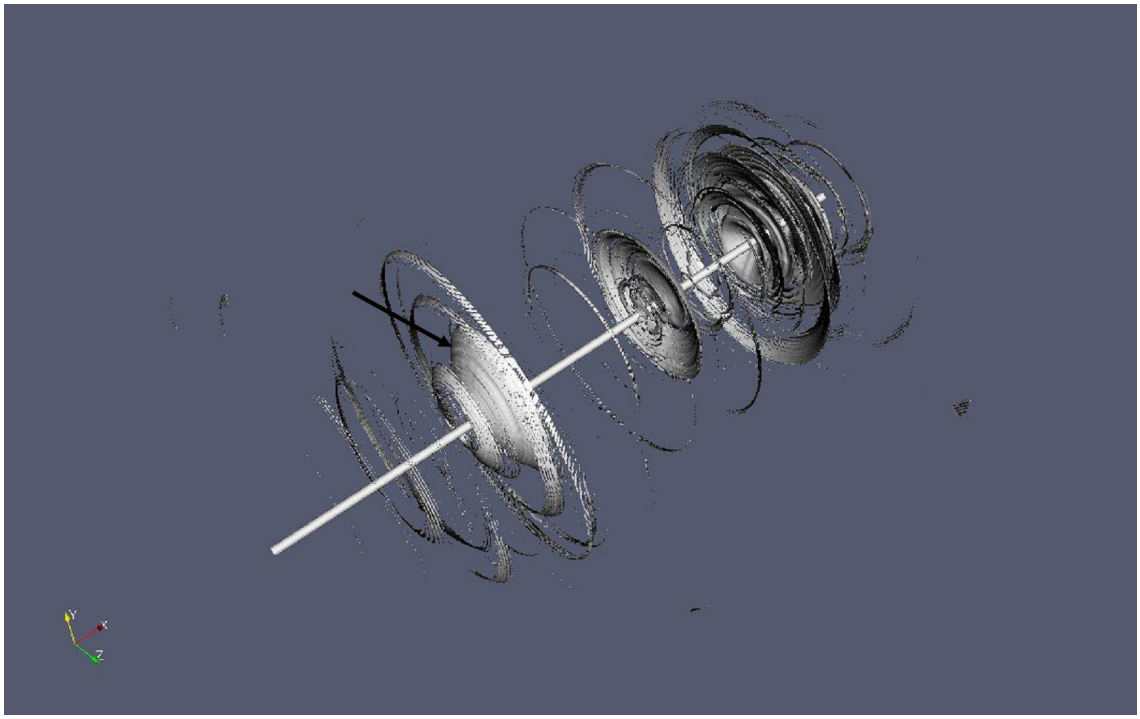

Figure 3.15: *Isosurface of reflections with high amplitudes in the 3D KPSDM volume (shear wave velocity, phase-stack). The black arrow signifies the reflector associated with the transition between Leventina and Lucomagno gneiss.*

As the angle of incidence is not considered by this method, reflectors appear as concentric shells around the tunnel (see Figure 3.14). Using the S-velocity model for Kirchhoff migration the isosurface indicated by the black arrow corresponds to the transition between two gneiss variations (Leventina - Lucomagno Gneiss, see Figure 3.15).

3.4 Reflection-Image-Spectroscopy

We extended 3D KPSDM by performing it over different narrow frequency bands. This approach is called Reflection-Image-Spectroscopy (RIS). It is a powerful tool in heterogeneous media in order to suppress scattering effects in the low frequency band and to increase the resolution in the high frequency band. The source, a pneumatic hammer, had a signal spectrum from 0 up to 1000 Hz. This was separated into 11 frequency bands by trapezoidal filters with a width of 200 Hz. The mean frequency increased from 100 Hz for the first band to 900 Hz for the last in increments of 80 Hz. Each band was migrated separately using KPSDM in a 3D model. The low frequency images (Figures 3.17 and 3.19) show much clearer and more intense reflections generated by the transition between two present gneiss variations. These are indicated by black arrows in the figures. Compared to the geological cross section shown in Figure 3.3 the slice through the tunnel wall of this geological feature is as expected from the geology at $x = 2900\,m$. The scatterers due to the gneiss crossing are much better visible in the RIS low-frequency-image (Fig. 3.17) than in the KPSDM image (Fig. 3.16).

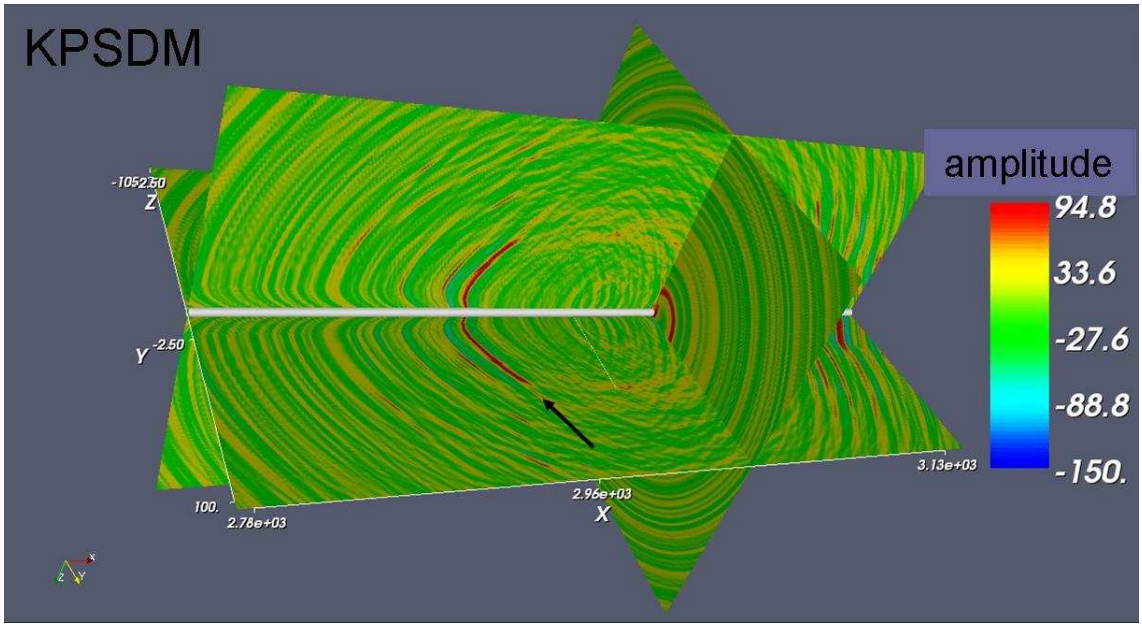

Figure 3.16: *KPSDM: Cross sections through the phase-stacked 3D migration volume (shear wave velocity). The black arrow points at the gneiss transition.*

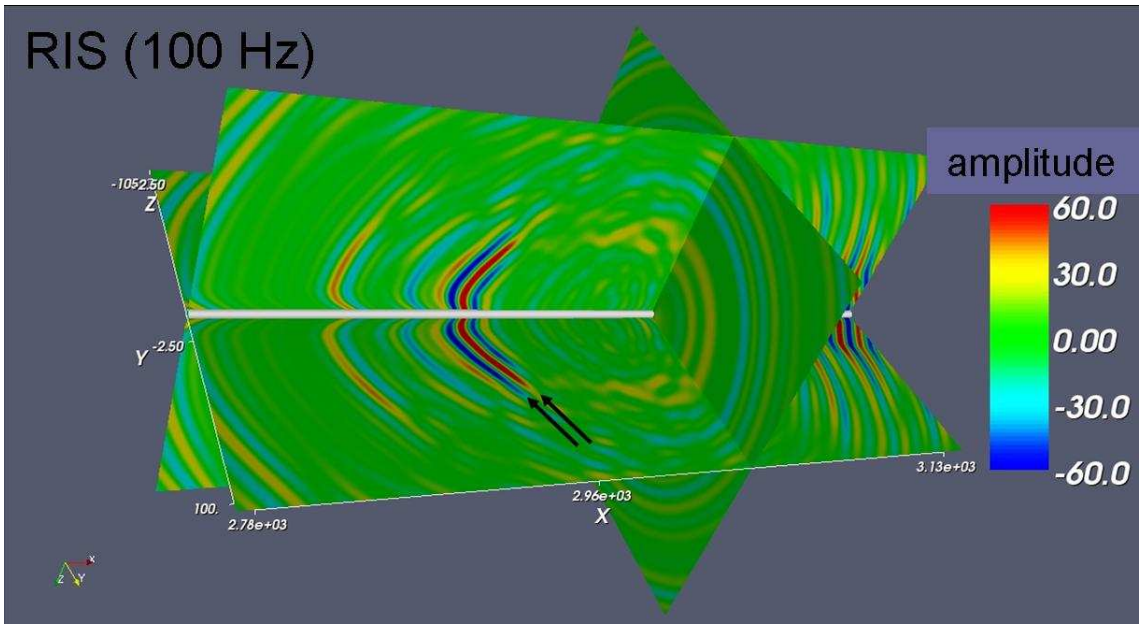

Figure 3.17: *RIS (100 Hz): The 2 arrows indicate the scatterers due to the gneiss crossing.*

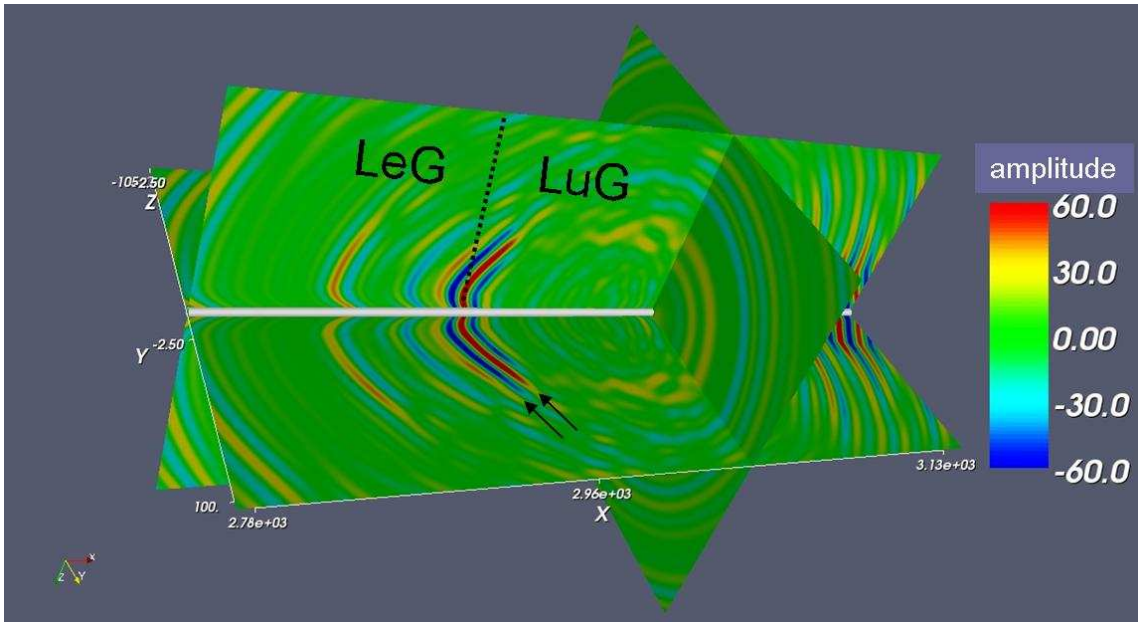

Figure 3.18: *RIS and geological features (Leventina Gneiss - Lucomagno Gneiss)*

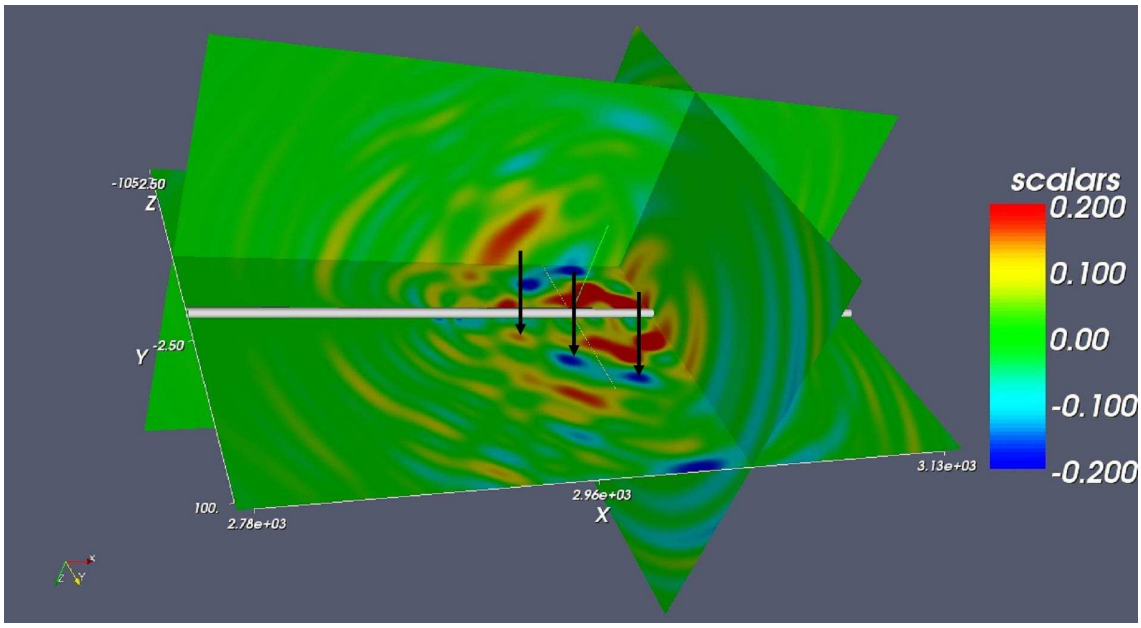

Figure 3.19: *RIS: Cross sections through the phase-stacked 3D migration volume (compressional wave velocity). Scatterers corresponding to the gneiss transition are indicated with black arrows. Scalars denote the amplitudes*

3.5 Fresnel Volume Migration

Fresnel Volume Migration (FVM) uses the emergence angles of reflections in order to restrict the smearing of energy to the physical relevant part in the 3D volume, which is the intersection of the isochrone surface and the first Fresnel Volume (see Figure 2.10). We implemented FVM in the 3D model. The emergence angles of reflections were calculated by a slowness and polarization analysis of the data. We were able to reproduce earlier results from FVM in a 2D model. Because of the acquisition geometry of receiver locations along a line only 2D direction estimates can be extracted out of the slowness calculation. First we derived these estimates along the tunnel via slowness calculations using a slant stack method. The 3 dimensional slowness vector is calculated through polarization analysis. The direction estimate of incoming signals was computed by the covariance matrix method as well as using averaged direction cosines (Jepsen and Kennett 1990; Rentsch 2007). The hodogram analysis of the Piora raw data set shows that using a time window corresponding to the dominant frequency allows a stable estimation of the polarization.

The definition of the covariance matrix is:

$$C = \begin{pmatrix} C_{xx} & C_{xy} & C_{xz} \\ C_{yx} & C_{yy} & C_{yz} \\ C_{zx} & C_{zy} & C_{zz} \end{pmatrix} \tag{3.1}$$

with

$$C_{ij} = \frac{1}{N} \sum_{t=1}^{N} u_i(t) \cdot u_j(t) \tag{3.2}$$

N: number of time samples in one dominant time period

u_{ij}: displacement in direction i,j

t: index of time sample

Every common receiver gather was migrated separately.

Rectilinearity is a measure of how accurate the direction estimates derived from the covariance matrix are:

$$R = 1 - \frac{\lambda_2 + \lambda_3}{2\lambda_1} \tag{3.3}$$

In the formula (3.3) the intermediate eigenvalue λ_2 and smallest eigenvalue λ_3 is related to the largest eigenvalue λ_1 of the covariance matrix. For a perfectly linearly polarized signal the largest eigenvalue λ_1 is much larger than the other eigenvalues. Hence the rectilinearity will have values close to one. For signals with elliptical polarizations the magnitudes of the eigenvalues will be much more similar and hence the rectilinearity decreases.

A very good rectilinearity was observed for all 15 common receiver gathers (see Figure 3.20). Other measures as the stability and planarity concerning the reliability of the direction estimates were computed and underlined the correctness of our results.

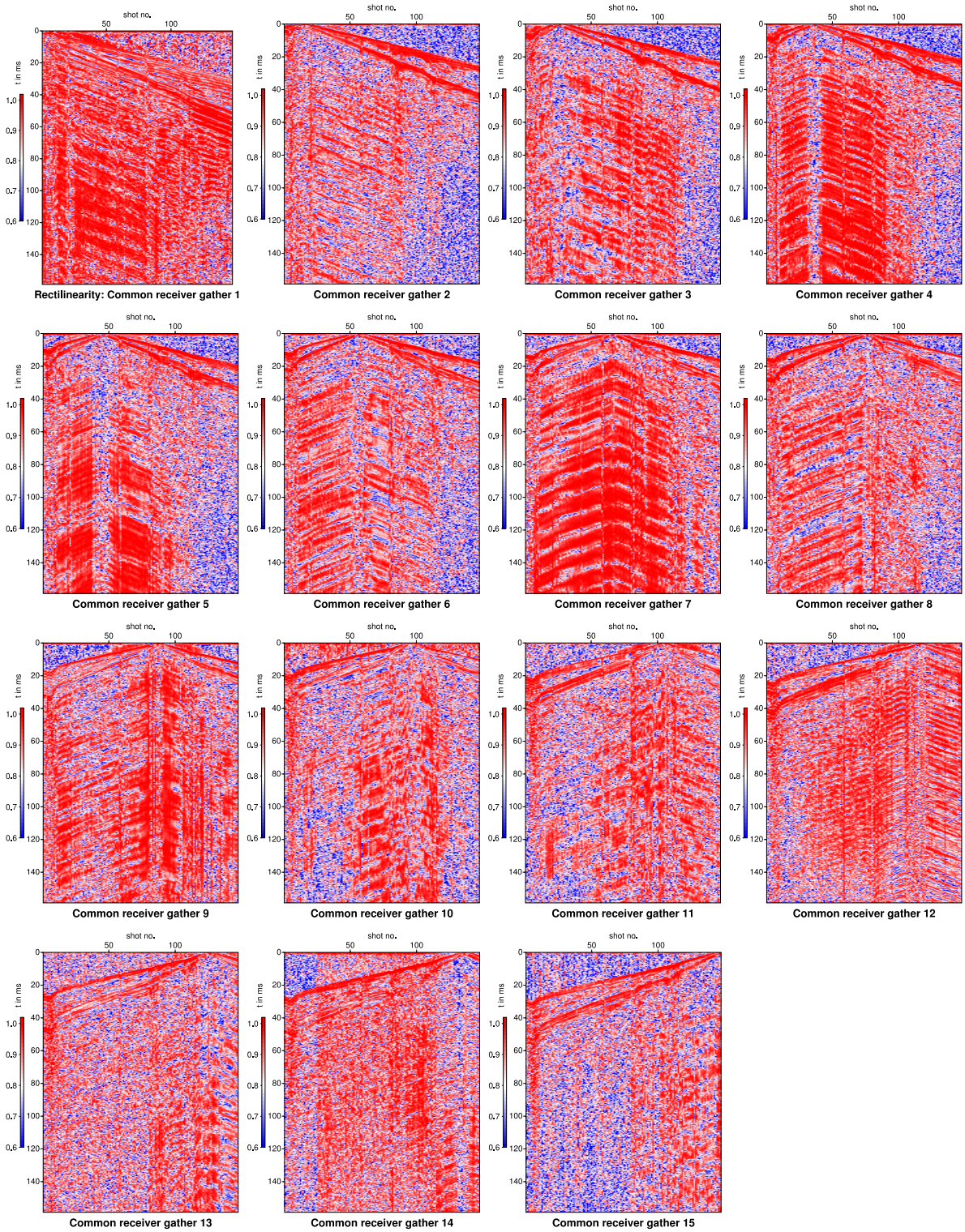

Figure 3.20: *Rectilinearity for common receiver gather 1-15 from left to right and from top to bottom.*

The phase-stack of the 15 receiver gathers compared with the geological structures at the tunnel wall is shown in Figure 3.21. High absolute values of amplitudes are indicated in red and blue while negligible amplitudes have the color green. In this image the location of the fault gouge at $x = 3105\,m$ as well as its perpendicular inclination toward the tunnel is mapped with high accuracy.

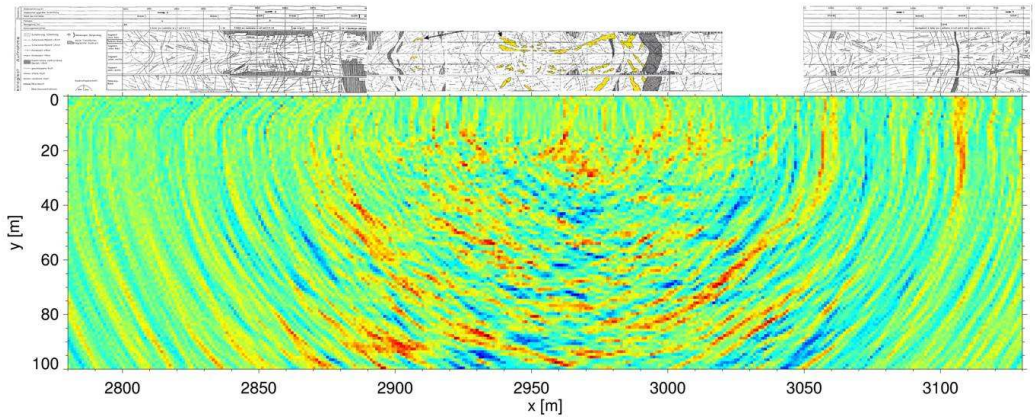

Figure 3.21: *Fresnel Volume Migration: Phase-stack of the 15 receiver gathers. We observe intense reflections corresponding to the fault gouge.*

The following 3 images illustrate how a reflector becomes visible only after rotating a horizontal slice in the 3D volume (see Figure 3.22, 3.23 and 3.24). The reflector is focused in a specific direction. This is a great benefit of FVM which focuses on the actual region of reflection.

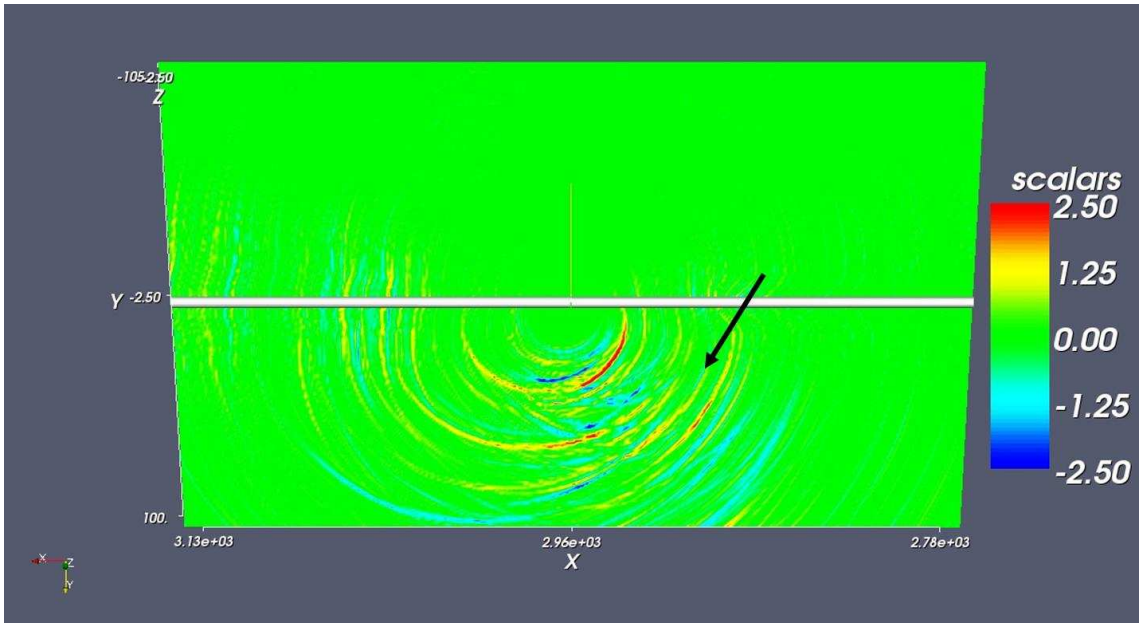

Figure 3.22: *Fresnel Volume Migration: Common receiver gather No. 8, horizontal slice in the source receiver plane. Scalars denote the amplitudes.*

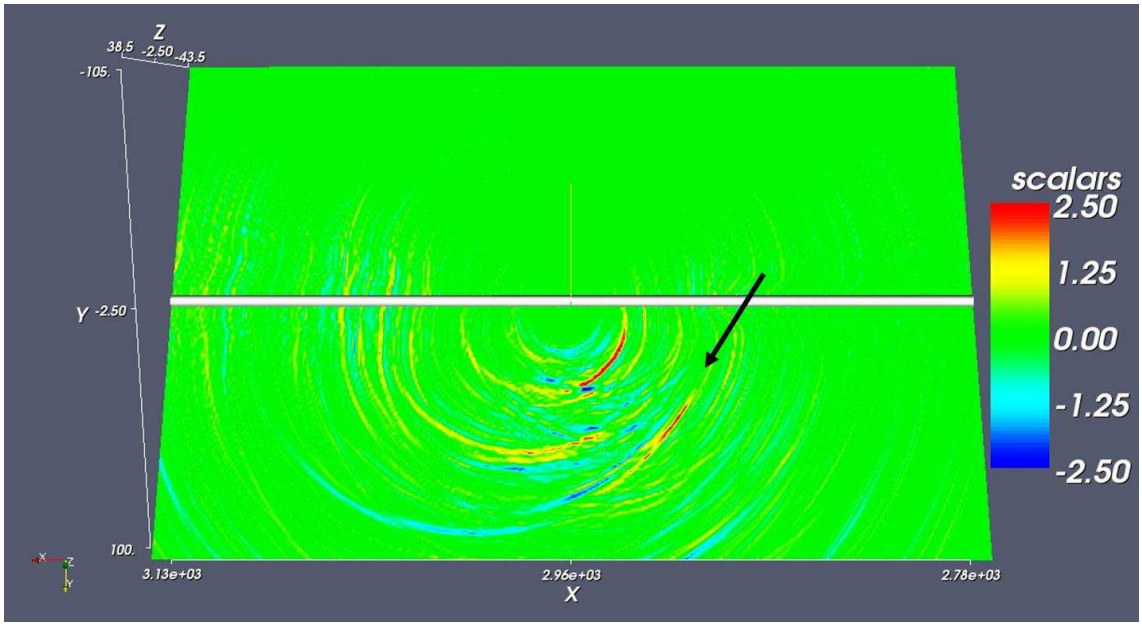

Figure 3.23: *Fresnel Volume Migration: Common receiver gather No. 8,* $21,8°$ *inclined plane to the horizontal, the reflector indicated by the black arrow becomes visible. Scalars denote the amplitudes.*

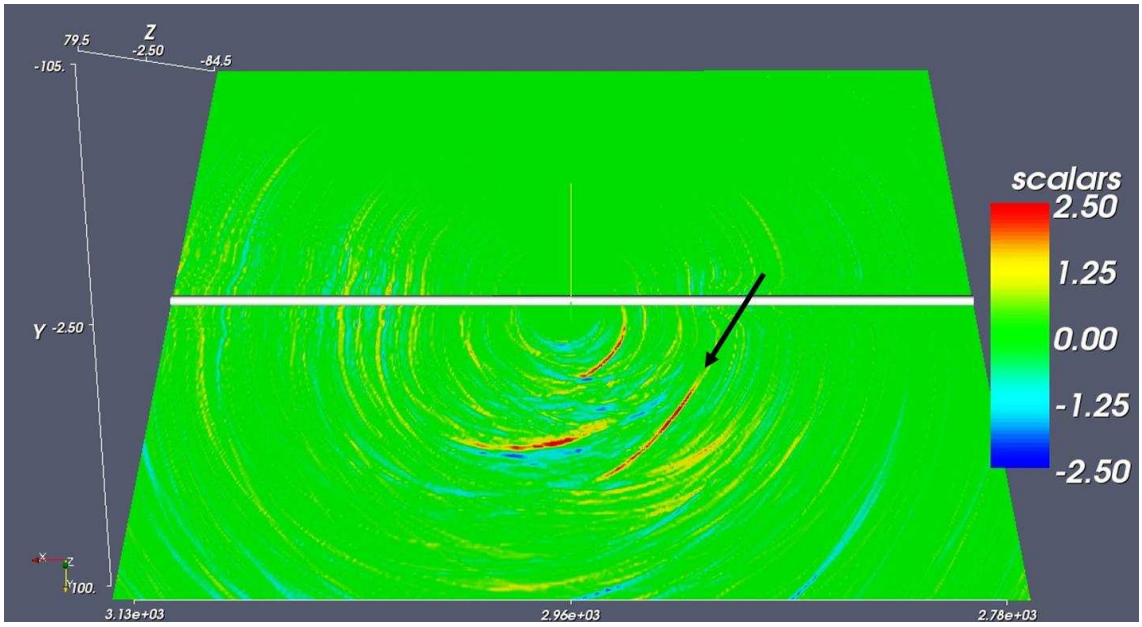

Figure 3.24: *Fresnel Volume Migration: Common receiver gather No. 8,* $38,66°$ *inclined plane to the horizontal, the reflector indicated by the black arrow has reached the maximum of his intensity. Scalars denote the amplitudes.*

The 2D slice through the source receiver plane of the FVM-volume resolves the gneiss crossing very precisely. The inclination with respect to the tunnel axis as well as the slice through the tunnel wall of the geological feature is mapped at $\alpha = 36°$ and $x = 2900\,m$ according to the geology as seen in Figure 3.25.

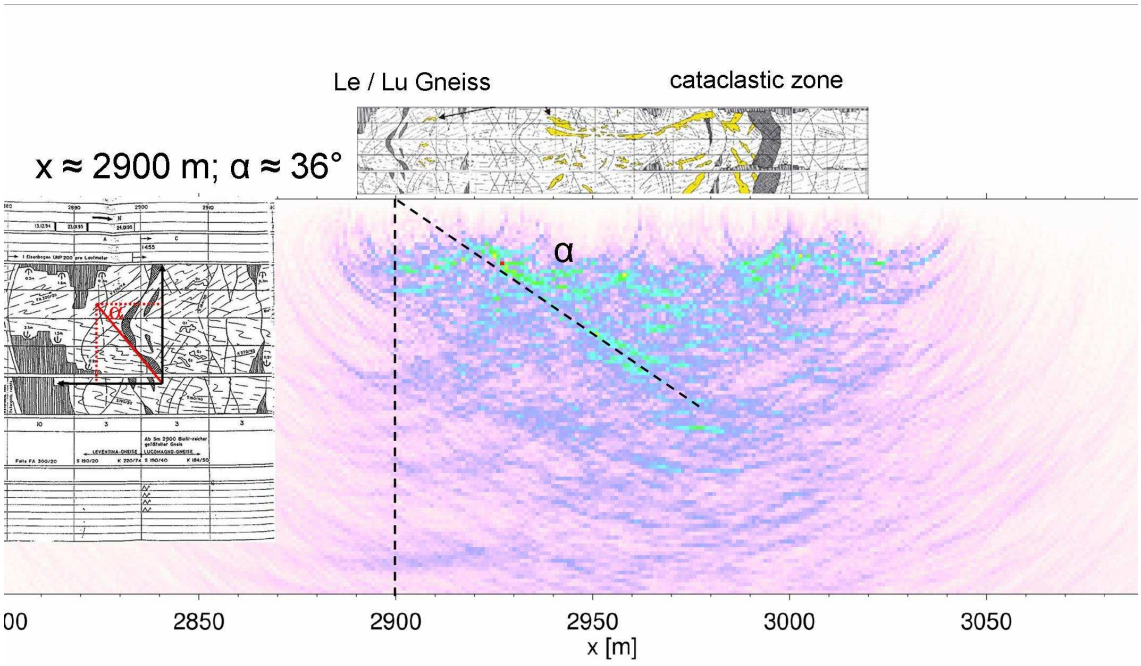

Figure 3.25: *Geological tunnel wall map and FVM: The location and orientation of the gneiss transition is mapped with high precision.*

Now we shall consider the spatial orientation of the gneiss transition in the x-z plane. From the geology we expect an angle toward the vertical z-axis of $\beta_{geo} = 20,96°$ (see Figure 3.26).

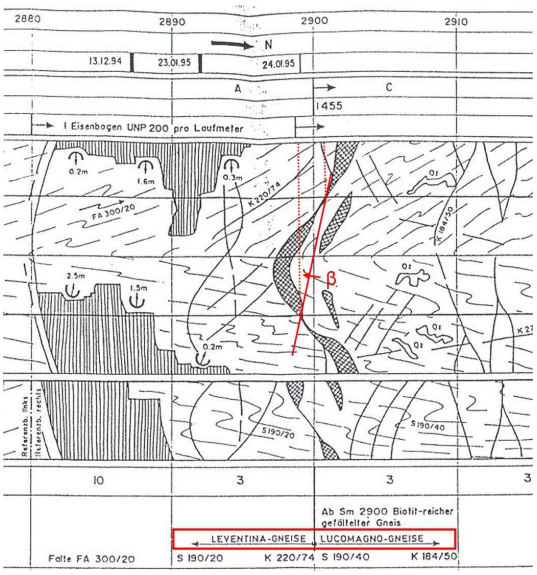

Figure 3.26: *Inclination of the gneiss transition toward the z-axis according to the geology.*

As we take a closer look on three perpendicular planes toward the y-axis, we observe a good coincidence of the measured angle β_{msd} with the angle expected from the geology β_{geo} (see Figures 3.27, 3.28 and 3.29).

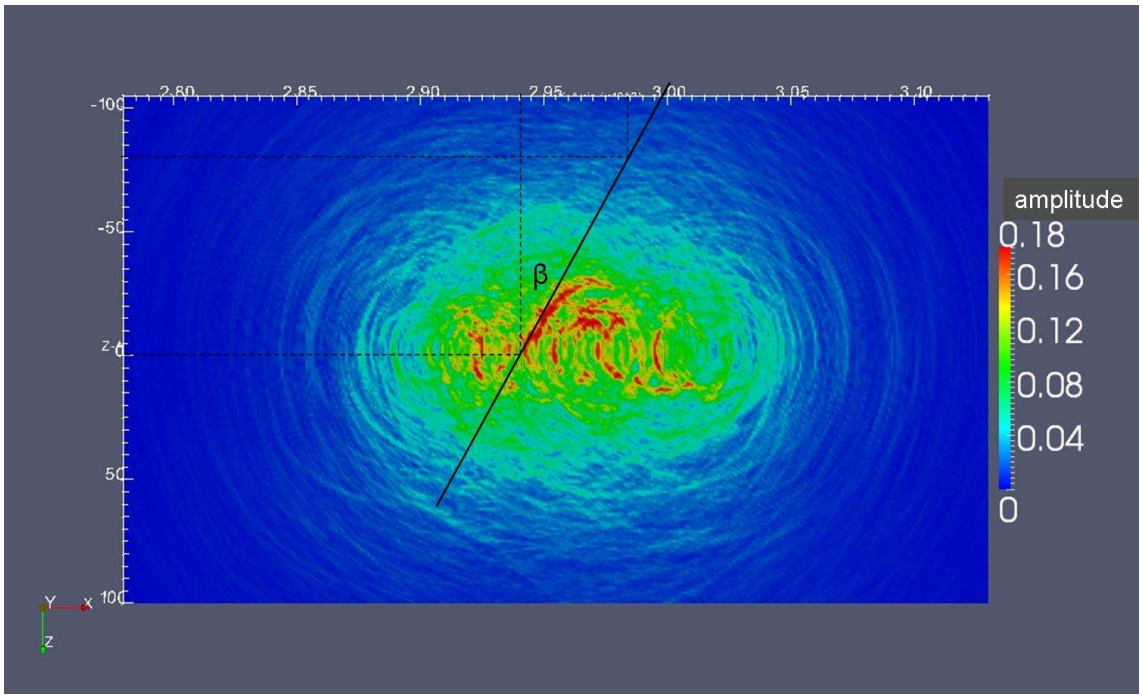

Figure 3.27: *Slice at $y = 30$ m. The measured angle between the gneiss transition and the vertical is $\beta_{msd} = 28,81°$.*

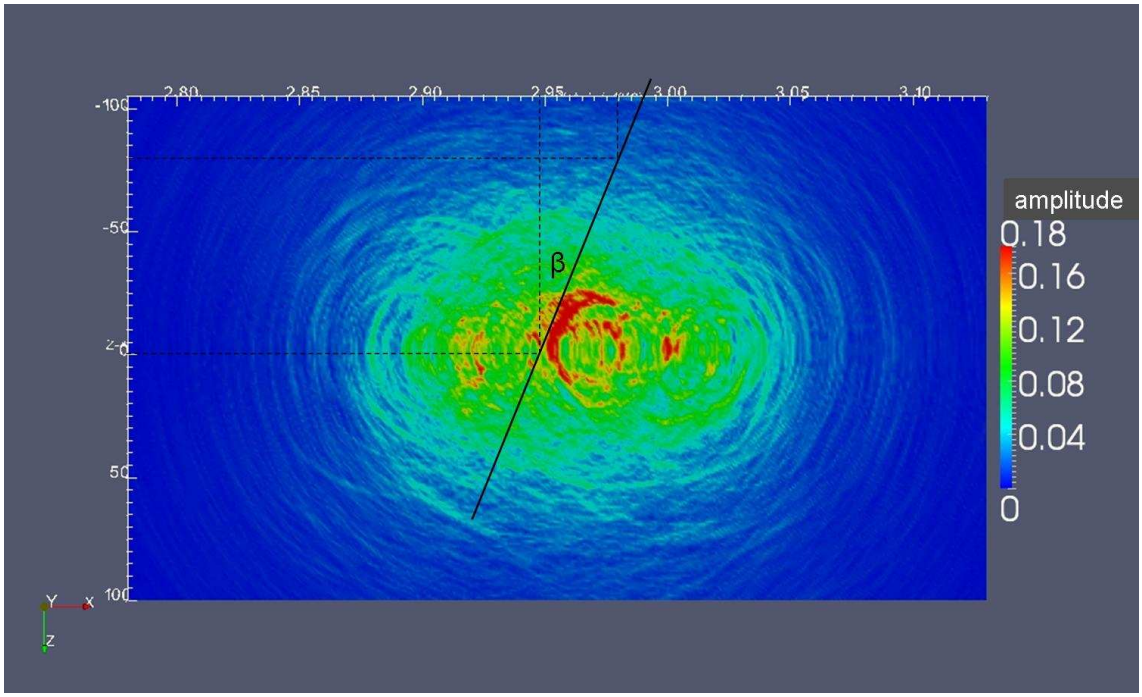

Figure 3.28: *Slice at $y = 35$ m. The measured angle between the gneiss transition and the vertical is $\beta_{msd} = 22,42°$.*

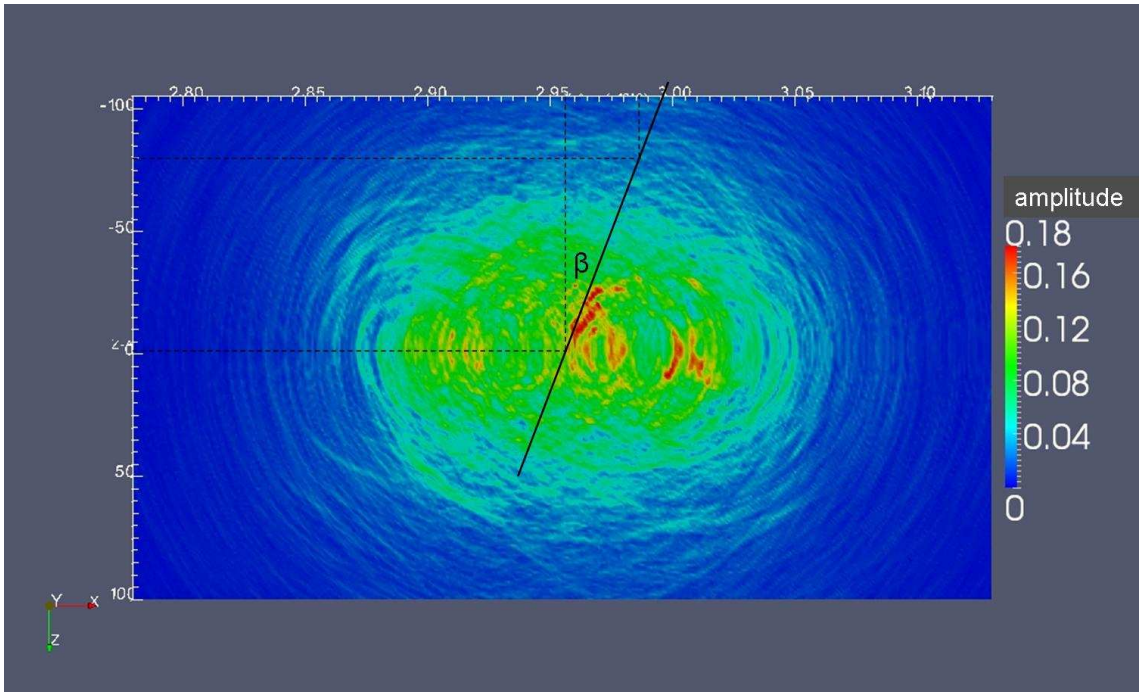

Figure 3.29: *Slice at $y = 45$ m. The measured angle between the gneiss transition and the vertical is $\beta_{msd} = 19,29°$.*

According to the relation:

$$\tan \beta_{msd} = \frac{\Delta x}{\Delta z} \tag{3.4}$$

the following values for β_{msd} could be obtained (see Table 3.1):

cut at y =	30m	35m	45m
β_{msd}	28,81°	22,42°	19,29°

Table 3.1: *Measured angle between the gneiss transition and the vertical for different slices in the x-z plane.*

We achieve an average angle of $\overline{\beta}_{msd} = 23,51°$, which coincides with the angle expected from the geology $\beta_{geo} = 20,96°$ quite well.

Figure 3.30 shows a x-y-slice through the 3D migration volume. A much clearer image of the reflectors related to the gneiss transition designated by 3 black arrows is obtained compared to the corresponding KPSDM images (see Figure 3.13). The slice in Figure 3.30 is rotated (Figure 3.31). Figure 3.32 shows the continuation of the gneiss crossing in the x-z plane and that the distribution of reflectors in 3D is no longer symmetrical but corresponds to the polarization information of the recorded seismic data. The gneiss transition is marked by two black arrows.

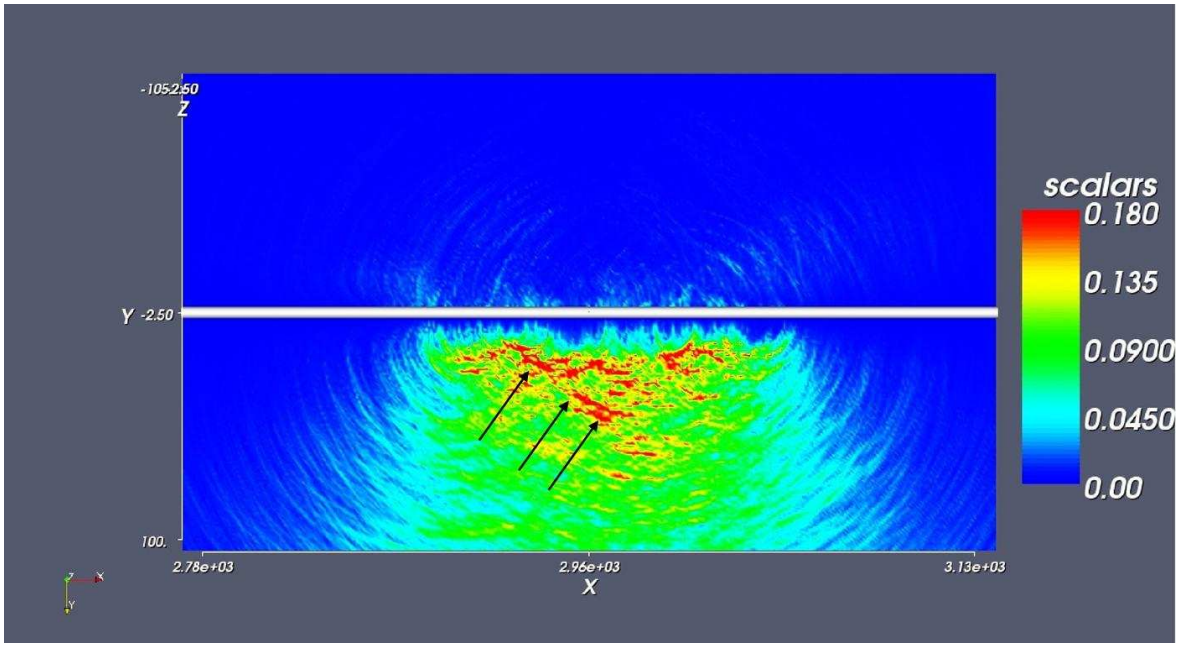

Figure 3.30: *Fresnel Volume Migration: absolute-value-stack of the 15 receiver gathers. We observe less spatial ambiguity and a higher resolution of most structures compared to KPSDM. Scalars denote the amplitudes*

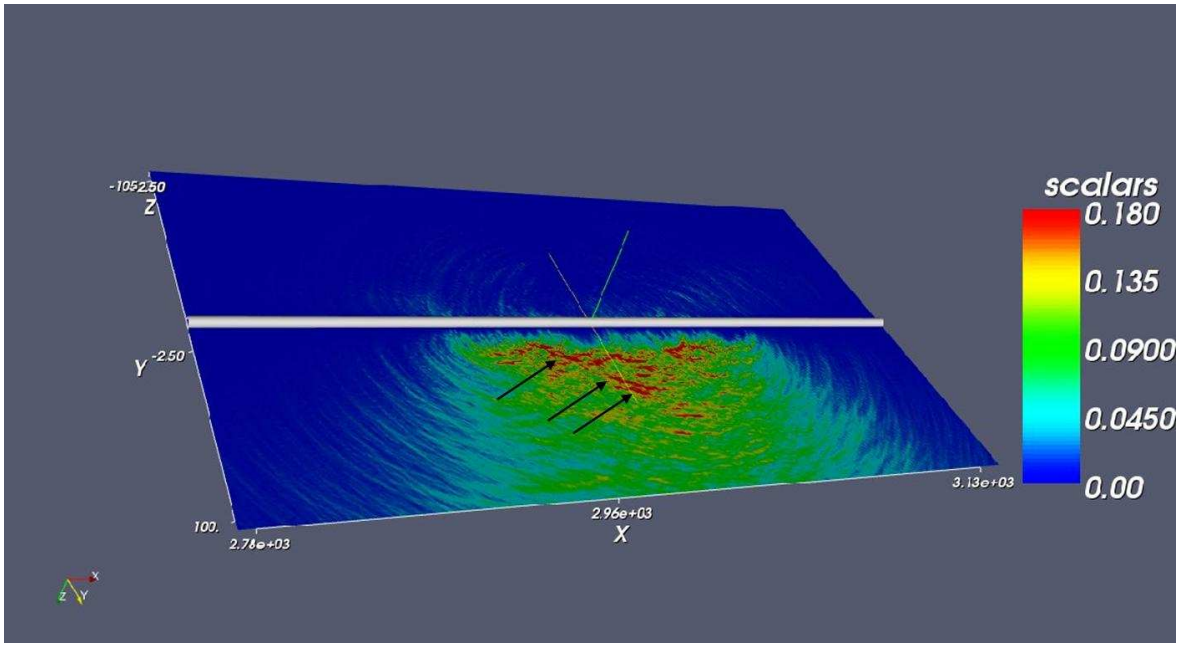

Figure 3.31: *Fresnel Volume Migration: x-y slice. Scalars denote the amplitudes.*

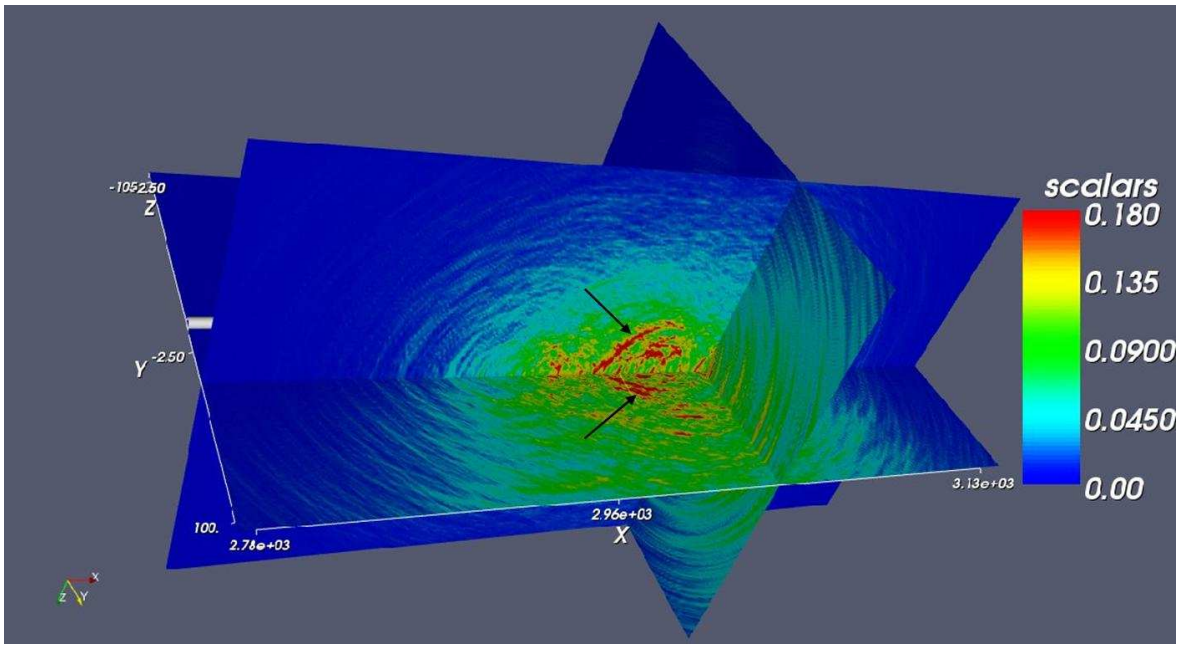

Figure 3.32: *Fresnel Volume Migration: x-y, y-z and x-z slices. Scalars denote the amplitudes.*

Another major geological feature can be seen in the geological map of the tunnel wall: the fault gouge (see Figure 3.4). We can observe that the fault gouge is not only mapped very well at tunnel meter 3105 in the FVM image but also the nearly symmetric orientation around the tunnel axis is imaged with high accuracy (see Figure 3.33).

We observe that the localization of reflectors is improved due to the focusing properties of FVM.

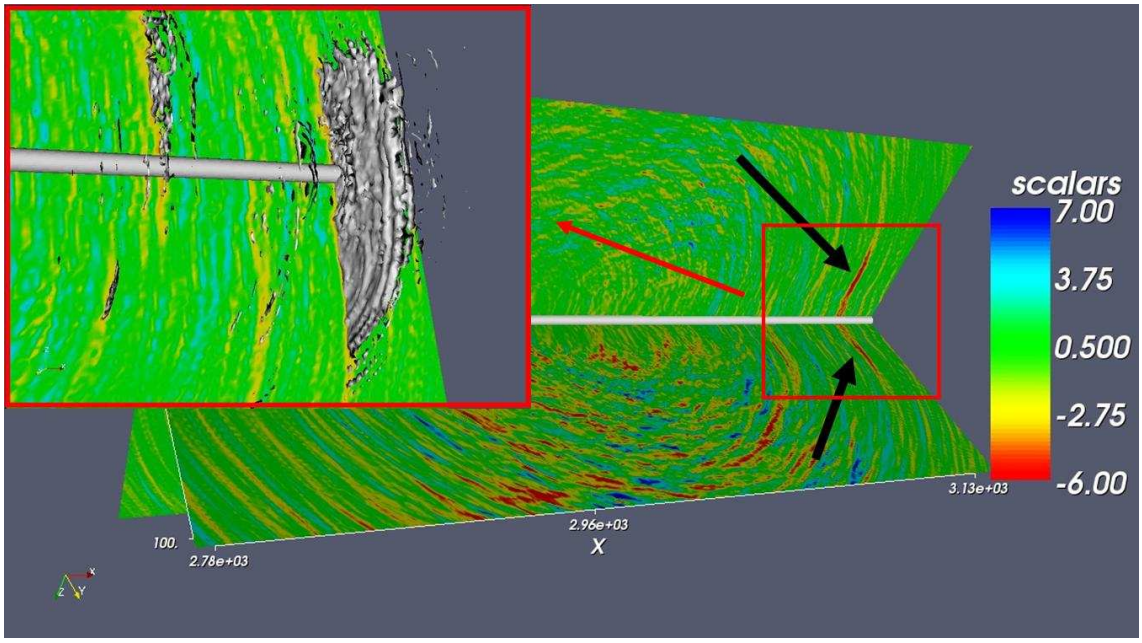

Figure 3.33: *FVM: Two Black arrows indicate the reflections corresponding to the fault gouge in two perpendicular slices and the drawn isosurface illustrates the possible shape of the fault gouge in 3D. Scalars denote the amplitudes.*

3.6 Combination of RIS and FVM

Each receiver gather was frequency filtered. For each frequency band polarization information was derived by applying the covariance matrix method. Then FVM was applied and the 15 migrated field files were stacked by taking into account the true phase or the absolute value of the amplitudes.

The transition between the two gneiss variations was very nicely and continuously imaged. In Figure 3.34 the correlation between the migration of the low frequency band and the recorded geology is presented.

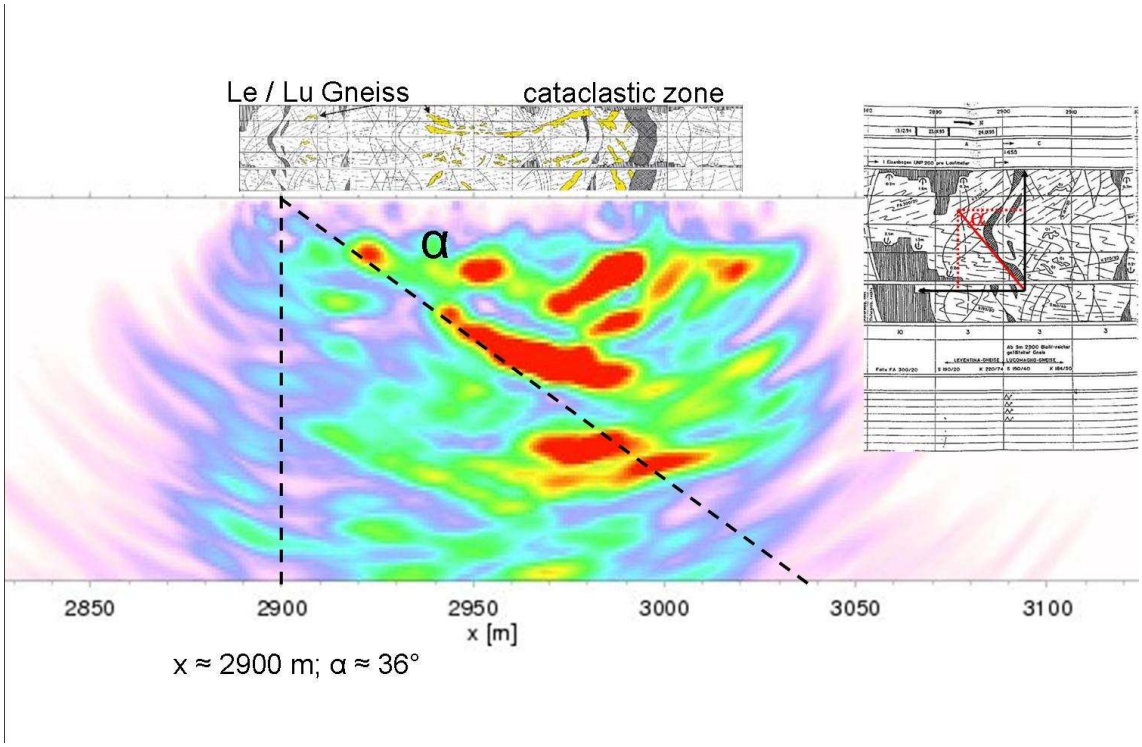

Figure 3.34: *RIS and FVM at 180 Hz mean frequency: Geology compared to the 2D slice through source receiver plane. The inclination to the tunnel axis as well as the slice through the tunnel wall of the gneiss transition is imaged according to the expectations.*

High amplitudes are marked in red and negligible amplitudes have the color white. In the upper right corner the geology between tunnel meter 2880 and 2920 is presented. The inclined, black, dashed line indicates the reflectors correlated with the gneiss transition. A strong reflection underneath the cataclastic zone between tunnel meter 2990 and 3000 can be connected to this geological feature. Again the inclination of the crossing of the gneiss types with respect to the tunnel axis and the slice of the transition zone through the tunnel at 2900 tunnel meters is mapped with high accuracy. Once again the

correctness of the migration method was confirmed and the reflector was imaged more continuous compared to the FVM of the whole frequency spectrum. The 3D image, Figure 3.35, shows a slice through the FVM-volume in the source receiver plane. The reflector corresponding to the gneiss transition indicated by two black arrows is clearly visible. Figure 3.36 illustrates the same slice from another perspective combined with an isosurface of high amplitudes. The most prominent isosurface marked by black arrows represents the spatial distribution of the gneiss transition in 3D. Another two planes perpendicular to the source receiver plane are added in Figure 3.37. Again the black arrows point at the reflector coinciding with the gneiss transition. The continuation of the reflector in the x-z plane is illustrated.

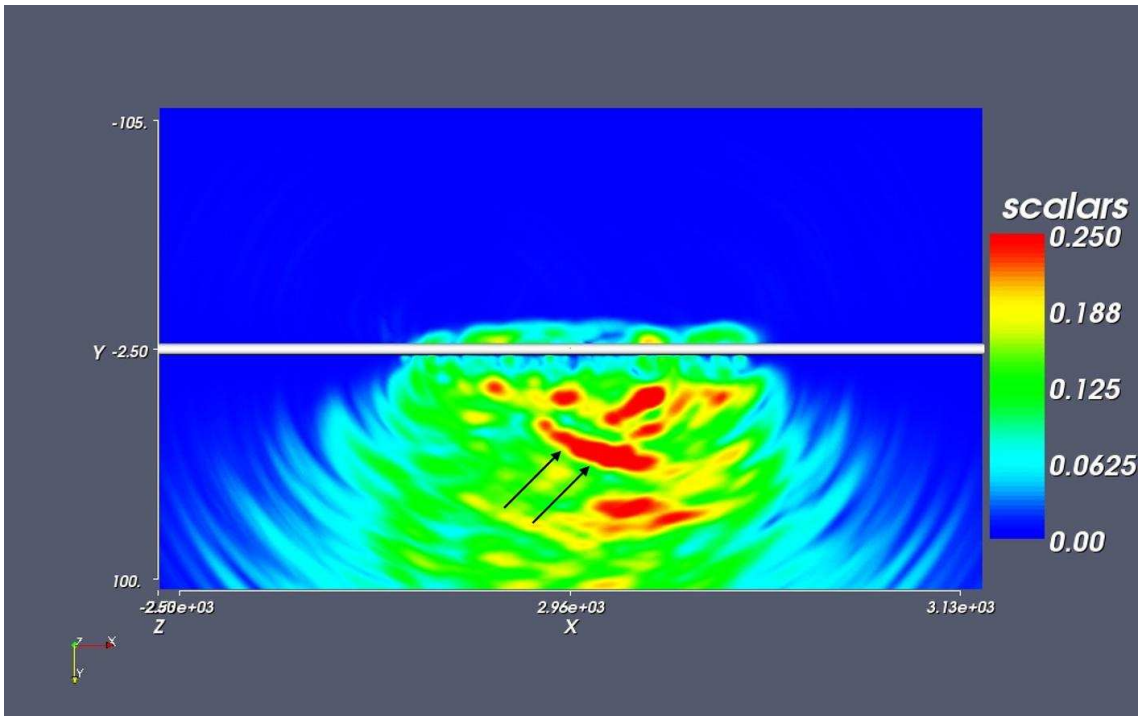

Figure 3.35: *RIS and FVM: Slice through the FVM-volume (source receiver plane). Scalars denote the amplitudes.*

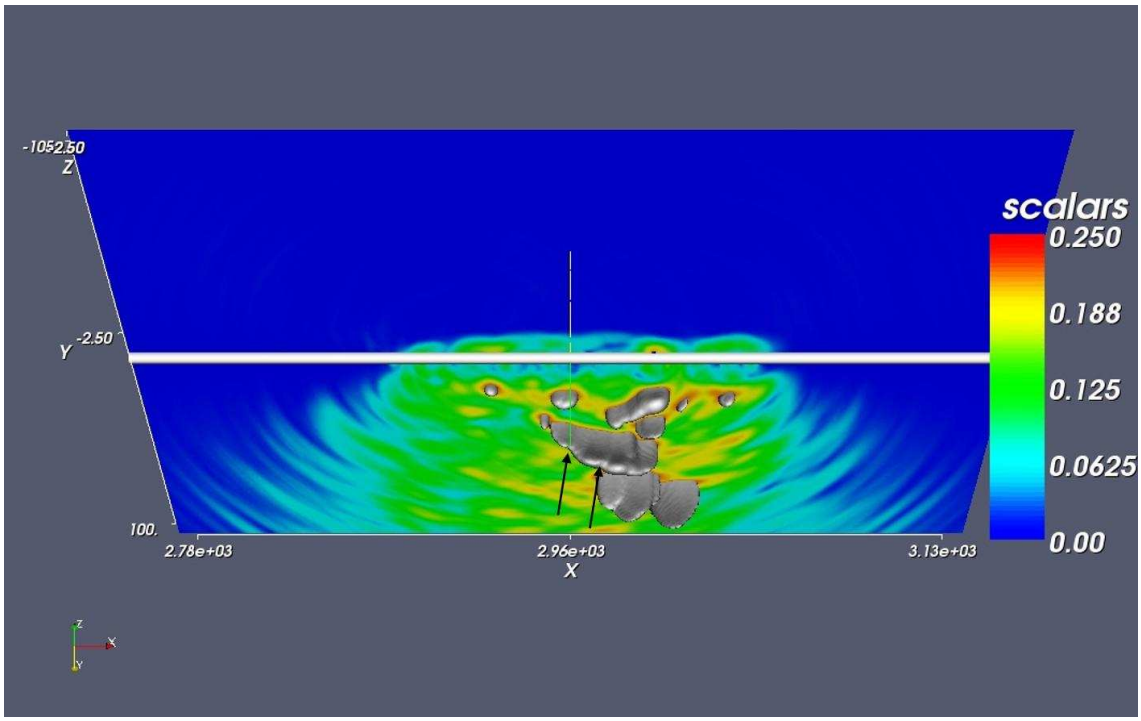

Figure 3.36: *RIS and FVM: One slice through the FVM-volume and isosurface of high amplitudes. Scalars denote the amplitudes.*

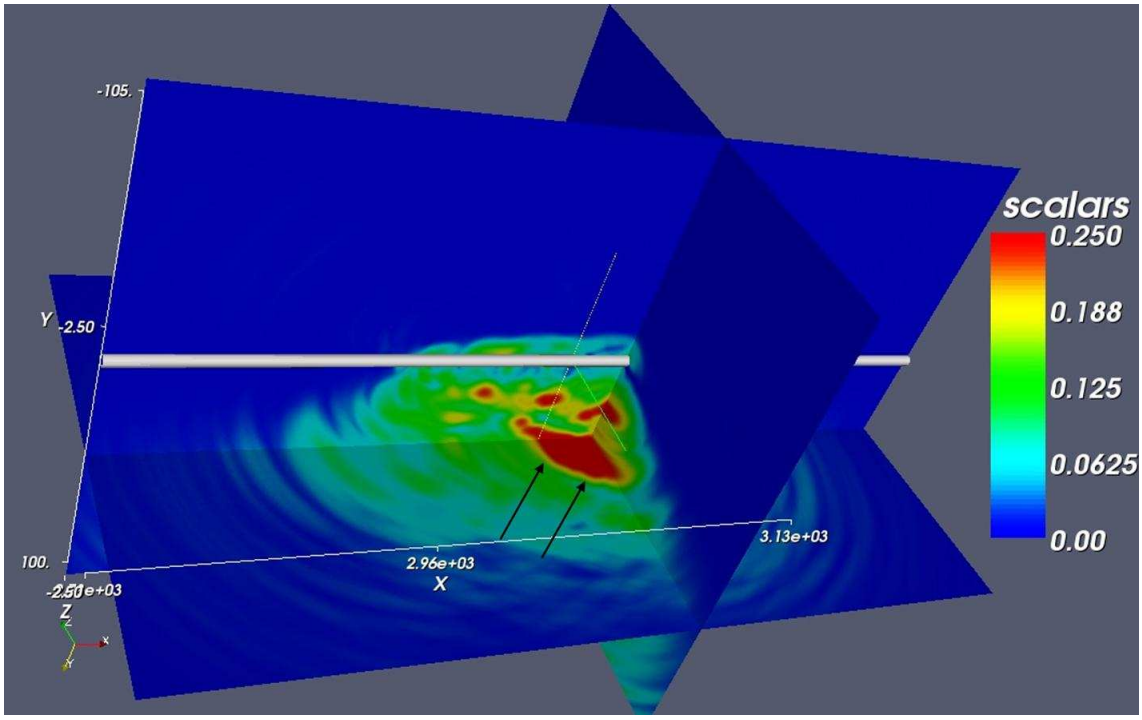

Figure 3.37: *RIS and FVM: Three slices through the FVM-volume. Scalars denote the amplitudes.*

3.7 P-S wave separation

A P-S wave separation algorithm was performed on the AGC and normalized data by taking into account the slowness vector $\vec{p}_{slow}$ and the polarization vector $\vec{p}_{pol}$ derived from the raw data. The dot product was calculated and if the two vectors happened to be parallel or nearly parallel (absolute value of angle θ between $\vec{p}_{slow}$ and $\vec{p}_{pol}$ smaller than 30° or greater than 150°) data corresponding to P-waves was extracted. In the case that the two vectors happened to be nearly perpendicular ($60° < |\theta| < 120°$) a accumulation of signals related to S-waves was performed.

$$cos\theta = \frac{\vec{p}_{slow} \cdot \vec{p}_{pol}}{|\vec{p}_{slow}||\vec{p}_{pol}|} \tag{3.5}$$

Taking into account only events corresponding to the above mentioned intervals led to many discontinuities in the separated wavefields. In order to avoid this we introduced a weighting function for the extracted P- (weighting function: $|cos(\theta)|$) as well as for the S-wavefield (weighting function: $|sin(\theta)|$). This tapering resulted in two more smooth wavefields without significant discontinuities (see Figure 3.38).

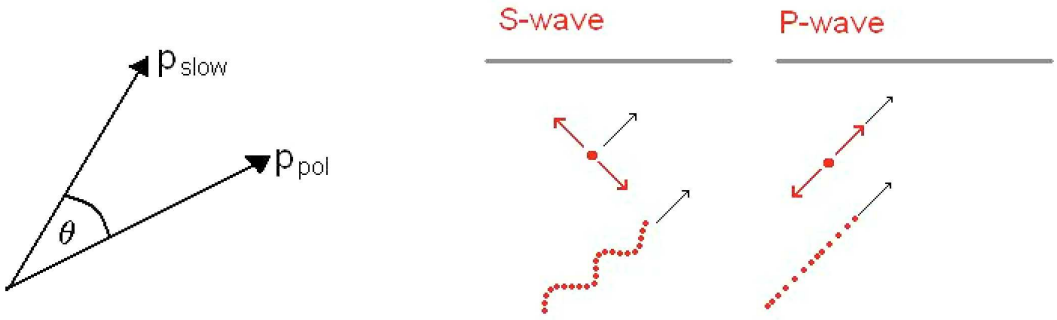

Figure 3.38: *Left: Slowness and polarization vector. Right: Illustration of shear wave and compressional wave, wave vector is indicated as red arrow and direction of wave propagation as black arrow.*

In Figure 3.39 and 3.40 a Kirchhoff migrated common receiver gather (no. 8) of the entire data set and only extracted P-wave related events can be observed. It becomes evident that geological relevant structures are focused (see red arrows pointing at reflections related to the gneiss transition) and artifacts are reduced (see green arrows).

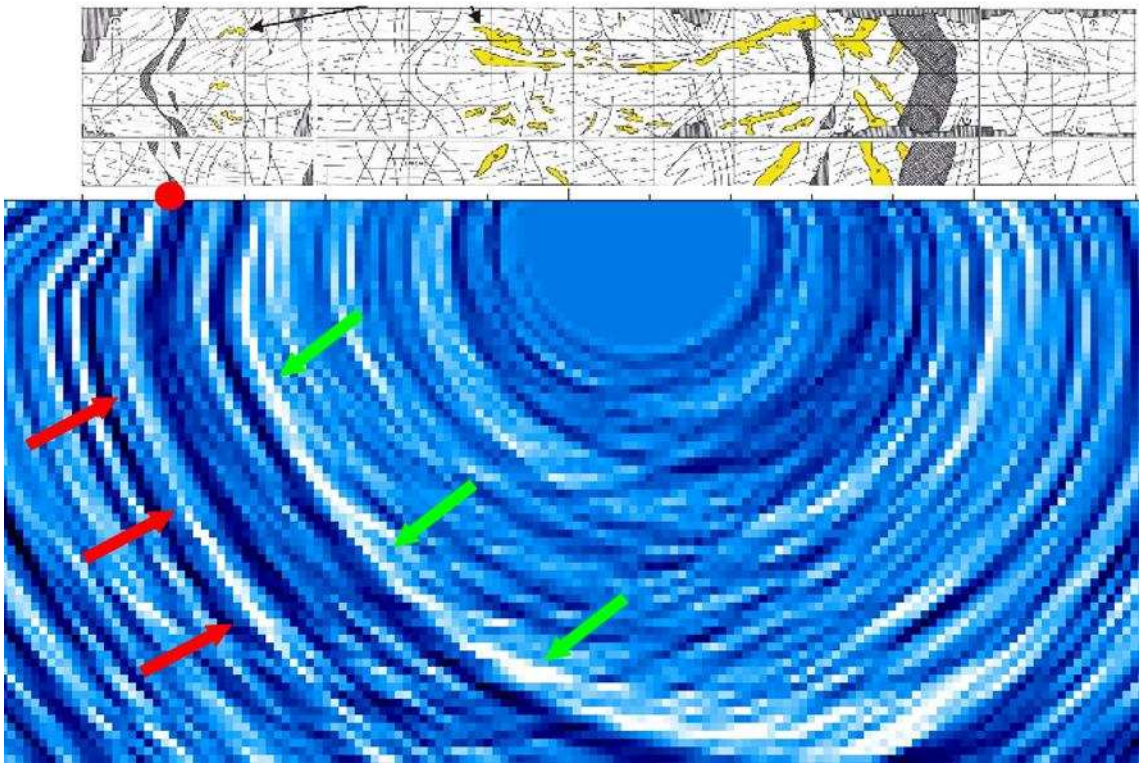

Figure 3.39: *P-S wave separation: field file no. 8, Kirchhoff Migration, entire wavefield*

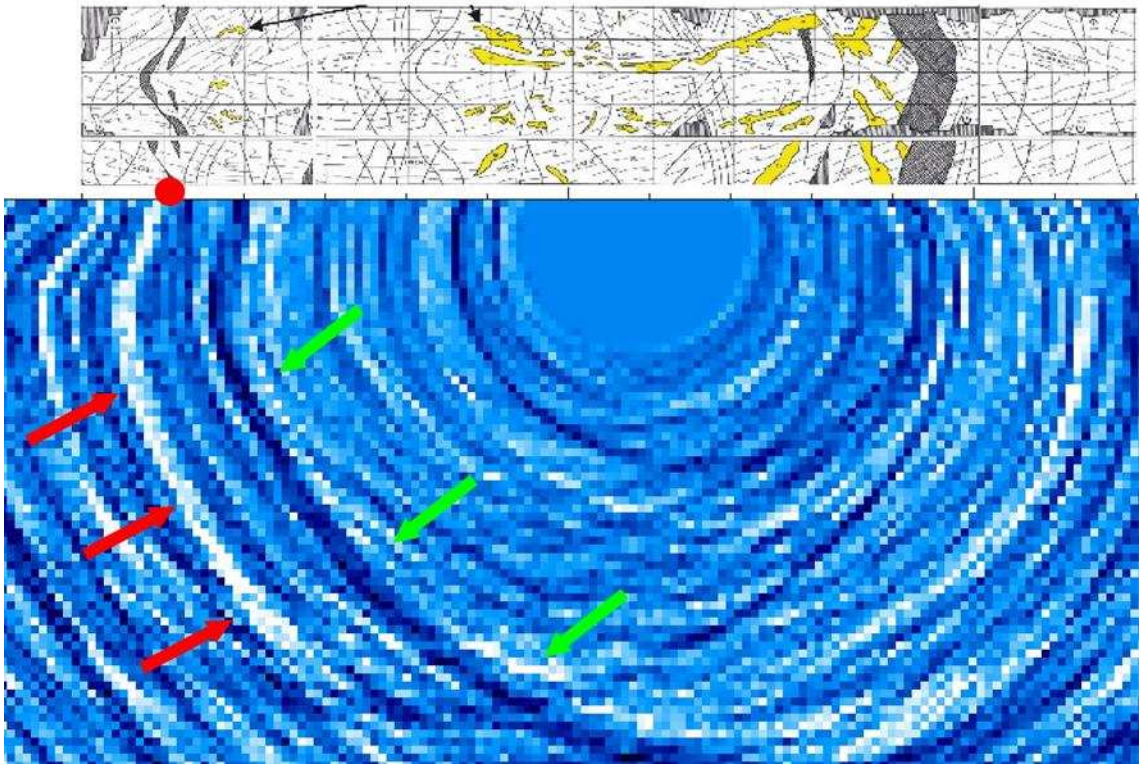

Figure 3.40: *P-S wave separation: field file no. 8, Kirchhoff Migration, separated P-waves*

The separation algorithm applied on the FVM images yields a much better mapping of the cataclastic zone. This is seen in Figure 3.41 especially after zooming in the relevant region.

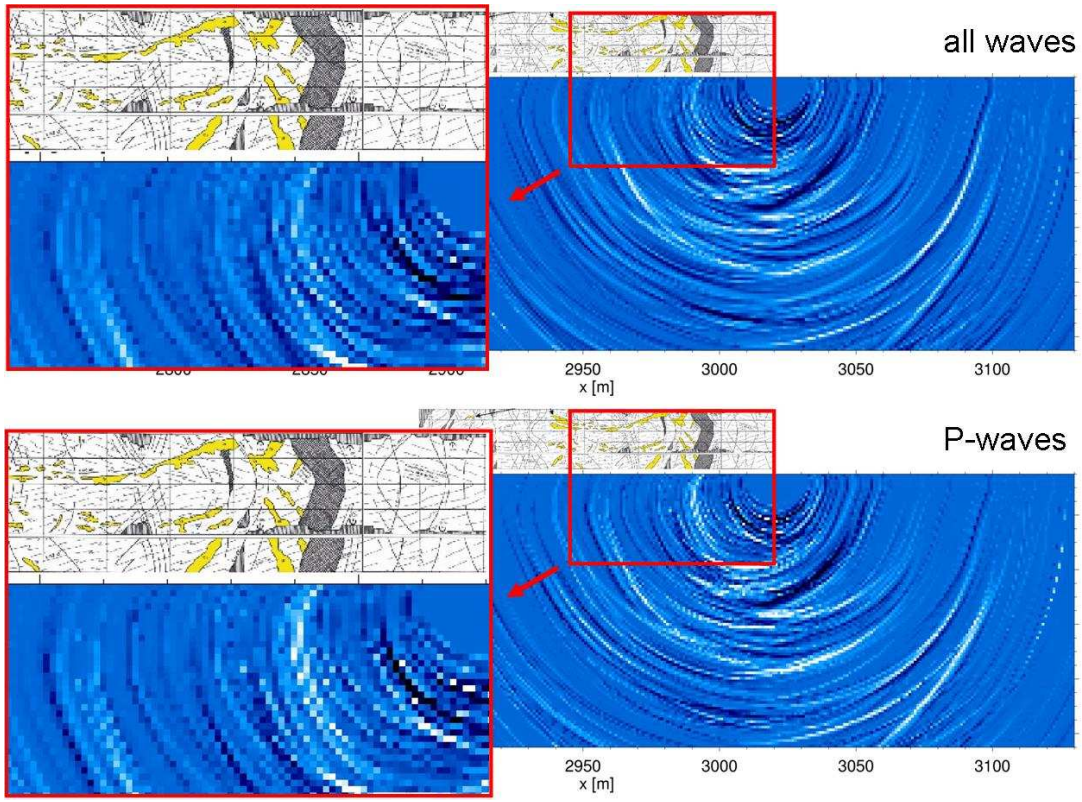

Figure 3.41: *P-S wave separation: FVM, upper image entire wavefield, lower image separated P-waves (zoom)*

3.8 Summary and conclusions

KPSDM has proven to be a useful tool for highly complicated environments. We show that one can further improve seismic images by extending this method. The frequency dependent images obtained by the RIS technique enable us to detect the transition between two gneiss variations in close vicinity of the tunnel. Unfortunately the high frequency images didn't show an increased resolution because the gneiss is a strongly diffuse scatterer for high frequencies. In the images obtained by FVM the spatial ambiguity of reflections is strongly reduced and the resolution is improved. These benefits are of great importance in a tunnel environment due to the very low data coverage. The combination of RIS and FVM yields a more continuous and prominent image of the main reflection. The separation of P- and S-waves offers a more pronounced image of the cataclastic zone.

Chapter 4

The Piora gallery data set

The survey layout is shown in Figure 4.1. 148 source points and 17 three-component receivers were used. The source point interval was $1\,m$ and the receiver interval approximately $10\,m$. The time sampling was $dt = 62\,\mu s$ and the total amount of time samples per trace was $nt = 3556$.

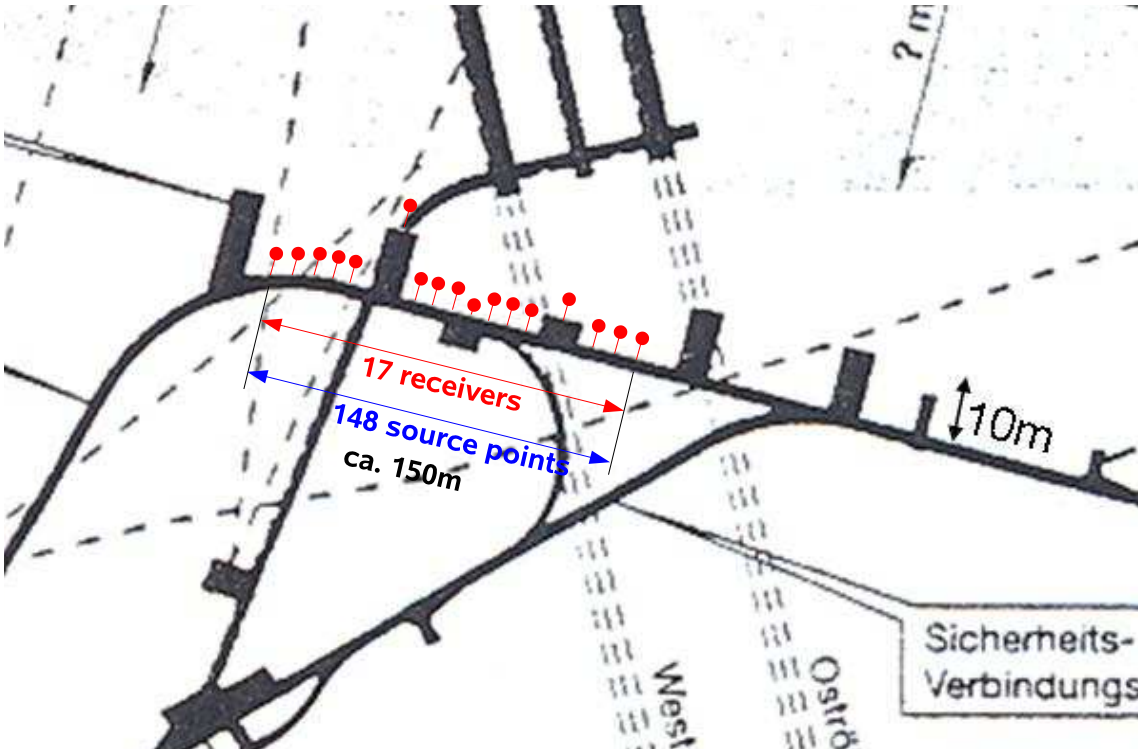

Figure 4.1: *Acquisition geometry for the Piora gallery data set.*

The data set was preprocessed by muting the first arrivals, then applying an AGC to the data and afterwards normalizing each trace to its maximum. The resulting seismic data before and after implementing the preprocessing steps for field file 9 can be observed in Figures 4.2 and 4.3.

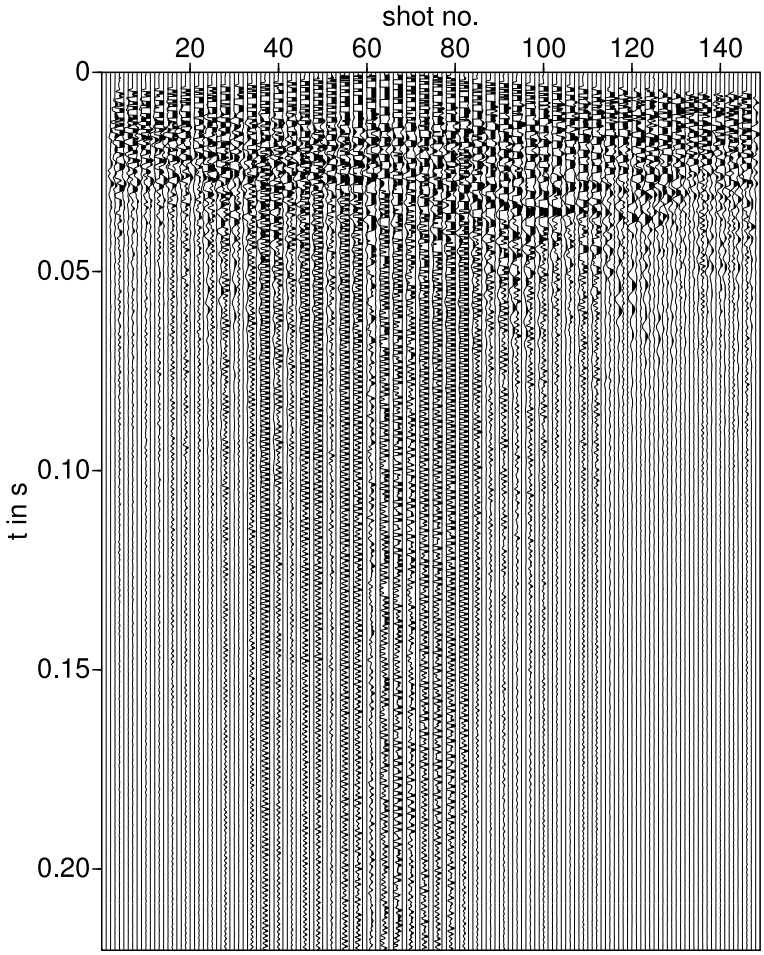

Figure 4.2: *Seismic traces of field file 9, raw data.*

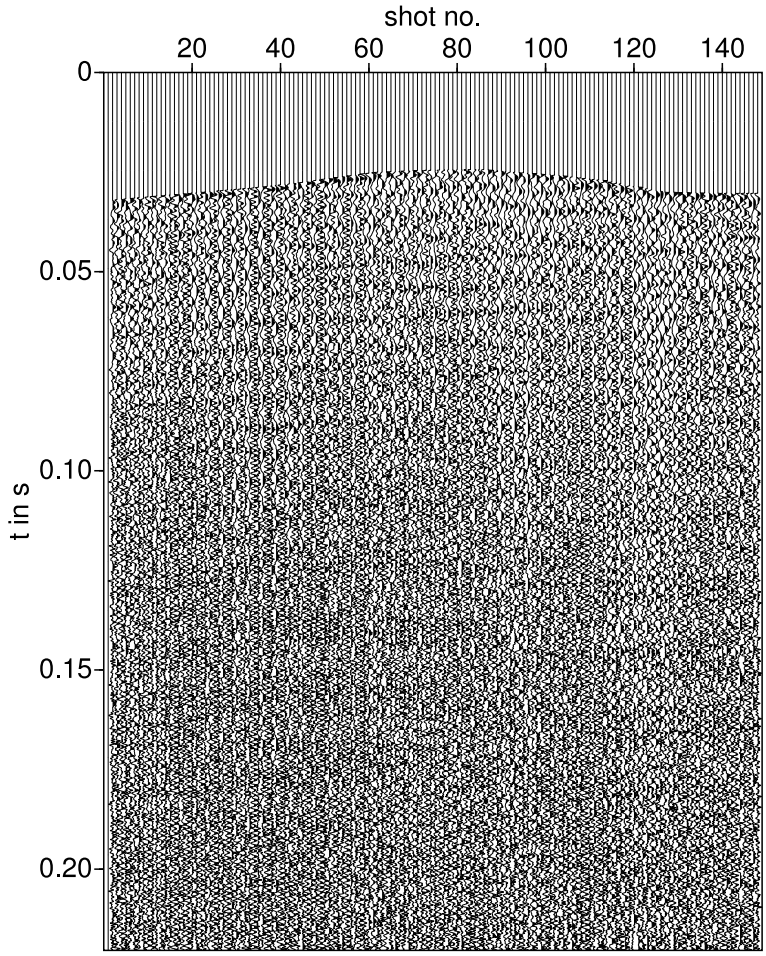

Figure 4.3: *Preprocessed seismic traces of field file 9.*

4.1 Velocity model

We calculated the first break theoretically by the formula:

$$T(x) = \frac{2}{a} \cdot ln \left[\frac{ax}{2v_0} + \sqrt{1 + \left(\frac{ax}{2v_0} \right)^2} \right] \tag{4.1}$$

In expression 4.1 a is the velocity gradient and v_0 is the velocity on the surface. By comparing the calculated first break with the seismograms we obtained the best fit using the parameters $a = 15,38\,1/s$ and $v_0 = 5000\,m/s$ for the P-velocity model and $a = 20,51\,1/s$, $v_0 = 2000\,m/s$ for the S-velocity model (see Figure 4.4).

The 3D velocity grid was created using the formula:

$$v(r) = v_0 + a \cdot (r(y, z) - 2, 5) \tag{4.2}$$

Here r is the radial distance from the tunnel axis and the radius of the tunnel is 2,5 m. Figures 4.5 and 4.6 show a slice through the 3D grid in the x-y plane for the P- and S-velocity model respectively.

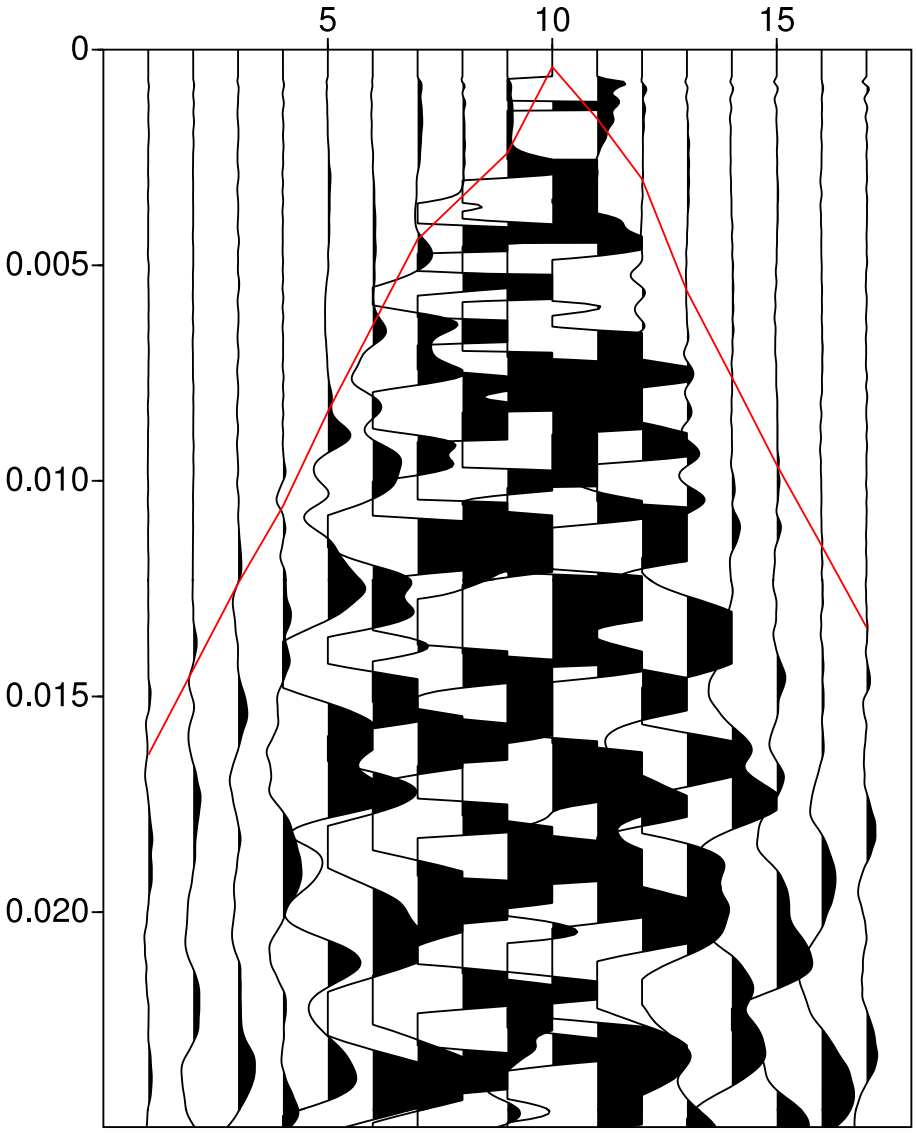

Figure 4.4: *The fit of the first break (red line) regarding P-waves with the above mentioned parameters.*

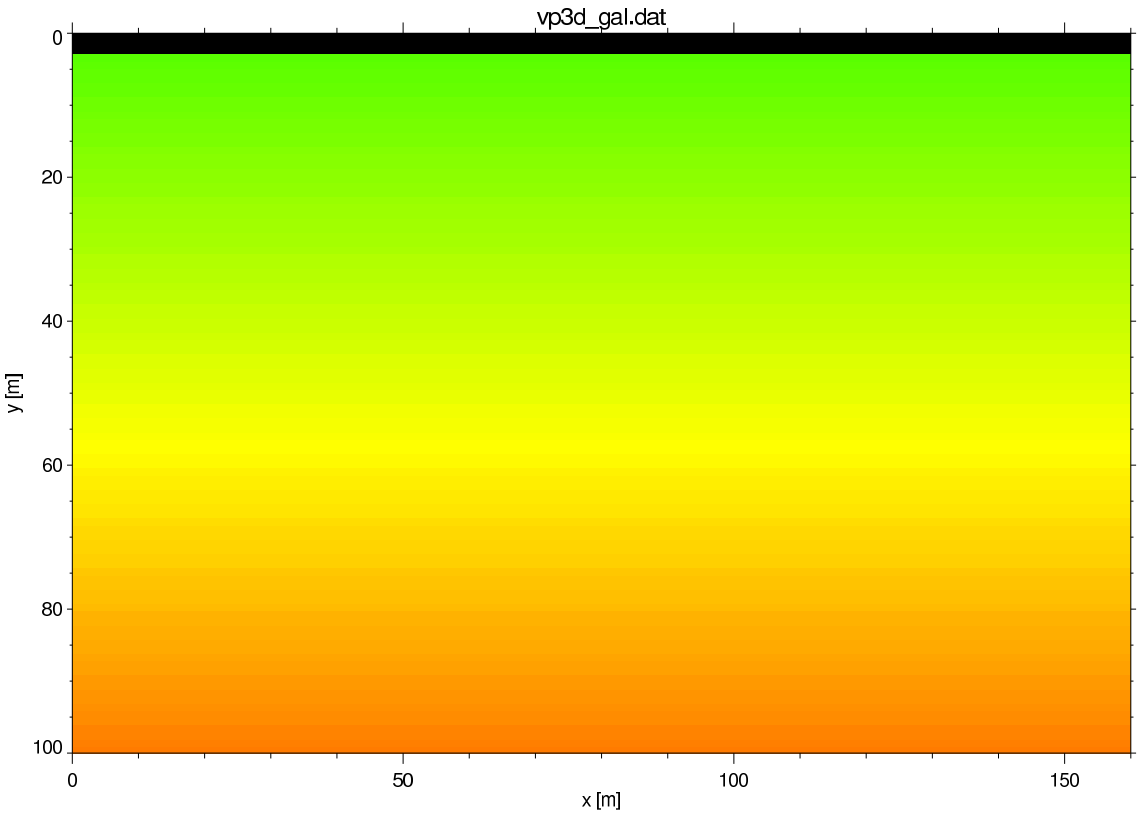

Figure 4.5: *P-velocity model for the Piora gallery data set. The velocity in the 3D model ranges from* $5000\ m/s$ *(green) to* $7137,25\,m/s$ *(red) (*$z = 0$*,* $v_{max} = 6500\ m/s$*).*

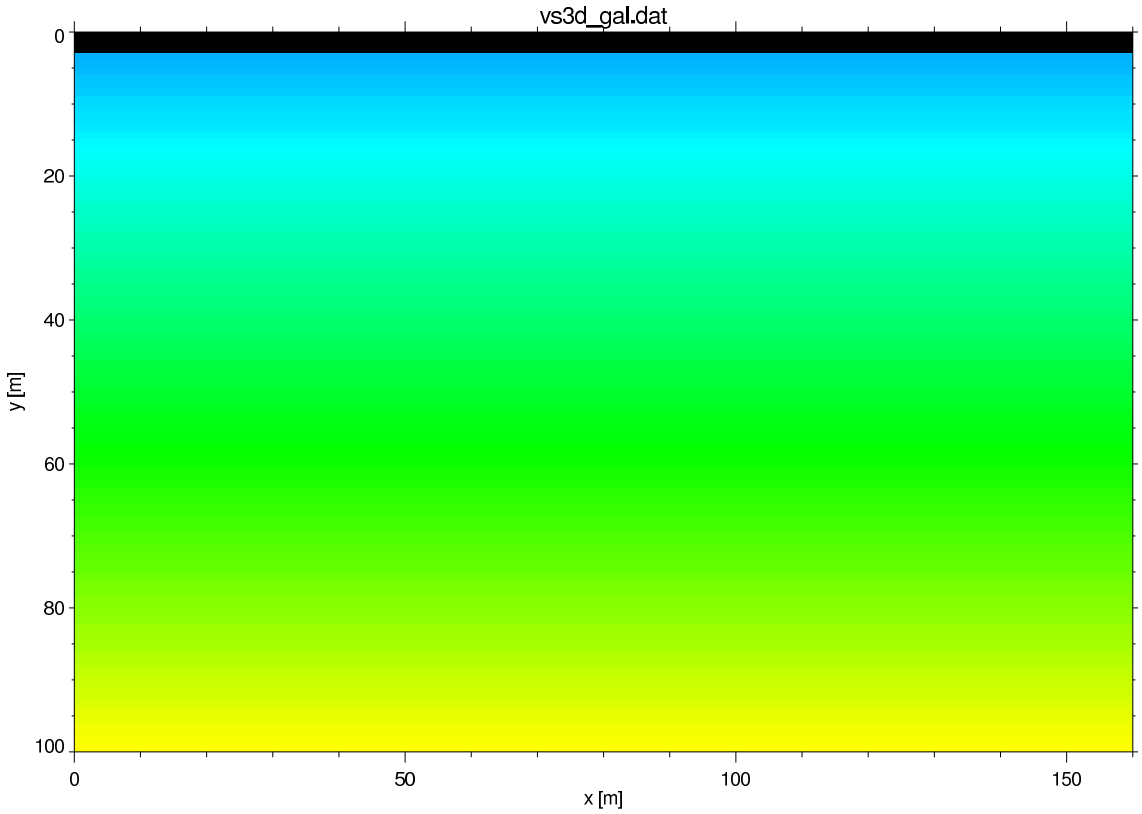

Figure 4.6: *S-velocity model for the Piora gallery data set. The velocity in the 3D model varies between* 2000 m/s *(blue) and* 4849, 67 m/s *(yellow) (*$z = 0$, $v_{max} = 4000\ m/s$*).*

4.2 Fresnel Volume Migration

The same procedure as in the corresponding previous chapters was performed with the seismic data set. The results (see Figure 4.7) show strong reflections appearing in $40\,m$ depth at $x = 0\,m$ and about $80\,m$ depth at $x = 80\,m$.

By taking a closer look on a $26,57°$ (Fig. 4.8) and $-26,57°$ (Fig. 4.9) inclined plane to the horizontal one can observe that the reflector is not distributed symmetrically to the x-y plane but the distance to the tunnel axis increases as z increases.

Figure 4.10 illustrates the fault zone in vicinity to the tunnel. The Piora Basin is the main feature located according to the geological mapping in a depth of $y = 78\,m$.

The following image (Figures 4.11) shows strong reflections near the location of the Piora Basin indicated by a red line.

Figure 4.12 shows the absolute value stack of 17 common receiver gathers. The outline of the Piora Basin is represented by a black line.

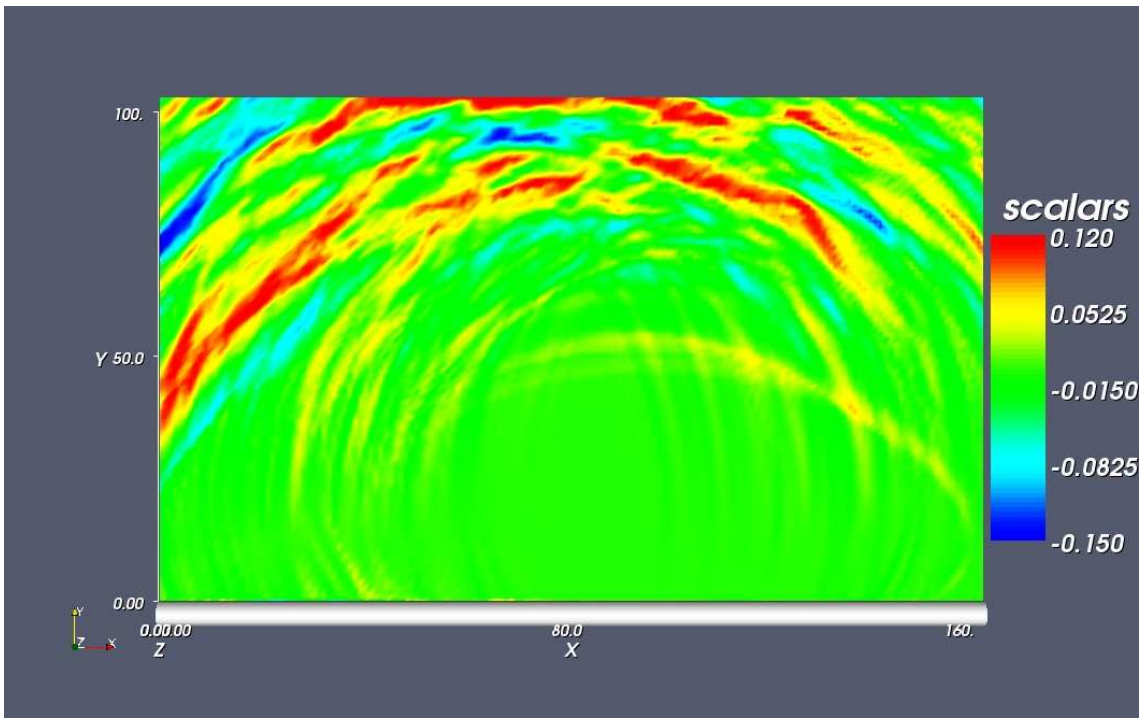

Figure 4.7: *FVM: true-phase-stack. Scalars denote the amplitudes.*

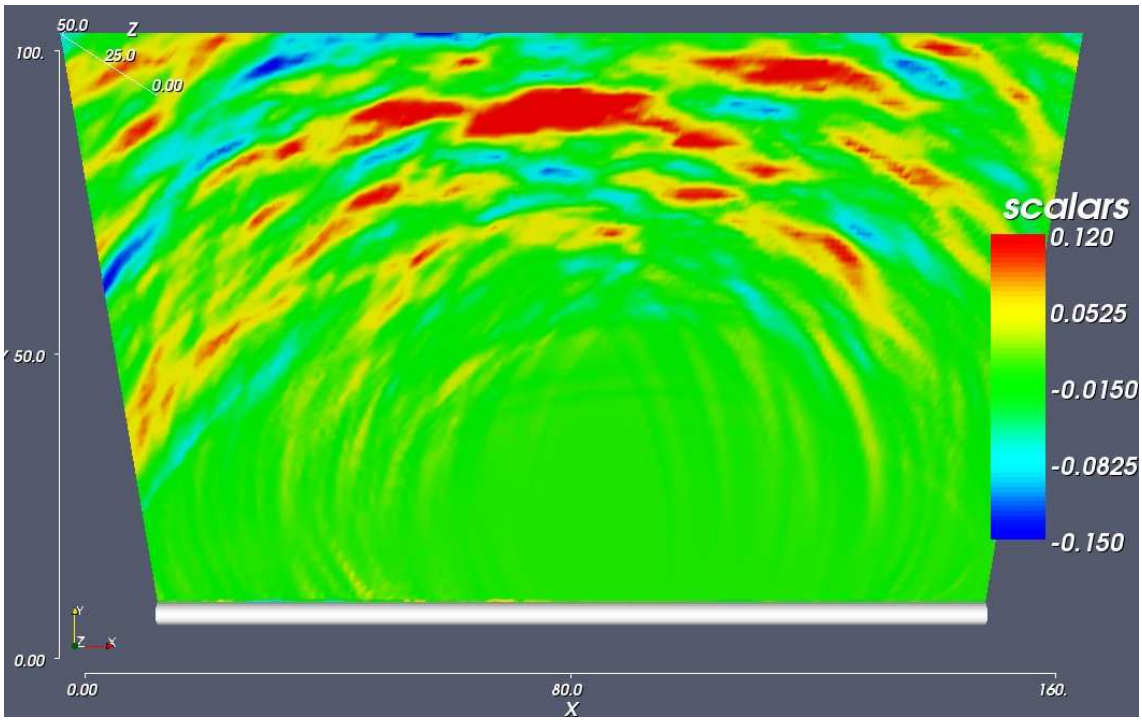

Figure 4.8: *FVM: true-phase-stack.* $26,57°$ *inclined plane to the horizontal. Scalars denote the amplitudes.*

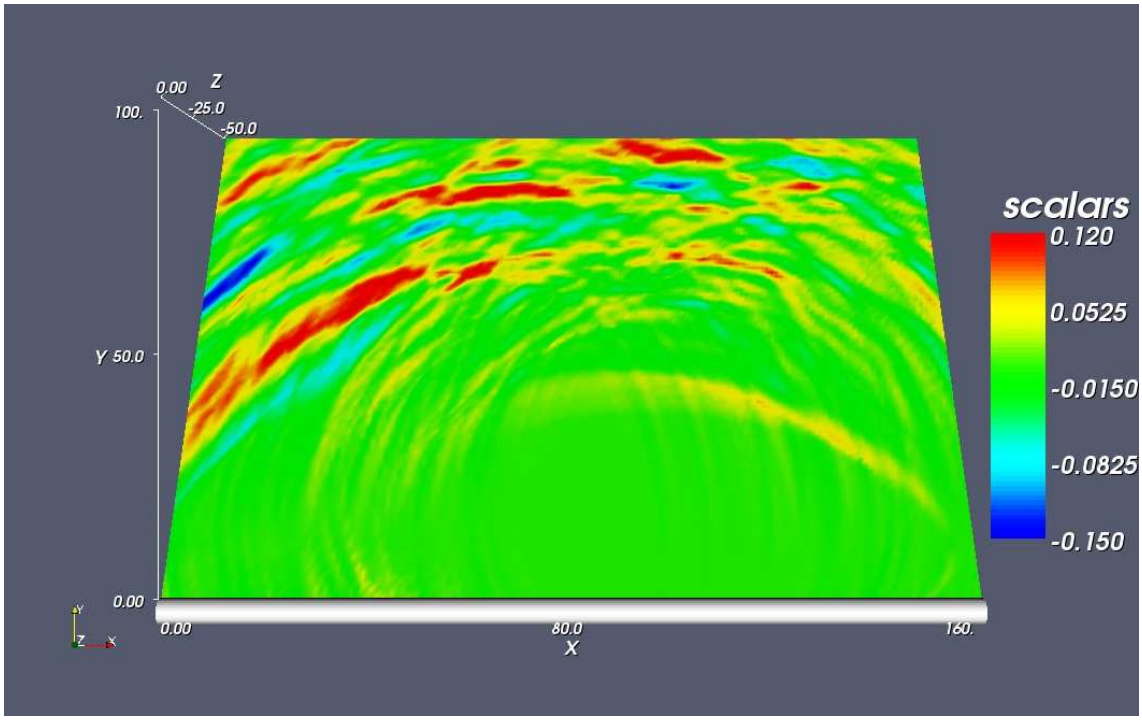

Figure 4.9: *FVM: true-phase-stack.* $-26,57°$ *inclined plane to the horizontal. Scalars denote the amplitudes.*

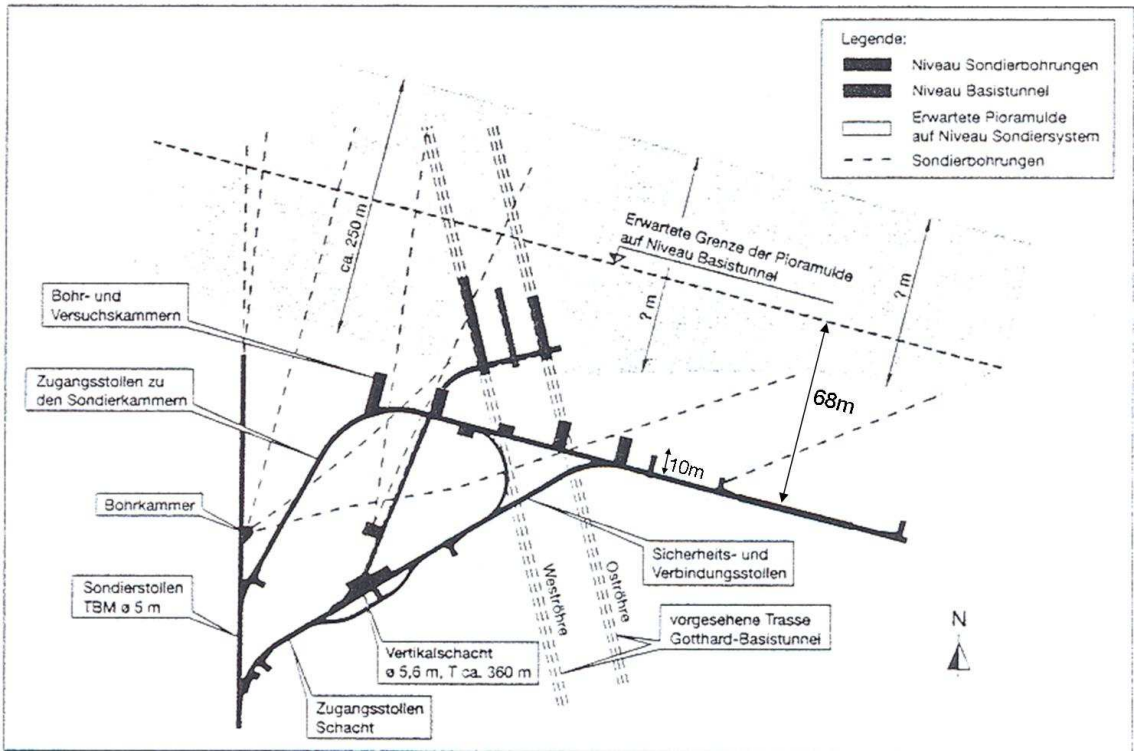

Figure 4.10: *The Piora Basin (Pioramulde, dashed line) proceeds in a depth of* $y = 78$ *m parallel to the x-axis.*

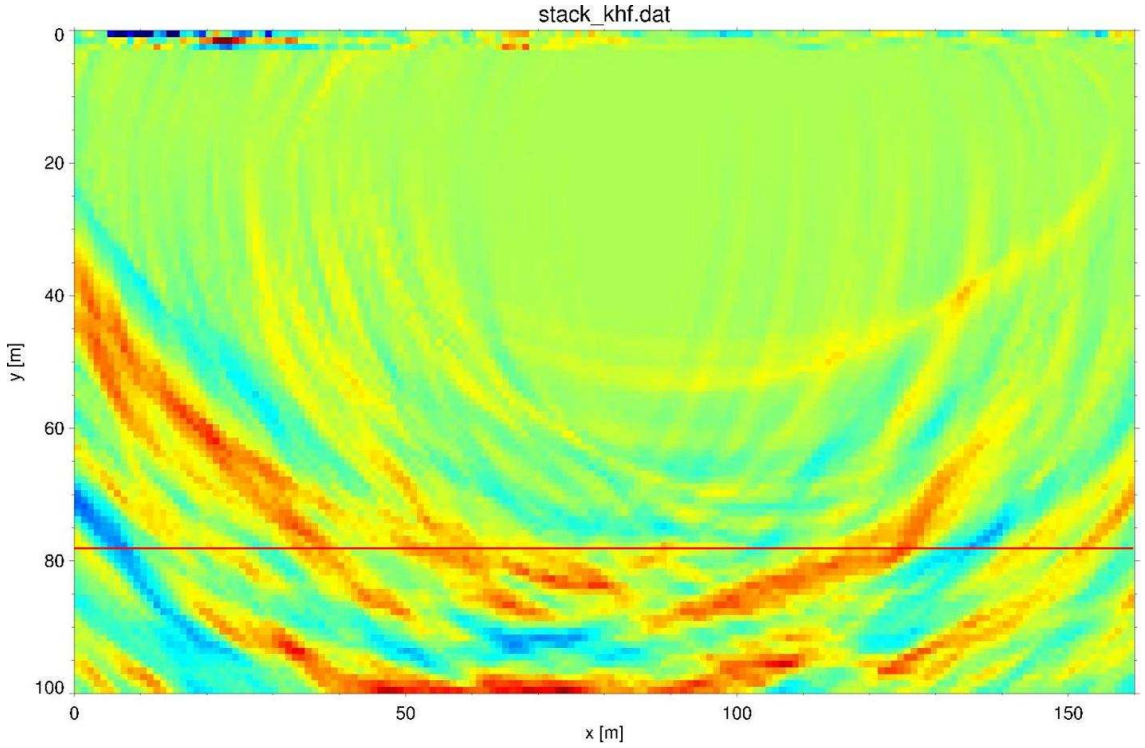

Figure 4.11: *FVM, true-phase-stack: Seismic profile and progress of the Piora Basin in a depth of y = 78 m parallel to the x-axis. The fault zone is indicated by a red line.*

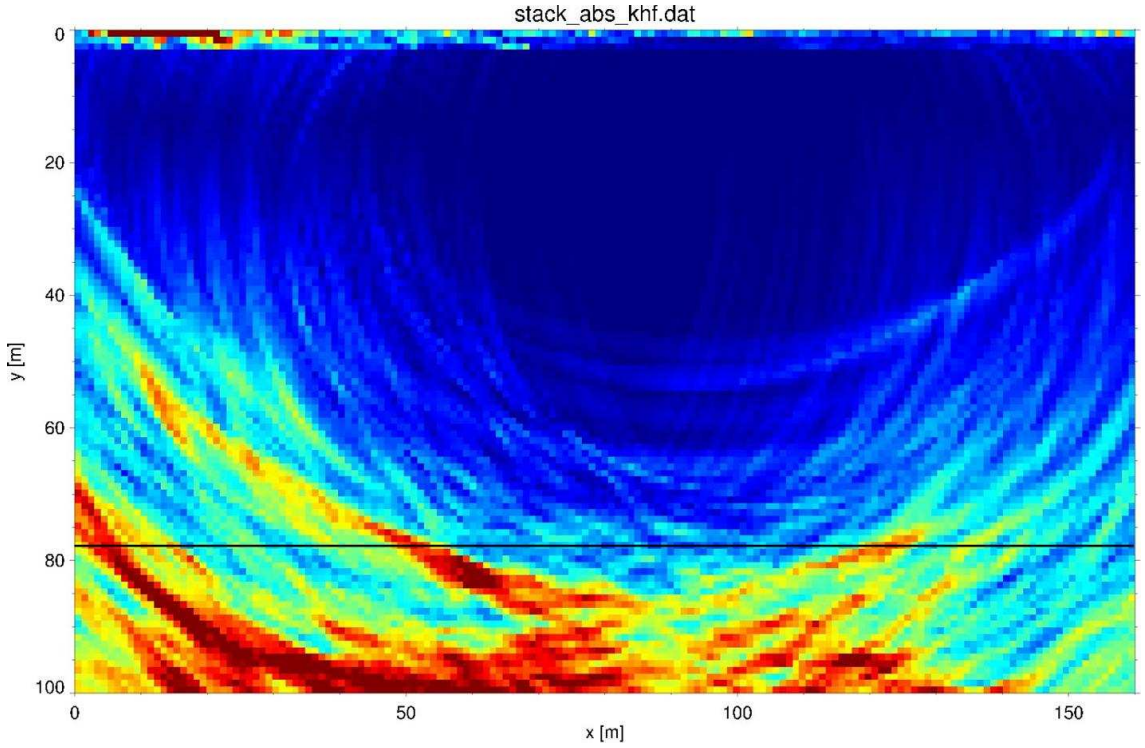

Figure 4.12: *FVM, absolute-value-stack: The progress of the Piora Basin is indicated by a black line.*

4.3 Combination of RIS and FVM

The entire frequency range was separated into 4 frequency bands with a width of 200 Hz each. FVM was applied to the 100 Hz and 300 Hz mean frequency band after the determination of the polarization by the covariance matrix method. The images show strong reflections occurring in a depth of approximately $75\,m$ between $x = 40\,m$ and $x = 100\,m$ (see Figure 4.13).

The spatial orientation of the reflector shall be illustrated. Considering all reflections with amplitudes greater than a given absolute value of the amplitude the following images are obtained (see Figures 4.14 and 4.15).

Figure 4.16 correlates the migration result obtained by RIS in combination with FVM with the geology in particular with the Piora Basin.

The absolute-value-stack of all common receiver gathers is displayed in Figure 4.17. Major reflections occur behind a black line indicating the trend of the Piora Basin.

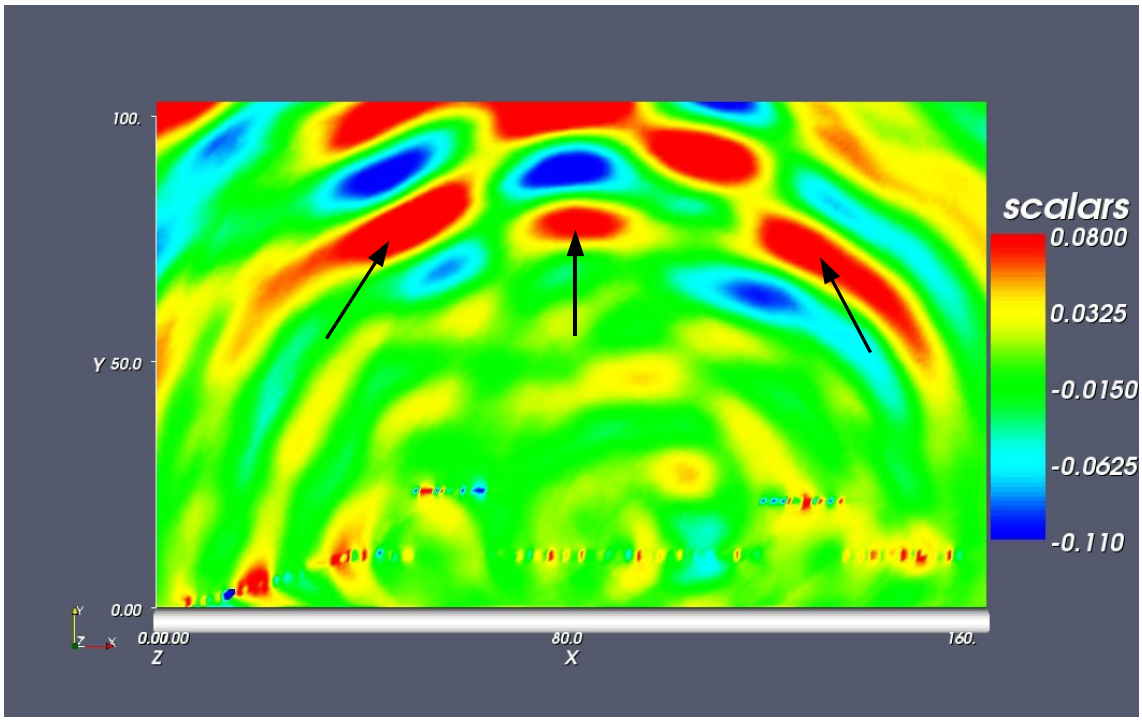

Figure 4.13: *RIS + FVM, true-phase-stack. Strong reflections occurring in a depth of 75 m indicated by black arrows. Scalars denote the amplitudes.*

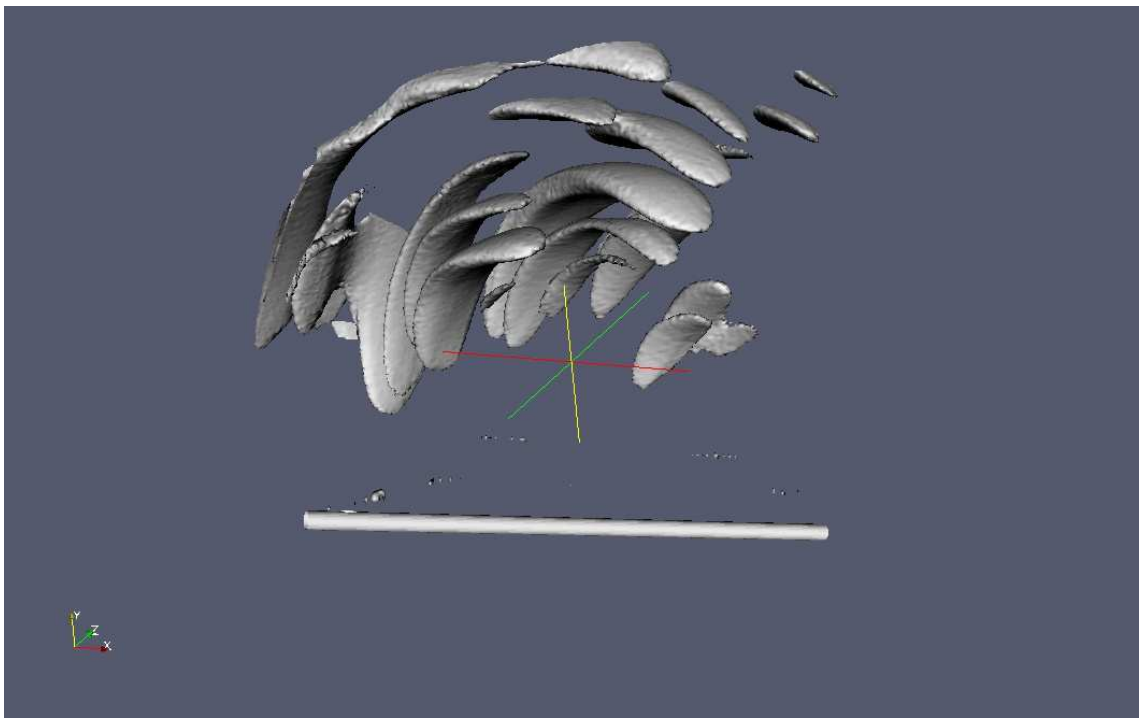

Figure 4.14: *RIS + FVM, true-phase-stack. Shape of all reflectors with high amplitudes.*

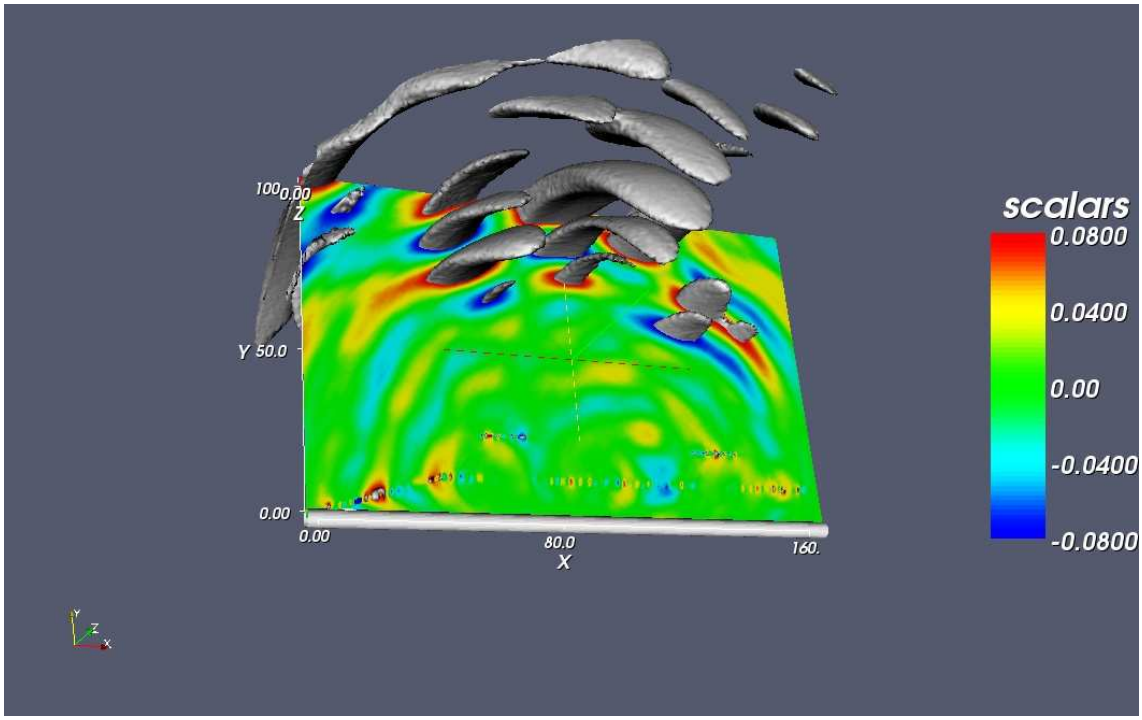

Figure 4.15: *RIS + FVM, true-phase-stack. Shape of all reflectors with high amplitudes in front of the x-y plane. Scalars denote the amplitudes.*

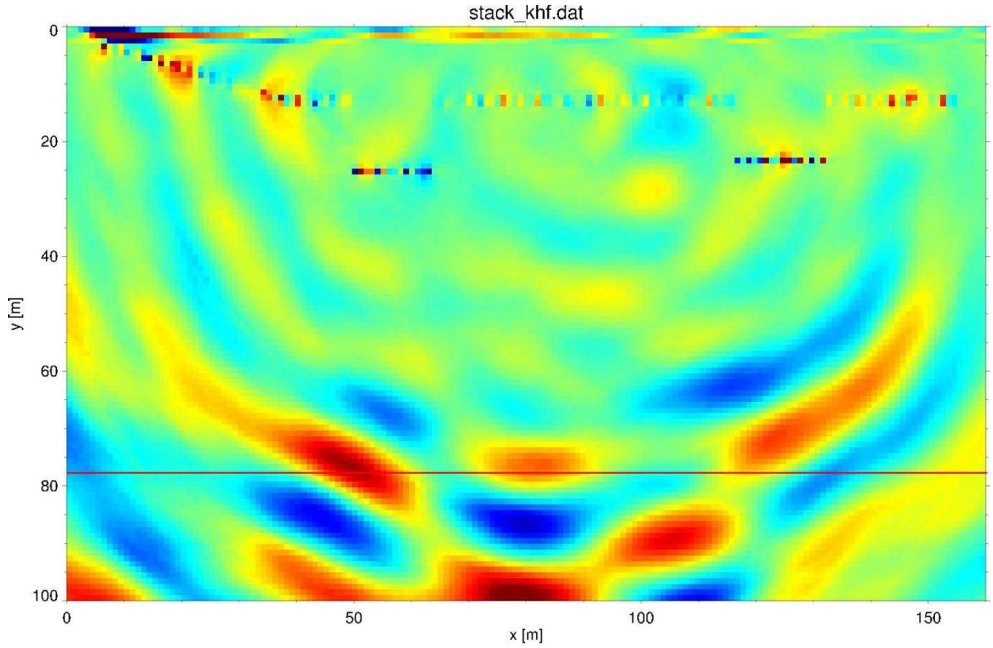

Figure 4.16: *RIS + FVM, true-phase-stack: Seismic profile and progress of the Piora Basin in a depth of y = 78 m parallel to the x-axis. The fault zone is indicated by a red line.*

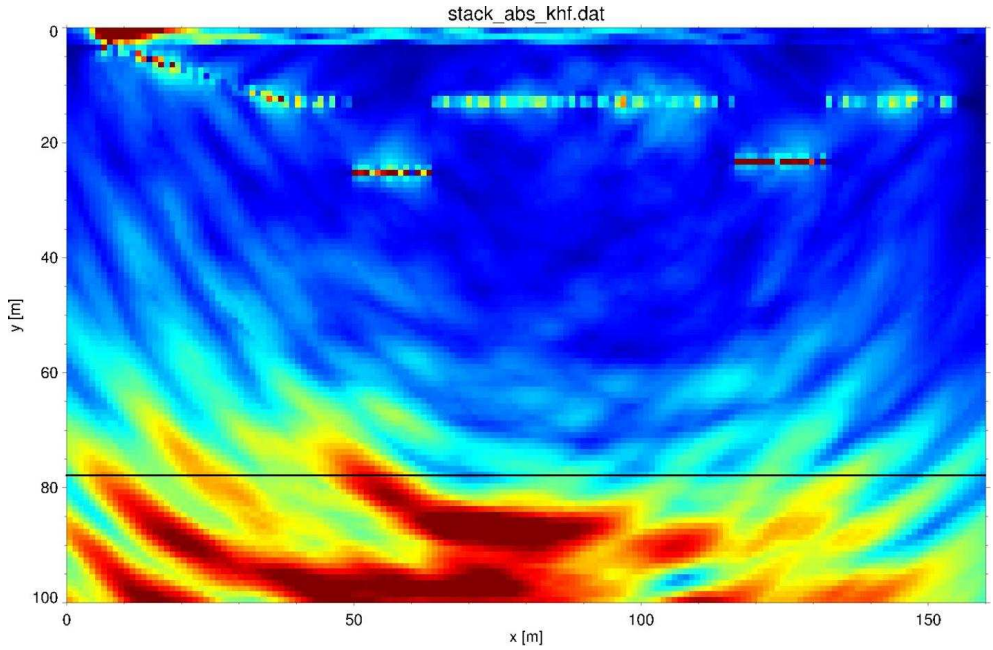

Figure 4.17: *RIS + FVM, absolute-value-stack: Seismic profile and progress of the Piora Basin in a depth of y = 78 m parallel to the x-axis. The fault zone is indicated by a black line.*

4.4 Summary and conclusions

The position of the Piora Basin is mirrored in the images achieved by FVM and the combination of RIS and FVM. The strong reflections occurring in a depth between 70 and 100 meters could be correlated partly with the geology. The images obtained by applying the shear wave velocity model and performing KPSDM on the whole frequency range and on the low frequency band showed many artifacts and were not capable for the interpretation.

Chapter 5

General summary and conclusions

The application of FVM to the two data sets showed significant results, reduced spatial ambiguity and improved the resolution in the images. Geologically relevant structures were focused and imaged more clearly compared to the images obtained by standard migration techniques as KPSDM. The integration of FVM and RIS yields a more pronounced image of the tunnel environment.

For the Piora data set the gneiss transition could be imaged very precisely using P- and S-waves. Unfortunately the high frequency images obtained by RIS for this data set showed no improvements because the gneiss is a very diffuse scatterer at these frequencies. The separation of P- and S-waves enabled us to detect a geological feature not observed in the images before the separation of the wave fields.

In the images derived from the Piora gallery data set we were able to correlate the most prominent reflectors with the Piora Basin. Once again the results obtained by the andvanced imaging technique FVM showed less artifacts, increased resolution and reduced spatial ambiguity.

It is possible to use the developed algorithms and programs for any kind of bore hole or excavation in particular for vertical bore holes. FVM is especially suited for low data coverage which is often the case in bore holes. The 3D RIS is also very important for surface measurements of layered media.

Acknowledgements

This work was performed within the OnSITE project, which is part of the R&D-Program GEOTECHNOLOGIEN funded by the German Ministry of Education and Research (BMBF) (grant 03G0637C).

I would like to thank my colleagues Stefan Buske and Kolja Groß as well as my supervising professor Dr. Serge Shapiro for their support and motivation. I am grateful for the assistance of our collaborators at the GFZ Potsdam Rudi Giese, Stefan Lüth and Aissa Rechlin. Thank you Stine Gutjahr and Nicolas Hummel for proofreading my dissertation.

Let me thank my family who made my dissertation possible and encouraged me during the whole three years.

Finally I would like to thank my friends Gudrun Zimmermann, Jörg Wichmann and Ronald Stitz for their encouragement and for giving me joy during my free time.

References

Aki, K. and Richards, P.G. (1980). Quantitative Seismology: Theory and methods, Vols. I and II, 156-157, 169-170. San Francisco: W.H. Freeman.

Bohlen, T., Giese, R., Jetschny, S., Lorang, U., Rabbel, W., Müller, C. and Lüth, S. (2007). Rayleigh-to-shear wave conversion at the tunnel face - From 3D-FD modeling to ahead-of-drill exploration. Geophysics, Vol. 72, No. 6, p. T67-T79

Buske, S., Gutjahr, S. and Sick, C. (2009). Fresnel volume migration of single-component seismic data Geophysics, 74, WCA47-WCA55

Červený, V. and Soares, J.E.P (1992). Fresnel volume ray tracing. Geophysics, 57, 902-915

Červený, V. (2001). Seismic ray theory. Cambridge University Press.

Chapman, C.H. (2004). Fundamentals of Seismic Wave Propagation. Cambridge University Press.

Giese, R., Klose, C. and Borm, G. (2005). In-Situ seismic investigations of fault zones in the Leventina Gneiss Complex of the Swiss Central Alps. Geological Society Special Publications 240, 15-24

Goertz, A., Müller, C., Buske, S. and Lüth, S. (2003). Fresnel-volume multicomponent migration. EAGE 65th Conference & Exhibition Abstracts, Stavanger, Norway

Hardage, B.A. (1985). Vertical Seismic Profiling: A: Principles, 2nd Edition London: Geophysical Press.

Jackson, G.M., Mason, I.M. and Lee, D. (1991). Multicomponent common-receiver gather migration of single-level walk-away seismic profiles. Geophysical Prospecting, 39, 1015-1029

Jepsen, D.C. and Kennett, B. L. N. (1990). Three-component analysis of regional seismograms. Bulletin of the Seismological Society of America, Vol. 80, No. 6, 2032-2052

Kneib, G., Kassel, A. and Lorenz, K. (2000). Automated seismic prediction ahead of the tunnel boring machine. First Break, 18, 295-302

Kravtsov, Y.A. and Orlov, Y.I. (1990). Geometrical optics of inhomogeneous media. Springer Verlag, Berlin, Heidelberg, New York

Kvasnicka, M. and Červený, V. (1994). Fresnel volumes and Fresnel zones in complex laterally varying structures. Journal of Seismic Exploration, 3, 215-230

Lüth, S., Buske, S. and Shapiro, S.A. (2004). Research and Development Project: Tunnel-Imaging. Report 2003/2004. GeoForschungsZentrum Potsdam.

Lüth, S., Buske, S., Giese, R. and Goertz, A. (2005). Fresnel volume migration of multicomponent data. Geophysics, Vol. 70, No. 6

Müller, G. (1989). Migration Seismischer Wellenfelder. Universität Frankfurt.

Newman, P. (1973). Divergence effects in a layered earth. Geophysics, 38: 481-488

Newman, P. (1975). Amplitude and phase properties of a digital migration process: Presented at the 37th Ann. Internat. Mtg., Europe. Assoc. Expl. Geoph., (Republished in: First Break, 8, 397-403, 1990)

Otto, R., Button, E.A., Bretterebner, H. and Schwab, P. (2002). The application of TRT - true reflection tomography - at the Unterwald Tunnel. Felsbau, 20, 51-56

Podvin, P. and Lecomte, I. (1991). Finite difference computation of traveltimes in very contrasted velocity models: A massively approach and its associated tools. Geophysical Journal International, 105, 271-284

Press, W.H., Flannery, B.P., Teukolsky, S.A. and Vetterling, W.T. (1992). Runge Kutta Method and Adaptive Step Size Control for Runge-Kutta. §16.1 and 16.2 in Numerical Recipes in Fortran: The Art of Scientific Computing. Cambridge University Press, 2nd Edition.

Rentsch, S. (2007). A migration-type approach for the fast location of seismicity: Theory and applications. PhD thesis, FU Berlin,
http://www.diss.fu-berlin.de/2007/474/indexe.html

Schleicher, J., Tygel, M. and Hubral, P. (1993). 3-D true-amplitude finite-offset migration. Geophysics, 58, 1112-1126

Schneider, T. R. (1997). Gotthard-Basistunnel: Neue geologische Erkenntnisse im Bereich des Tavetscher Zwischenmassivs und der Piora-Mulde. Schweizerischer Ingenieur- und Architekten-Verein, Dokumentation D0143, 15-26.

Sheriff, R.E. and Geldart, L.P. (1995). Exploration Seismology. Cambridge University Press, 2nd Edition.

Sick, C.M.A. (2005). Structural Investigations of Chile: Kirchhoff Prestack Depth Migration versus Fresnel Volume Migration. Dissertation, FU Berlin.

Spencer, T.W. (1985). Measurement and interpretation of seismic attenuation. Developments in Geophysical Exploration Methods. A. A. Fitch, Vol. 6, 73-110. Amsterdam: Elsevier.

Sun, H. and Schuster, G. T. (2001). 2D wave path migration. Geophysics, 65, 584-595

Takahashi, T. (1995). Prestack migration using arrival angle information. Geophysics, 60, 154-163

Tillmans, M. and Gebrande, H. (1999). Focusing in prestack isochrone migration using instantaneous slowness information. Pure and Applied Geophysics, 156, 187-206

Toksoz, M.N. and Johnston, D.H. (1981). Seismic Wave Attenuation, Geophysical Reprint Series 2. Tulsa: Society of Exploration Geophysicists.

Tzavaras, J., Buske, S., Groß, K. and Shapiro, S.A. (2008). Seismic imaging around and ahead of tunnel construction sites. Geophysical Research Abstracts, 10

Tzavaras, J., Buske, S., Groß, K. and Shapiro, S.A. (2008). Tunnel seismic investigations 3D imaging. EAGE 70th annual meeting and technical exhibition: expanded abstracts

Tzavaras, J., Buske, S., Groß, K. and Shapiro, S.A. (2008). Tunnel seismic investigations 3D imaging. 14th European Meeting of Environmental and Engineering Geophysics: expanded abstracts

Tzavaras, J., Buske, S., Groß, K. and Shapiro, S.A. (2008). Tunnel seismic investigations 3D imaging Tagungsband der 68. Jahrestagung der Deutschen Geophysikalischen Gesellschaft

White, J.E. (1965). Seismic Waves - Radiation, Transmission and Attenuation. New York: McGraw-Hill.

White, J.E. (1966). Static friction as a source of seismic attenuation. Geophysics, 31: 333-339

Yoon, M. (2005). Deep seismic imaging in the presence of a heterogeneous overburden: Numerical modeling and case studies from the central Andes and southern Andes. PhD thesis, FU Berlin, http://www.diss.fu-berlin.de/2005/74/indexe.html

Yoon, M., Buske, S., Shapiro, S.A. and Wigger, P. (2009). Reflection Image Spectroscopy across the Andean Subduction Zone. Tectonophysics, 472, 51-61